AFOSR-TR-95 ___

REPORT DOCUMENTATION PAGE

G633

1. AGENCY USE ONLY (Leave blank)	2. REPORT DATE 1 Feb. 1995	3. REPORT TYPE AND DATES COVERED Final, 1 Feb. 1992–31 Jan. 1995	
4. TITLE AND SUBTITLE The Effect of a Flexible Fiber Cover on Controlling Boundary Layer Flow and Heat Transfer			**5. FUNDING NUMBERS** 92- Contract F49620-J-0121 2307/BS
6. AUTHOR(S) Adrian Bejan			
7. PERFORMING ORGANIZATION NAME(S) AND ADDRESS(ES) Duke University Department of Mechanical Engineering and Materials Science Durham, NC 27708-0300			**8. PERFORMING ORGANIZATION REPORT NUMBER** None
9. SPONSORING/MONITORING AGENCY NAME(S) AND ADDRESS(ES) Air Force Office of Scientific Research Directorate of Aerospace and materials Sciences Bolling Air Force Base, DC 20332-0001 *NA*			**10. SPONSORING/MONITORING AGENCY REPORT NUMBER** F49620-92-J0121
11. SUPPLEMENTARY NOTES			

DTIC
S ELECTE D
OCT 1 3 1995
G

12a. DISTRIBUTION/AVAILABILITY STATEMENT Approved for public release, distribution unlimited	**12b. DISTRIBUTION CODE**

13. ABSTRACT (Maximum 200 words)

This report describes the friction and heat transfer characteristics of a solid surface covered with flexible fibers. The work consisted of analysis, numerical simulations, and laboratory experiments. Chapter 1 documents the pressure drop and heat transfer through bundles of parallel cylinders in a domain that has been overlooked, namely, low Reynolds numbers, arrays that are long in the direction of flow such that the flow is hydraulically and thermally fully developed, and cylinders inclined relative to the flow direction. The heat transfer, friction and mechanical (elastic) interaction between an external laminar flow and a solid surface covered by a layer of fibers is documented in Chapter 2. The flow is initially perpendicular to the surface, and the fibers can bend. The effect of fiber bending, is described by a new dimensionless group, the stiffness number S. Chapters 3 and 4 report results for the optimal spacing between cylinders in arrays with natural or forced convection. Chapter 5 shows how to correlate the optimal sizes of bodies with specified external forced convection heat transfer, when the objective is to minimize the total rate of entropy generation, or the total cost.

DTIC QUALITY INSPECTED 5

14. SUBJECT TERMS Forced convection, surfaces covered with fibers, inclined fibers, flexible fibers, optimal spacing between cylinders	**15. NUMBER OF PAGES** 109
	16. PRICE CODE

17. SECURITY CLASSIFICATION OF REPORT Unclassified	**18. SECURITY CLASSIFICATION OF THIS PAGE** Unclassified	**19. SECURITY CLASSIFICATION OF ABSTRACT** Unclassified	**20. LIMITATION OF ABSTRACT**

19951011 021

Final Technical Report

THE EFFECT OF A FLEXIBLE FIBER COVER ON CONTROLLING BOUNDARY LAYER FLOW AND HEAT TRANSFER

Accesion For		
NTIS CRA&I		☑
DTIC TAB		☐
Unannounced		☐
Justification		
By		
Distribution /		
Availability Codes		
Dist	Avail and / or Special	
A-1		

AFOSR Contract no. F49620-92-J-0121

Principal Investigator

Adrian Bejan

J. A. Jones Professor of Mechanical Engineering

Box 90300

Duke University, Durham, NC 27708-0300

February 1, 1995

Contents

ii

Abstract

This research project focused on the friction and heat transfer characteristics of a solid surface covered with flexible fibers. The work consisted of analysis, numerical simulaitons, and laboratory experiments. Related developments that grew out of this work were investigated in the later part of the project: specifically, the optimal spacings between cylinders (e.g. fibers) with heat transfer, and the optimal sizes of bodies immersed in an external flow.

Chapter 1 documents the pressure drop and heat transfer through bundles of parallel cylinders in a domain that has been overlooked, namely, low Reynolds numbers, arrays that are long in the direction of flow such that the flow is hydraulically and thermally fully developed, and cylinders inclined relative to the flow direction. The numerical results cover the range $1 \leq Re_D \leq 30, 0.72 \leq Pr \leq 100, 0.6 \leq \phi \leq 0.95$ and $0° \leq \beta \leq 60°$, where ϕ is the porosity of the bundle as a saturated porous medium, and β is the angle between the cylinder centerline and the direction perpendicular to the flow direction. The accuracy is verified by means of experimental measurements of the pressure drop across a bundle with 115 cylinders in the flow direction, in the range $8 < Re_D < 50, 0.84 \leq \phi \leq 0.92$ and $0° \leq \beta \leq 60°$. The results show that significant errors may occur if the available large-Re_D information is extrapolated to the domain covered by this study.

The heat transfer, friction and mechanical (elastic) interaction between an external laminar flow and a solid surface covered by a layer of fibers is documented numerically in Chapter 2. The flow is initially perpendicular to the surface, and the fibers can bend. In the first part of the chapter, it is assumed that the fibers are inflexible. It is shown that the effect of the fiber layer on the overall heat transfer can be correlated in terms of the fraction of the external flow that penetrates into the fiber layer. The second part focuses on the effect of fiber bending, which is described by a new dimensionless group: the stiffness number $S = EI / (\rho U_\infty^2 L^4)$. It is shown that the wall heat transfer, friction and fiber layer flow fraction exhibit a sudden decrease when S drops below a critical value, S_c. The critical stiffness number can be correlated as $S_c = C(H/L)^5 (D/H)^2 / (1 - \phi)$ where C is a constant of order 0.4, H and D are the fiber length and diameter, L is the half-length of the solid wall, and ϕ is the porosity of the fiber layer.

Chapter 3 summarizes a theoretical, numerical and experimental study of how to select the spacing (S) between horizontal cylinders in an array with laminar natural convection, such that the total heat transfer (q) between the array and the ambient is maximized. The volume occupied by the array (height H, width W, cylinder length L) and the cylinder diameter (D) are arbitrary but fixed, while the spacing (or number of cylinders in the array) varies. The optimal spacing and maximum heat transfer results predicted theoretically are developed into accurate and well tested correlations by means of numerical simulations and experimental measurements.

The recommended correlations are $S_{opt}/D = 2.72(H/D)^{1/3} Ra_D^{-1/4} + 0.263$ and $\tilde{q}_{max} = 0.448\left[(H/D)^{1/3} Ra_D^{-1/4}\right]^{-1/6}$ where $\tilde{q}_{max}$ is the dimensionless maximum overall thermal conductance, $\tilde{q}_{max} = q_{max} D^2/[H\,LW\,k(T_w - T_\infty)]$. The optimal spacing is relatively insensitive to whether the cylinders are isothermal or with uniform heat flux. The corresponding problem of finding the optimal spacing when the heat transfer is by forced convection is considered in Chapter 4.

Chapter 5 shows how to correlate the optimal sizes of bodies with specified external forced convection heat transfer, when the objective is to minimize (1) the total rate of entropy generation, or (2) the total cost. Specific results are reported for the cylinder in cross-flow, the sphere, and the flat plate in parallel flow. The results are presented in terms of dimensionless parameters that show that regardless of the body shape, the optimal size increases monotonically with the heat transfer duty parameter. A universal correlation is obtained by nondimensionalizing the body size as a Reynolds number based on the transversal length scale of the flow, and by replacing the body with an equivalent one in two-dimensional flow. The optimal sizes correlated in this manner can be applied to bodies of other shapes.

Chapter 1

FORCED CONVECTION IN BANKS OF INCLINED CYLINDERS AT LOW REYNOLDS NUMBERS

1.1 Introduction

This chapter documents the flow and heat transfer characteristics of bundles of parallel cylinders that are inclined relative to the free stream that bathes them. The emphasis is on (a) the low Reynolds number range $Re_D \leq 30$, (b) the fully developed regime, and (c) the effect of the angle of inclination on the pressure drop and heat transfer coefficient. These aspects have been overlooked in spite of the large research effort that has been devoted to banks of cylinders in cross-flow. The progress on this general topic has been reviewed by Zukauskas (1972, 1987a, b) and Kays and London (1984).

In his more recent review, Zukauskas (1987b) proposed a correction factor to account for the effect of angle of inclination on pressure drop calculations. It is unclear whether his method is universally valid, or applies only to a certain range of Reynolds numbers and a certain type of cylinder array. One objective of the present study was to clarify the conditions under which Zukauskas's correction is applicable.

The flow and heat transfer results assembled in this chapter were developed in three phases. First, numerous cases of the flow and temperature fields in long bundles of inclined cylinders were simulated numerically, based on detailed three-dimensional calculations. In the second phase, the heat and fluid flow results were correlated into a saturated porous medium model that accounts for the angle of inclination and the low Reynolds number range. The third phase was experimental, where the accuracy of the numerical results was tested against laboratory measurements of the pressure drops through bundles at several cylinder inclinations and Reynolds numbers.

1.2 Mathematical Formulation

The numerical part of the study refers to an array of staggered cylinders, with their centers arranged in an array of equilateral triangles. Two orientations of the flow relative to the array were examined (Fig. 1.1, top). The entire array was tilted to an angle β that varied from $0°$ to $60°$ relative to the perpendicular (Fig. 1.1, bottom). In the numerical simulations (and unlike in the experiments, section 1.6) the spacing between cylinders was fixed so that the porosity of the bundle ϕ was not a function of the angle β. In an equilateral triangle array the porosity is $\phi = 1 - 0.907 (D/S)^2$, where S is the distance between cylinder centers.
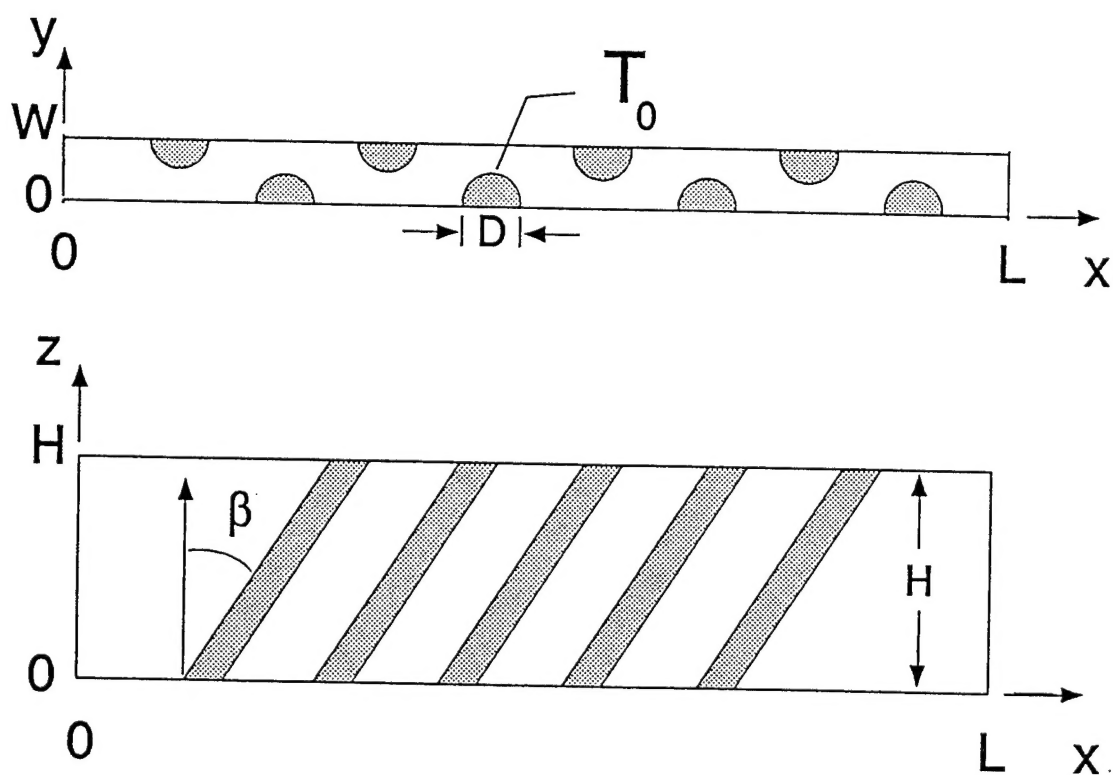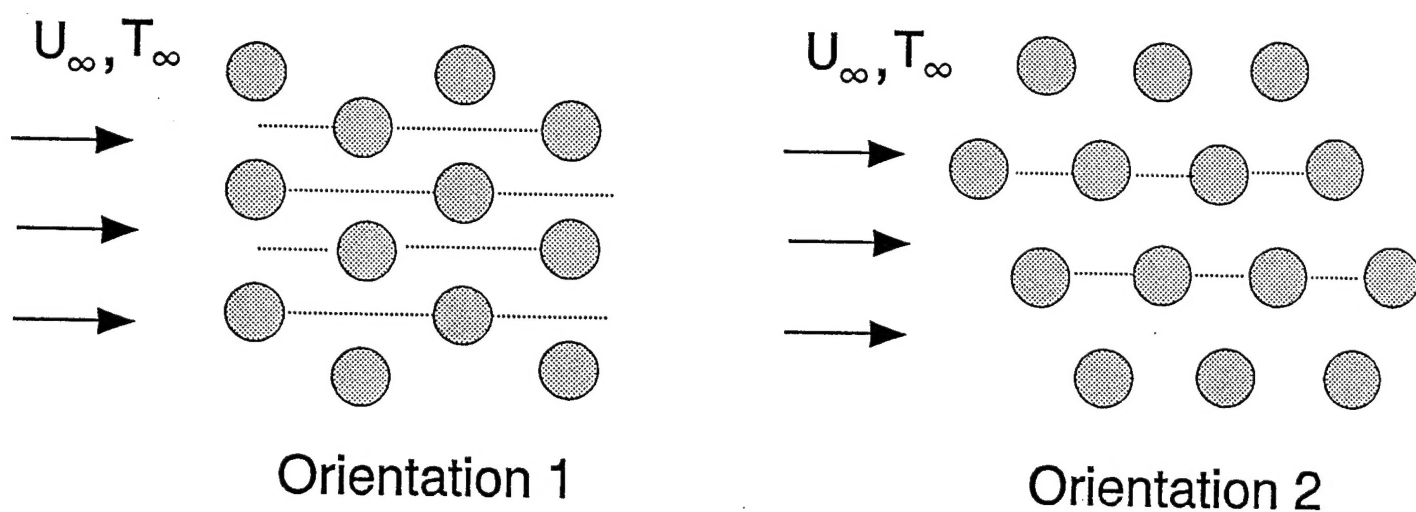
1

Figure 1.1 Arrays of parallel cylinders with forced convection heat transfer (top), and three-dimensional computational domain (bottom).

In the range $Re_D \leq 30$ the flow is laminar and the wake behind each cylinder is steady and symmetric. This allowed us to view the array as a sandwich of many channels like the one highlighted in the middle of Fig. 1.1, and illustrated by the dashed lines in the top drawings of Fig. 1.1. There was no mixing between the channels. The computational domain contained only one channel.

The equations that account for the conservation of mass, momentum and energy in the fluid regions of the three-dimensional frame defined in Fig. 1.1 are

$$\frac{\partial u}{\partial x} + \frac{\partial v}{\partial y} + \frac{\partial w}{\partial z} = 0 \tag{1.1}$$

$$u_j \frac{\partial u_i}{\partial x_j} = -\frac{1}{\rho} \frac{\partial P}{\partial x_i} + \nu \frac{\partial^2 u_i}{\partial x_j^2} \tag{1.2}$$

$$u \frac{\partial T}{\partial x} + v \frac{\partial T}{\partial y} + w \frac{\partial T}{\partial z} = \alpha \left(\frac{\partial^2 T}{\partial x^2} + \frac{\partial^2 T}{\partial y^2} + \frac{\partial^2 T}{\partial z^2} \right) \tag{1.3}$$

where (u,v,w) are the velocity components aligned with the (x,y,z) axes. Equation (1.2) makes use of the tensor notation convention that triple summation is indicated by repeated indices. The boundary conditions on the cylinder surfaces account for no slip, no penetration and uniform temperature,

$$u_i = 0 \quad \text{and} \quad T = T_0 \quad \text{on all cylinder surfaces} \tag{1.4}$$

Along the top and bottom of the channel, and on the side-wall regions contained between cylinders the conditions were zero shear, no penetration and zero heat flux,

$$\frac{\partial u}{\partial z} = 0, \quad \frac{\partial v}{\partial z} = 0, \quad w = 0 \quad \text{and} \quad \frac{\partial T}{\partial z} = 0 \quad \text{at} \quad z = 0, H \tag{1.5}$$

$$\frac{\partial u}{\partial y} = 0, \quad v = 0, \quad \frac{\partial w}{\partial y} = 0, \quad \text{and} \quad \frac{\partial T}{\partial y} = 0 \quad \text{at} \quad y = 0, W \tag{1.6}$$

The flow was isothermal and longitudinally uniform at the channel inlet,

$$u = U_\infty, \quad v = 0, \quad w = 0 \quad \text{and} \quad T = T_\infty \quad \text{at} \quad x = 0 \tag{1.7}$$

The channel outlet conditions were zero stress and zero longitudinal heat flux,

$$-p + 2\mu \frac{\partial u}{\partial x} = 0, \quad \frac{\partial v}{\partial x} = 0, \quad \frac{\partial w}{\partial x} = 0, \quad \frac{\partial T}{\partial x} = 0 \quad \text{at} \quad x = L \tag{1.8}$$

The equations and boundary conditions were nondimensionalized by using D, U_∞ and $(T_0 - T_\infty)$ as representative scales,

$$(X,Y,Z) = \frac{(x,y,z)}{D}, \qquad (U,V,W) = \frac{(u,v,w)}{U_\infty} \tag{1.9}$$

$$\theta = \frac{T - T_\infty}{T_0 - T_\infty}, \qquad P = \frac{p}{\rho\, U_\infty^2} \qquad\qquad (1.10)$$

The nondimensional counterparts of equations (1.1)-(1.8), which are omitted for brevity, contain the nondimensional numbers

$$Re_D = \frac{U_\infty D}{\nu}, \quad Pr = \frac{\nu}{\alpha}, \quad \left(\tilde{H}, \tilde{L}, \tilde{W}\right) = \frac{(H, L, W)}{D} \qquad\qquad (1.11)$$

The system of nondimensional equations was solved using the finite element package FIDAP (1991). When the cylinders are inclined ($\beta \neq 0$) the problem is inherently three-dimensional and thus a 3-D solver was required. The computational domain was built up of 8 node brick elements. A Stokes flow solution was used to initialize the solution for the mass and momentum equations when $\beta = 0°$, and then the solution to each prior run was used to initialize the next run, as β was increased. Since the energy equation is only weakly coupled to the mass and momentum equations, it was solved separately for the various Pr values after the velocity field was determined.

Numerical testing indicated that a channel with 40 cylinders in the longitudinal direction allowed for pressure measurements at rows 11, 19 and 27 that were not effected by the entrance or exit regions. We verified that the flow was fully developed by calculating the pressures at three equidistant longitudinal locations (say a, b and c), and checking that the pressure drops matched, $P_a - P_b = P_b - P_c$. In all cases, the discrepancy between the two pressure drops was less than 1 percent.

The effect of doubling the channel height $\tilde{H}$ was found to be insignificant (less than 1 percent change in the pressure gradient) if the $\tilde{H} \geq 6$ and a free slip boundary condition was used at the top and bottom of the channel. The solution proved to be extremely sensitive to changes in channel height when a no slip condition was imposed on the top and bottom planes of the channel. Convergence testing for the mesh density was performed with $\beta = 45°$. The number of elements was doubled in each direction until such doubling produced a change in the pressure gradient of less than 3 percent. These tests were performed for each porosity, and for both orientations of the array.

All of the final numerical meshes for determining the pressure gradient required between 20,000 and 35,000 elements. Typically the initial run, which requires a Stokes flow solution for initialization, required 10 to 20 minutes of CPU time on a Cray Y-MP. The runs that followed generally required about 10 minutes of CPU time each. The temporary space required for the matrix solver ranged from 500 to several thousands of megabytes. This, in combination with the increased computational cost of doing proper convergence testing, made a supercomputer necessary. The convergence testing for stability in the calculated Nusselt number indicated that twice as many elements were necessary in the x direction to achieve a 3 percent stability in the

4

Nusselt number than were needed for the same stability in the pressure gradient. To solve for the velocity field on the finer mesh required about 50 minutes of CPU time on the Cray Y-MP. Three additional minutes were needed to solve the heat transfer problem for each Prandtl number.

The Nusselt number calculation could not be performed for the entire range defined by $0.6 \leq \phi \leq 0.95$, $0.72 \leq Pr \leq 100$ and $1 \leq Re_D \leq 30$. For example, in the case $\phi = 0.6$, $Pr = 0.72$, and $Re_D = 10$, the fluid reached thermal equilibrium with the solid almost immediately, i.e. after the first row. In the opposite extreme (e.g. $\phi = 0.95$, $Pr = 100$, $Re_D = 10$) the flow was not fully developed thermally at the downstream end of the computational domain, and no fully developed Nu could be reported. As a rule, if Nu varied by more than 5 percent over the 20 inner rows of cylinders, the thermal development was considered incomplete.

1.3.   Pressure Drop Results

The results that document the effect of the cylinder angle of inclination on pressure drop are presented in Figs. 1.2a-d. The ordinate shows the pressure gradient in an array with inclined cylinders, as a fraction of the pressure gradient when the same array is perpendicular to the same flow. The first three frames show that when $Re_D \leq 10$ the relative pressure drop $\Delta P(\beta)/\Delta P(0°)$ is influenced only by the angle β, and not by the other parameters (Re_D, ϕ, orientation). The β effect can be significant; for example, in all four frames of Fig. 1.2 the pressure drop decreases to 60 percent of its original value as β increases from 0° to 60°.

Figures 1.2a and 1.2d indicate that at Reynolds numbers larger than 10 the relative pressure drop depends on Re_D and ϕ, in addition to β. The pressure drop is considerably more sensitive to changes in the angle β at low porosities ($\phi = 0.6$) than at high porosities ($\phi = 0.9$). When the porosity is high the angle of inclination has no visible effect on the pressure drop if $\beta \leq 30°$.

These results can be compared with the single relative pressure drop curve reported by Zukauskas (1987), which falls right on top of the curve drawn in Fig. 2a for $Re_D = 30$ and $\phi = 0.6$. The present results suggest that the $\Delta P(\beta)/\Delta P(0°)$ curve is not universal, i.e. it is not independent of Re_D and ϕ. This lack of universality is particularly evident in the direction of increasing Re_D, which is the domain of heat exchanger applications. At the same time, the present results show that a universal relative pressure drop curve different than Zukauskas's exists when Re_D is smaller than 10.

We also correlated the pressure drop data for cross-flow ($\beta = 0°$) by modelling the array and the fluid as a saturated porous medium. In the small-Re_D limit the flow is expected to follow the Darcy model,
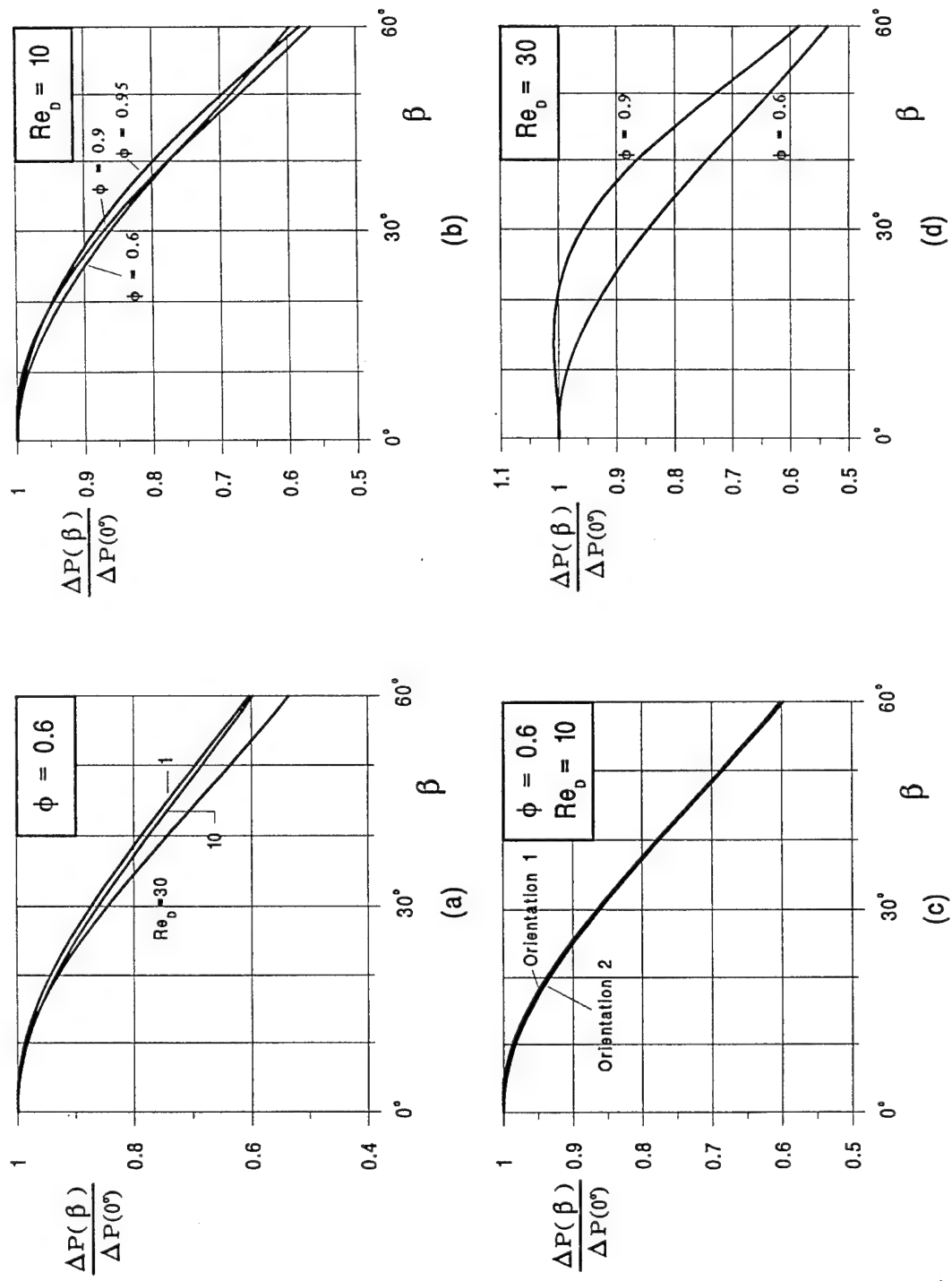
Figure 1.2   The effect of β, φ, Re_D and array orientation on the longitudinal pressure drop in fully developed flow.

6

$$-\frac{\partial p}{\partial x} = \frac{\mu}{K} u \tag{1.12}$$

The permeability K was determined by fitting the numerical pressure gradient results to equation (1.12), and correlating the K values using a formula similar to the Carman-Kozeny relation (Carman, 1937),

$$K = \frac{D^2}{125}\left[\frac{\phi^3}{(1-\phi)^2}\right]^r \tag{1.13}$$

with $r = 0.85$ for orientation 1, and $r = 0.8$ for orientation 2. Equation (1.13) agrees within 6 percent with the numerical K values deduced from equation (1.12) for orientation 1 and $\phi \le 0.9$. The agreement between equations (1.13) and (1.12) is within 35 percent for all the runs made for orientation 2: The average error for all the runs in both orientations was 10 percent. The agreement for the runs in orientation 2 is illustrated in Fig. 1.3, where the numbers listed after each point represent Re_D and ϕ. The use of $K^{1/2}$ as length scale in the dimensionless groups on the ordinate and abscissa of Fig. 1.3 is standard in the field of convection in porous media (Cheng, 1978; Nield and Bejan, 1992). Equation (1.12) is not shown in the figure: it would be represented by a line of slope -1 passing through the point (1,1), i.e. a line that would pass right through the shown data.

1.4   Heat Transfer Results for Cylinders in Cross-Flow

The results of the heat transfer part of the problem defined in section 1.2 are summarized as an average Nusselt number

$$Nu = \frac{h D}{k} \tag{1.14}$$

The rate of heat transfer between the fluid and the wetted area A in any control volume of the computational domain is

$$q = h A \Delta T_{lm} = \dot{m} c_p (T_{out} - T_{in}) \tag{1.15}$$

where $\dot{m}$ is the mass flowrate through the domain (Fig. 1.1, bottom). The relation between Nu and the nondimensional formulation presented in section 1.2 is

$$Nu = \frac{\tilde{F} Re_D Pr (\theta_{out} - \theta_{in})}{\tilde{A} \theta_{lm}} \tag{1.16}$$

where $\tilde{A} = A/D^2$ and

$$\theta_{lm} = \frac{\theta_{out} - \theta_{in}}{\ln\left[(1 - \theta_{in})/(1 - \theta_{out})\right]} \tag{1.17}$$

$$\tilde{F} = \int_{\tilde{A}_{flow}} U \, d\tilde{A}_{flow} \tag{1.18}$$
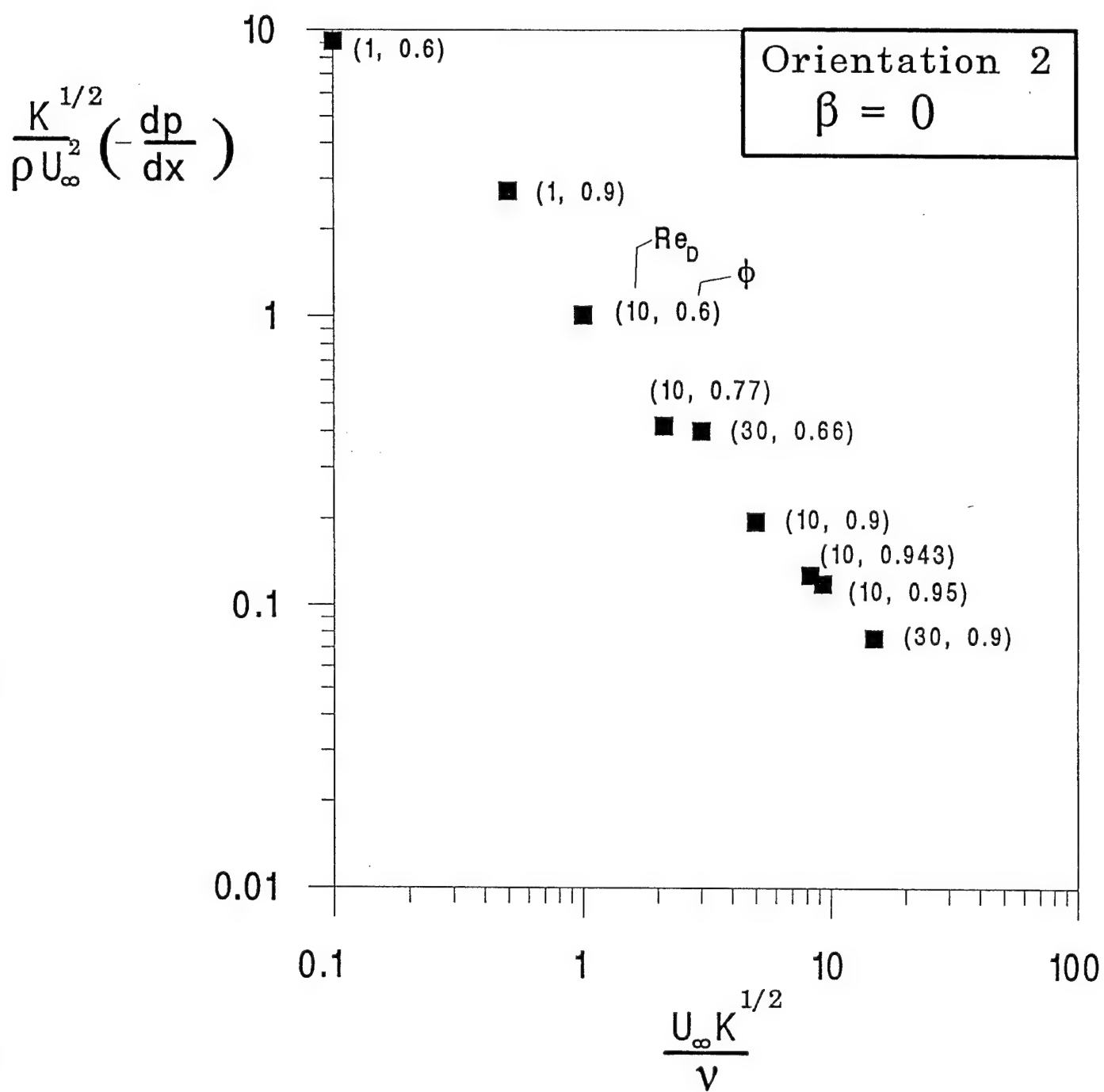
7

Figure 1.3   Porous-medium correlation of the pressure drop results for crossflow.
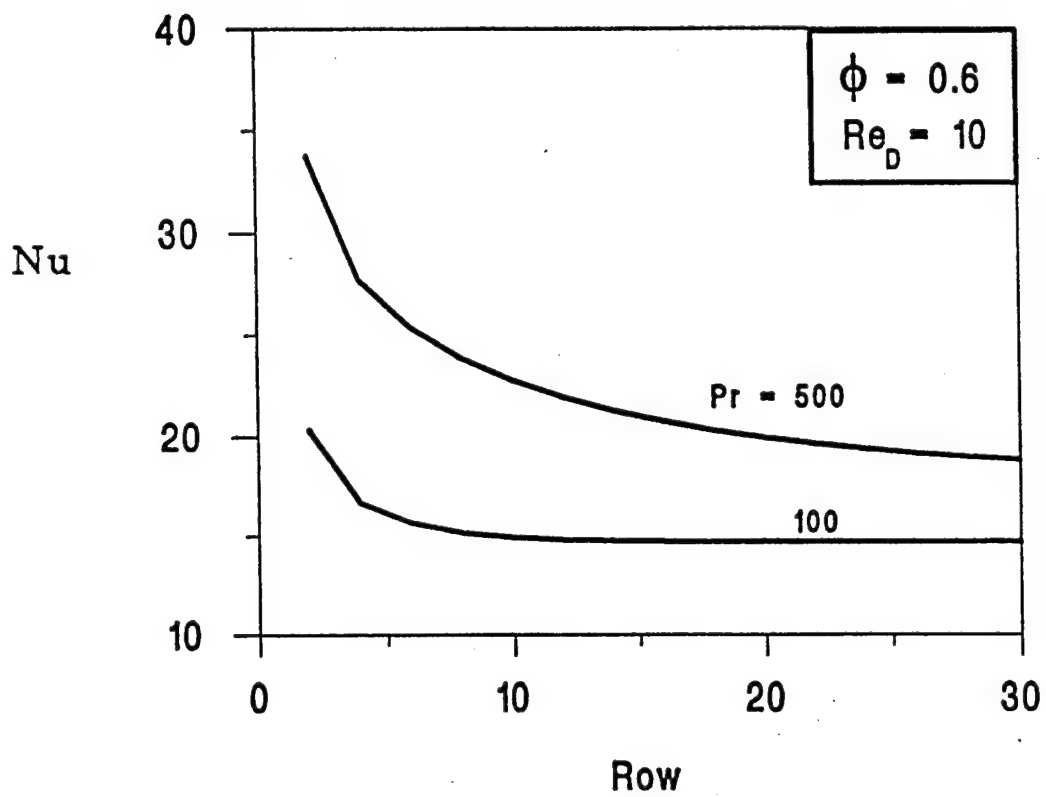
8

Figure 1.4   The local (row) Nusselt number as a function of Pr and longitudinal position.

Experimental studies usually report Nu averaged over the entire array, because that value is experimentally accessible. We calculated the "local" Nusselt number associated with (averaged over) a certain row of cylinders in order to monitor the thermal development of the flow, from one row to the next.

The results obtained for $\beta = 0°$ show that in general the row Nusselt number Nu in the first few rows is larger than in later rows. This trend is illustrated in Fig. 1.4. We found that the Nu value for the first row was very sensitive to grid refinement. After a few rows Nu approached a constant, which was less sensitive to grid refinement. Our convergence tests were based on the stability of the constant Nu value found between rows 7 through 31.

The only correlation for low Reynolds number heat transfer for staggered tube banks in cross-flow appears to be a formula due to Zukauskas (1987a):

$$Nu = 1.04 \, Re_{D,f}^{0.4} \, Pr^{0.36} \left(\frac{Pr_f}{Pr_w} \right)^{0.25} \tag{1.19}$$

where Nu is the value for "inner rows", and $Re_{D,f}$ is based on the velocity averaged over the minimum cross section. Equation (1.19) was recommended for the range $1.6 < Re_{D,f} < 40$. The subscripts f and w indicate that the properties must be evaluated at the flow mean temperature and, respectively, the cylinder surface temperature.

Our results for fully developed cross-flow in the range $1 \le Re_D \le 30$ and $0.72 \le Pr \le 100$ are correlated by the power law

$$Nu = c \, (Re_D \, Pr)^n \tag{1.20}$$

for which the constants c and n are reported in Table 1.1. The agreement between the numerical Nu values and the values obtained based on equation (20) is within 4 percent.

The most important difference between the correlations (1.19) and (1.20), is the smaller exponent n (i.e. weaker Re_D and Pr effect) present in equation (1.20). To understand these differences we examined the experimental and numerical work on which equation (1.19) is based (Omohundro et al., 1949; Bergelin et al., 1949, 1950). For example, equation (1.20) underestimates by a factor of 2 the Nusselt number found experimentally by Bergelin et al. (1950) for $Pr \cong 500$. The numerical work of Chang et al. (1989), which was performed for $Pr = 0.7$, agrees with the Bergelin et al. experiments when a $Pr^{0.33}$ correction factor is applied to the Nusselt number. The agreement between Bergelin et al. and Chang et al. is due to the shortness of the arrays studied (10 rows for Bergelin et al., and 5 rows for Chang et al.), and explains why equations (1.19) and (1.20) are different.

Table 1.1. Constants for the fully developed Nusselt number correlation (1.20).

ϕ	c	n
0.6	5.64	0.14
0.9	2.34	0.18
0.95	2.0	0.18

Figure 1.4 illustrates the effect of Prandtl number on the local Nusselt number over the first 30 rows. When we examine our numerical results for the first ten cylinder rows we find that the Nusselt number averaged over ten rows scales as $Pr^{0.3}$, and that our numerical simulation agrees with the findings of Bergelin et al. to within 10 percent. Nonetheless at later rows where the flow is fully developed, our correlation (20) applies. For flow systems in which the flow becomes fully developed early in the array, it is clear that Zukauskas's formula (1.19) would result in significant error (although it is correct for short arrays in which entrance effects dominate).

The same explanation (fully developed flow vs. entrance flow) holds for the different exponents on the Reynolds number in equations (1.19) and (1.20). That the Nusselt number in the fully developed region is proportional to Re_D^n where n is significantly smaller than in Zukauskas's correlation (1.19) is further supported by the experiments of Minakami et al. (1993). These authors tested an array of in-line square pin fins with 10 to 20 rows in the longitudinal direction, and found that $Nu \sim Re_D^n$, where n is between 0.2 and 0.25 in the laminar regime and for $Pr = 7$ (water). Comparison of our findings with the results of Minakami et al. is reasonable because the shape of the pins (square or cylindrical) should have only a small effect in the low Re_D regime. Furthermore, Zukauskas (1987a) indicates that Nu values for staggered and in-line arrays have the same Re_D dependence for $Re_D > 40$.

1.5. Heat Transfer Results for Inclined Cylinders

Zukauskas (1972) proposed the single curve of Fig. 1.5 (top), as a heat transfer method of accounting for the effect of the angle of inclination β between the cylinder axis and the direction perpendicular to the flow. He did not indicate the Re_D range and array dimensions for which this curve is valid. Our results for fully developed flow, $1 \leq Re_D \leq 30$, $0.72 \leq Pr \leq 100$, and orientation 1 indicate that the angle effect on Nu is considerably smaller than indicated by Zukauskas.

Groehn (1981) proposed the principle of independence as a method of accounting for the effect of β on the Nusselt number. In this method the relevant velocity scale is that normal to the cylinder, hence the Reynolds number that should be used in equation (1.20) is $Re_D \cos \beta$. If the principle of independence is valid then the ratio $Nu(\beta) / Nu(0°)$ should be a function of ϕ and β
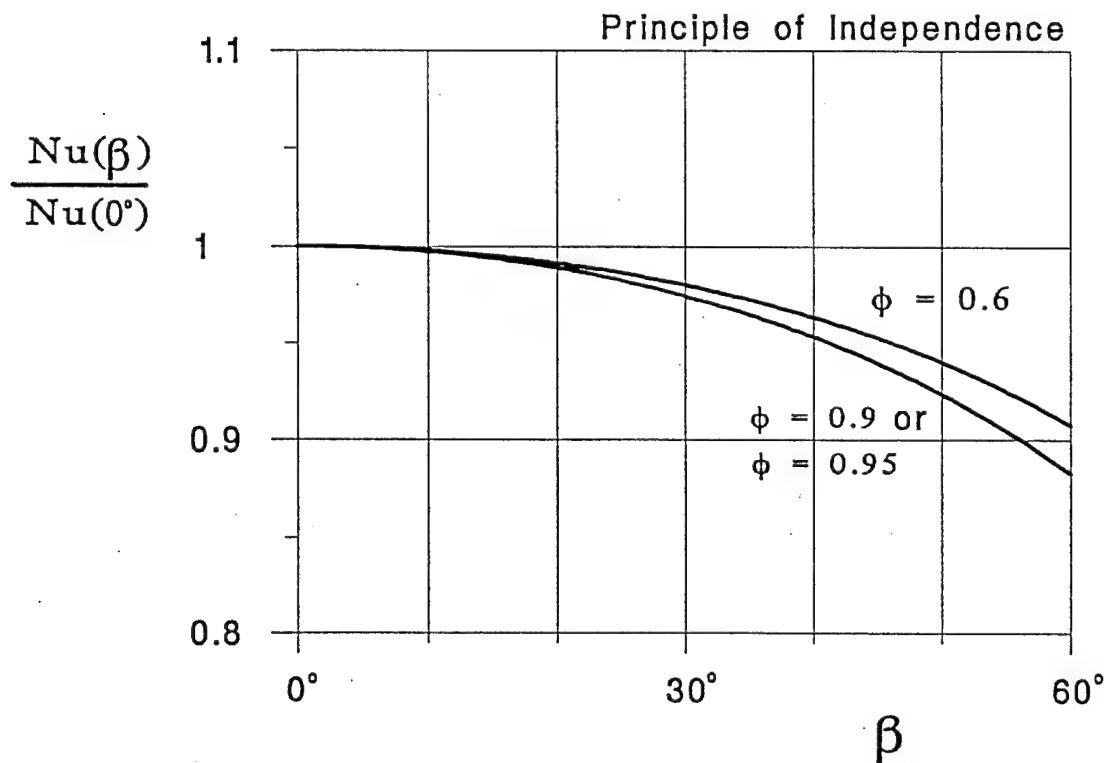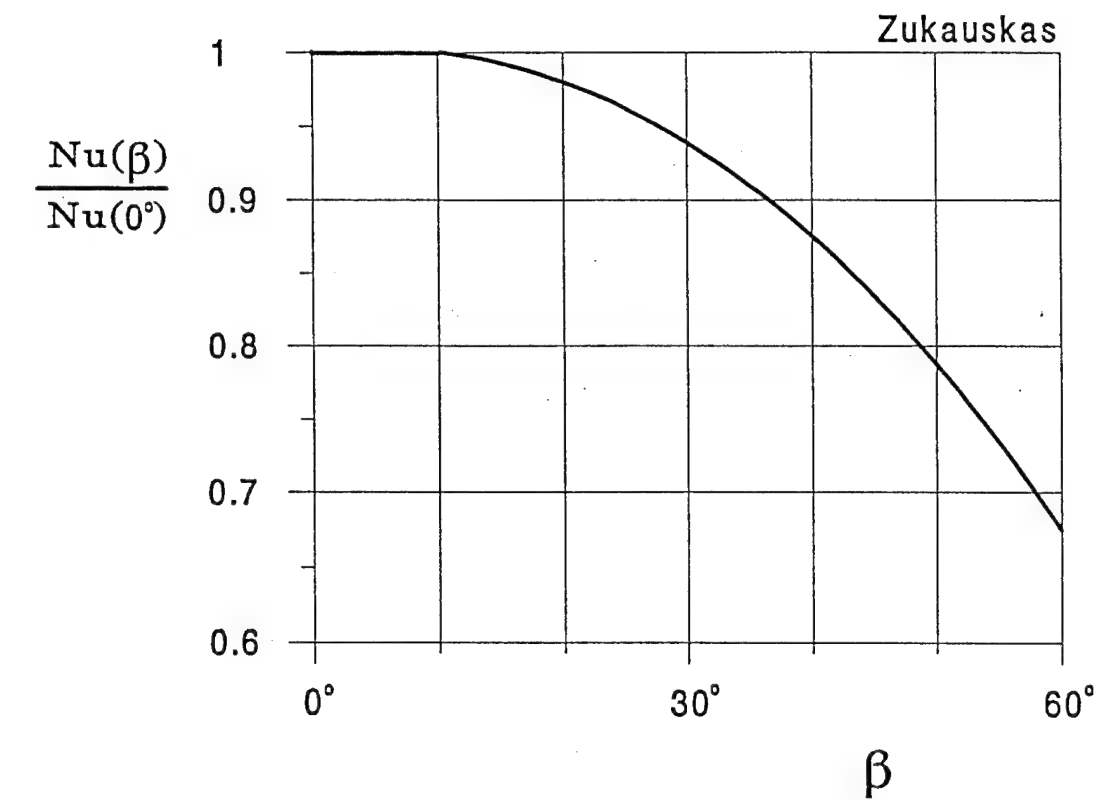
11

Figure 1.5   Top: Zukauskas's (1972) curve for the effect of the angle β on the Nusselt number;
Bottom: the principle of independence in combination with equation (1.20).

only. Figure 1.5 (bottom) illustrates the curves predicted by the principle of independence in combination with equation (1.20).

Figures 1.6a-c show how the ratio $Nu(\beta)/Nu(0°)$ responds to changes in β, ϕ and Pr when Re_D is fixed. An interesting feature is the evolution of the $Pr = 7$ curve (e.g. water) as the porosity increases from 0.6 to 0.95. The $Nu(\beta)/Nu(0°)$ curve moves upward as ϕ increases, and this means that the angle effect is weaker in a sparse array than in a dense array. In particular, when $\phi = 0.95$ and $0° < \beta \leq 45°$ the Nusselt number for inclined cylinders is greater than for the same array in cross-flow. This feature is almost the same as in the experimental results of Willins and Griskey (1975), who measured the mass transfer from a single cylinder inclined relative to a uniform flow. In the Willins and Griskey experiment the group Re_D Sc was of the order of 10^4 (note that Re_D Sc is the mass transfer equivalent of the Peclet number in forced convection heat transfer). In Fig. 1.6c, the $Pr = 7$ curve corresponds to $Pe_D = 70$, which is the highest Peclet number illustrated in that frame. Moreno and Sparrow (1987) found an increase in Nu at small angles β in flow through tube banks at $Re_D \sim 10^4$ if the cylinders were in line, but not if they were staggered. As our array becomes more sparse, it more closely approximates the in-line configuration. In conclusion, Fig. 1.6c, Willins and Griskey's and Moreno and Sparrow's results suggest that the increase in $Nu(\beta)$ above $Nu(0°)$ in a small β range is a high Peclet number effect visible in in-line arrays, sparse staggered arrays or isolated cylinders.

Figure 1.7 shows how the Nusselt number behaves at constant Pr and constant Re_D. The curves show that the porosity has a relatively weak effect and that the ratio $Nu(\beta)/Nu(0°)$ is mainly a function of β. Again, the exception is the $\phi = 0.95$ curve in Fig. 1.7b, which shows that the porosity plays a role when the array is sufficiently sparse.

Figure 1.8 shows that the Re_D effect is such that $Nu(\beta)/Nu(0°)$ increases when Re_D increases. This is interesting because it means that the $Nu(\beta)/Nu(0°)$ curve becomes less and less like Zukauskas's curve (Fig. 1.5) as Re_D increases. This trend is the opposite of what we found in the results for the pressure drop, where the $\Delta P(\beta)/\Delta P(0°)$ curve approached Zukauskas's curve as Re_D increased (Fig. 1.2a).

Finally, in Figs. 1.9a, b we show that when the Peclet number ($Pe_D = Re_D$ Pr) is held constant (of order 100), the ratio $Nu(\beta)/Nu(0°)$ is essentially a function of β only. Plotted are two curves ($Pe_D = 70$ and 100) for $\phi = 0.6$ and $\phi = 0.9$, and a single point ($Re_D = 30$, $Pr = 3.3$) for $\phi = 0.6$. Comparing this finding with the relative pressure curves of Fig. 1.2 leads to the conclusion that when the relative pressure curve is independent of Re_D, (namely, when $Re_D \leq 10$), the ratio $Nu(\beta)/Nu(0°)$ is a function of β and Pe_D, and not of Re_D and Pr separately.

The dependence of $Nu(\beta)/Nu(0°)$ on Pr and Re_D indicates that the principle of independence does not hold in a strict sense. It does, however, provide a good order-of-magnitude estimate for the effect of β. That the principle of independence does not hold exactly
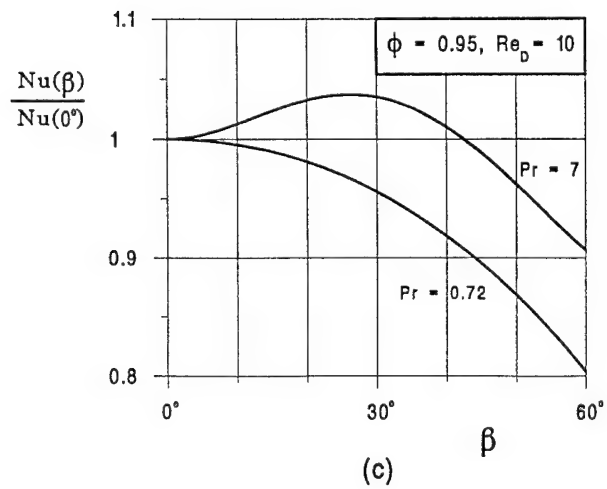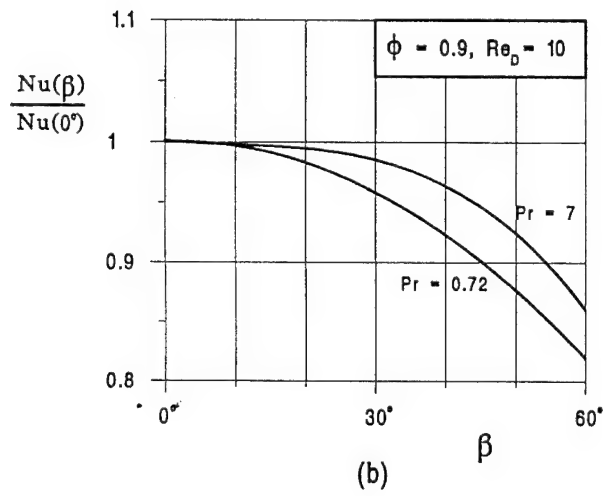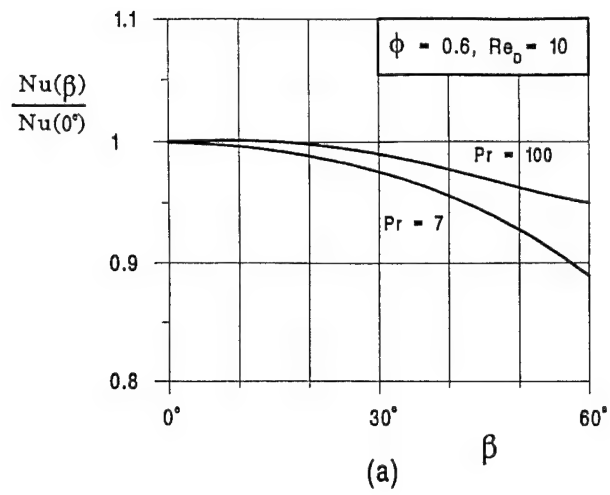
Figure 1.6   The effect of angle of inclination, Prandtl number and porosity on the Nusselt number (Re$_D$ = 10).

14
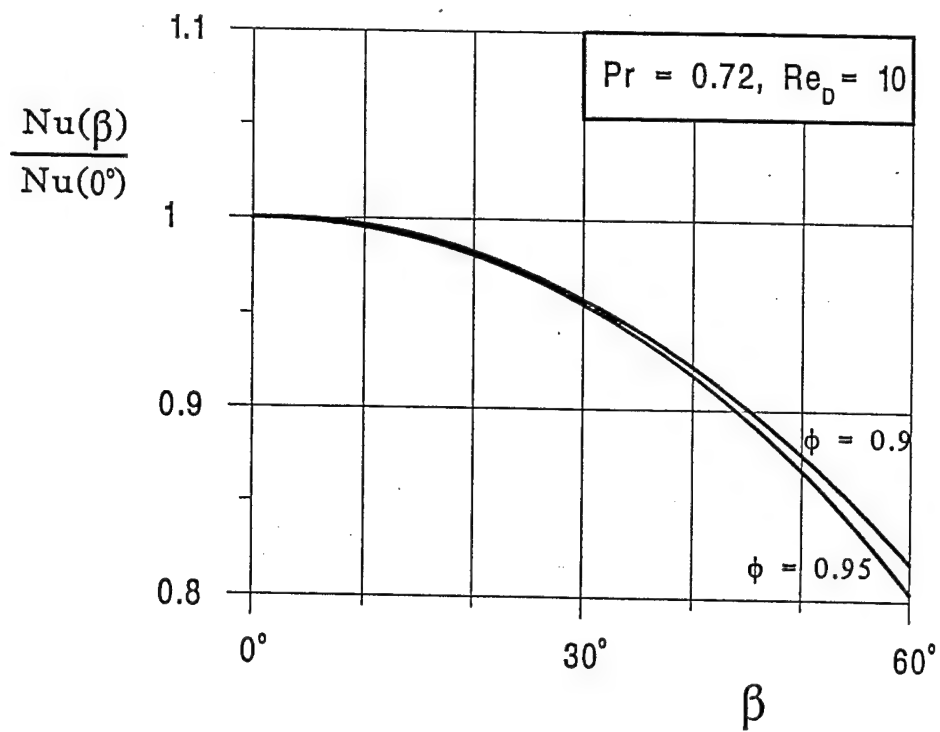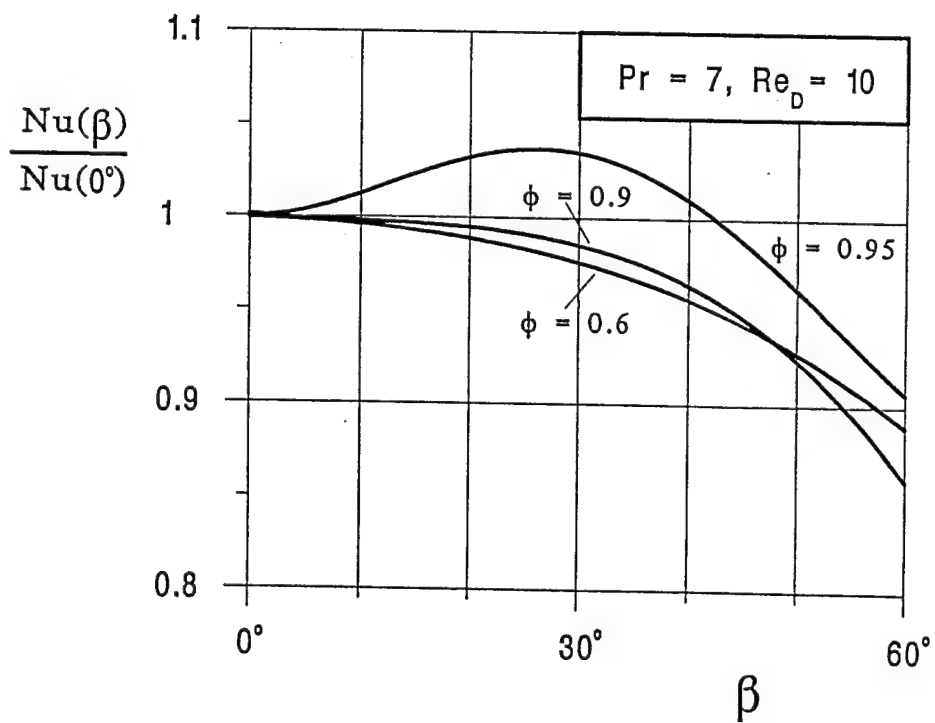
Figure 1.7   The effect of angle of inclination and porosity when Re_D and Pr are fixed.
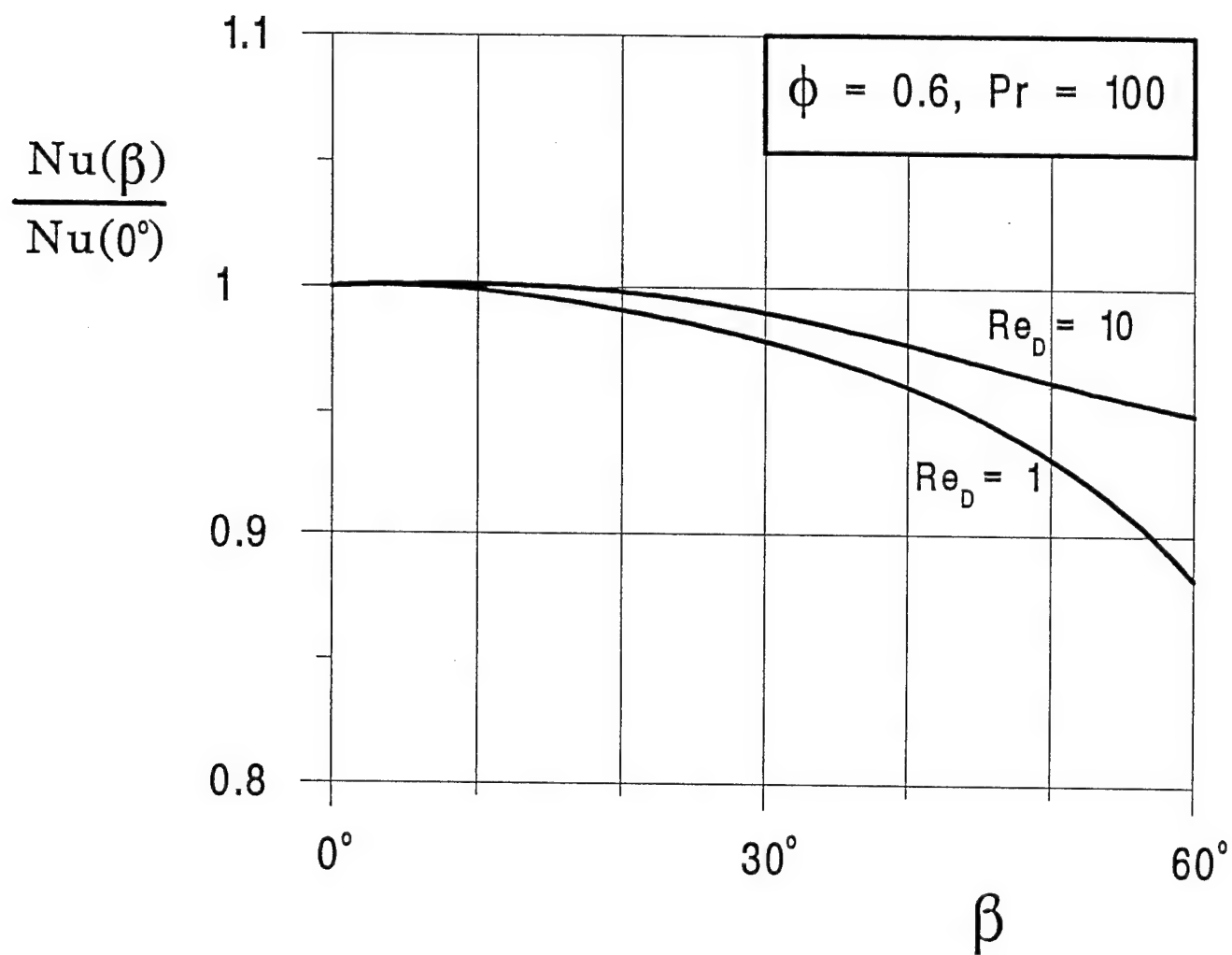
Figure 1.8   The effect of the Reynolds number on the Nusselt number of an inclined array.
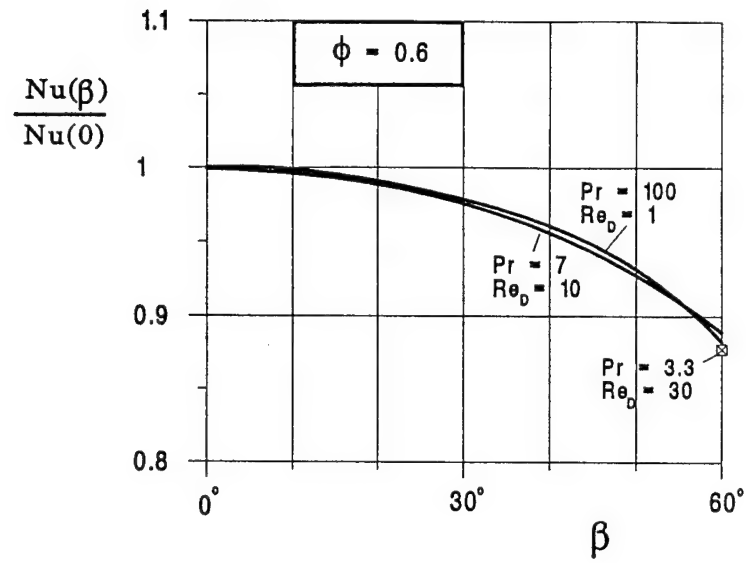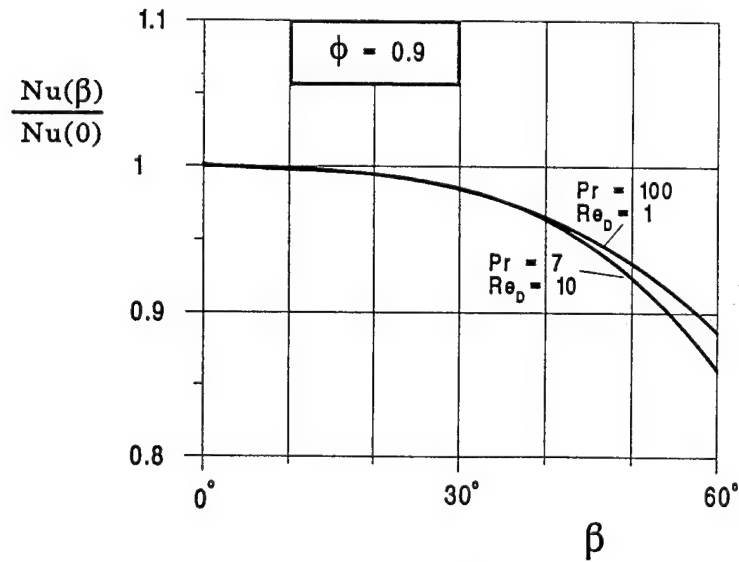
Figure 1.9   The angle effect on the Nusselt number when the array is dense and the Peclet
              number is fixed.

in the low Re_D regime is reasonable, since this principle is based on the assumption that the flow away from the cylinder surface is inviscid.

The most important aspect of the heat transfer results presented in this section is that at low Reynolds numbers the effect of cylinder inclination is relatively small, regardless of the Peclet number. For example, if the β effect is ignored in the estimation of Nu in the β range 0°-60°, the error in Nu is less than 20 percent.

1.6   Experiments for Pressure Drop

We verified the accuracy of our numerical results by measuring in the laboratory the pressure drop across a long bundle of cylinders with several inclinations ($\beta = 0°, 45°, 60°$) and at low Reynolds numbers ($8 \leqslant Re_D \leqslant 50$). We chose to test the pressure drop calculations because they represent the most critical part of the results described until now, since the effect of cylinder inclination is much greater on the pressure drop than on the heat transfer coefficient. We needed to verify that our computational domain captured correctly the three-dimensional flow effects present in an array with many yawed and long cylinders. Earlier experimental studies of low-Re_D flows through cylinders in cross-flow (Omohundro, 1949; Bergelin et al., 1949, 1950) were limited by the fact that the arrays were too short, and the flows were not fully developed. Furthermore, we could not find any experimental reports on low-Re_D flows through inclined cylinder arrays.

1.6.1   Apparatus. The main features of the experimental apparatus are shown in Fig. 1.10. We constructed an array with 12 cylinders across and 115 cylinders in the flow direction, with the cylinders arranged in the configuration indicated as orientation 1 in Fig. 1.1. The length of the array was 60 cm. The cylinders were made of 0.07 inch (1.8mm) rubber O-ring stock. They were 7.4 cm long and spaced in equilateral triangles with side length of 6mm. When the cylinders were oriented across the flow ($\beta = 0°$) the porosity of the array was $\phi = 0.92$. The channel height to cylinder diameter ratio was 420:1. In order to change the fiber angle, the wall of the lower channel was shifted longitudinally and upward, such that the total fiber length remained the same (7.4 cm) but the distance between the top and bottom of the channel changed, and the fiber angle changed. When $\beta = 60°$ the channel height to cylinder ratio was 210:1 and the porosity was $\phi = 0.84$.

The fiber channel was connected to a 2 m tall tank into which fluid could be pumped, thereby developing a pressure head to drive flow through the array. Six manometers were spaced along the channel so that pressure measurements could be made in the region of fully developed flow. The fluid drained out of an opening at the end of the fiber channel into a settling tank, from which it was siphoned into the pumping tank and re-pumped into the head tank.
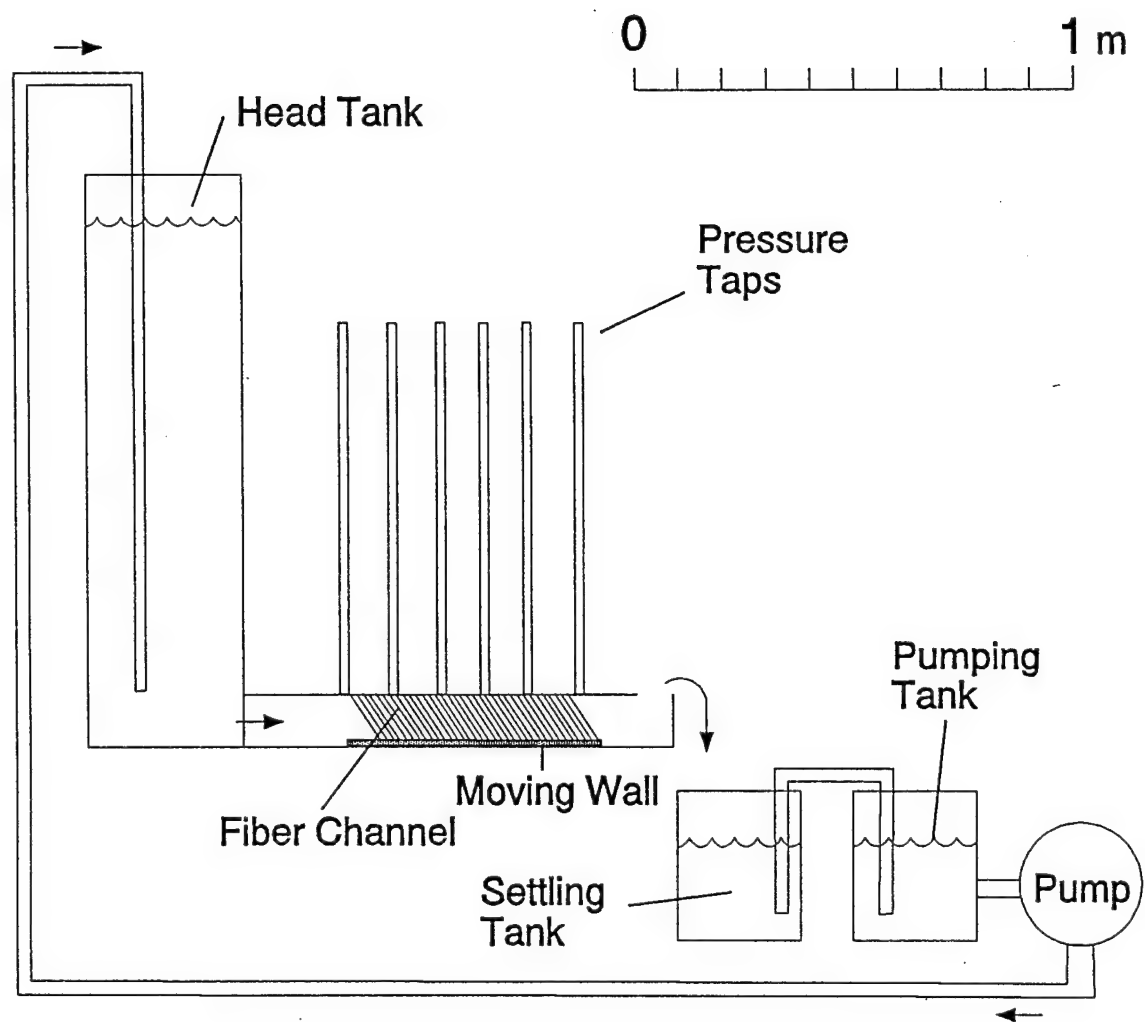
Figure 1.10 The main components of the experimental apparatus.

The pump operated at constant flow rate during each run, so that the height of the fluid column in the head tank adjusted itself until the flowrate through the fiber channel matched the flowrate into the head tank. We measured the flowrate by timing the filling of a container placed under the exit from the fiber channel. The fluid was a solution of corn syrup and water (ratio 1:3 by volume) with a kinematic viscosity between $7\text{-}8 \times 10^{-6}$ m^2/s. The viscosity depended on the temperature and the concentration of corn syrup, and varied from day to day but was stable during a series of consecutive runs. It was measured after each run with a Cannon-Fenske type viscometer.

The pump was a variable speed Simer shallow well pump. The manometers were glass tubes with 4 mm inside diameter and 1m height. The head tank and the walls of the fiber channel were made of Lexan. The fibers (total number $\approx$ 1380) were tied on the back side of orifices drilled in the top and bottom walls of the fiber channel, and sealed with RTV silicone sealant. The fibers were pulled tight to prevent bending during operation. No bending or vibration of the fibers was observed; however, only the outermost fibers could be seen, due to the density of the fibers.

1.6.2 Procedure. The pump was set at a certain flowrate. After the pump had run for a few minutes, to let the bubbles flow out and to allow the head tank to reach its equilibrium height, the liquid levels in the manometers were read and recorded. Then the fill time for a one-gallon container collecting fluid at the fiber channel exit was measured five times. Finally, the manometer levels were read again to make sure that steady state had been achieved.

Four of the manometers were positioned in the region of fully developed flow. After a few runs it became clear that it was going to be unusual to produce a run in which all four manometers were bubble free at the time of measurement. In order to maintain consistency between runs, the reading of one manometer was discarded from every run. Pressure was determined by the relationship $P = \rho gh$, where ρ is the measured fluid density, g is gravitational acceleration, and h is the height of the column measured in the manometer. The fluid density was measured by weighing a 10 ml fluid sample. A 95 percent confidence interval was calculated based on the three pressure measurements. Only in the case of one run was the precision error found to be greater than 5 percent, and the run was discarded. All other runs for which all of the necessary measurements could be made were included in the reported results.

The longest and shortest measured times for flowrate were discarded, and the remaining three times were averaged to find the flowrate and to calculate the precision error. The fluid velocity derived from this measurement was the average channel velocity, which is equivalent to the inlet velocity U_∞ used in the numerical simulations.

1.6.3 Error Analysis. All errors were calculated using 2 standard deviations as the 95 percent confidence interval. There were four sources of precision error in this experiment

(random errors and unsteadiness): the height measurements in the manometers P_h, the kinematic viscosity measurements P_v, the density measurements P_ρ, and the flowrate measurements P_F. The precision errors P_h and P_F changed from run to run. The precision error for density ($P_\rho/\rho \sim$ 0.07 percent) was negligible compared to other errors and did not vary from run to run. Repeated tests for kinematic viscosity in which fluid samples were taken from different tanks in the system indicated that $P_v/v = 2.2$ percent.

The bias, or the fixed errors for height and distance measurements, were calculated assuming that our ruler was accurate to within ± 0.5mm. Because the heights being measured changed depending on flowrate, B_h/h varied with each run, from 0.5 to 4 percent. The fixed error for the gallon container was estimated by repeated calibration against highly accurate volumetric measuring containers, and was found to be 1 percent. Due to the extremely accurate containers, scales and viscometer calibration, the bias errors for those measurements were negligible compared with the height and gallon volume errors. The non-negligible bias errors and the precision errors that did not vary from run to run are listed below:

P_v/v	B_x/x	B_v/V	P_ρ/ρ
2.19%	0.5%	1%	0.07%

The 95 percent confidence was determined by combining all bias and precision errors using the root-sum-square method, and is indicated graphically for each point plotted in Figs. 1.11 and 1.12. The data scatter falls within the estimated errors.

1.6.4 Results. Figure 1.11 shows the experimental points for $\beta = 0°$, and the corresponding numerical results (the solid line). Note again that U is the volume averaged velocity, equivalent to U_∞ of the numerical simulations. The Reynolds numbers covered by the data vary from 10 to 50. Our numerical solution becomes less accurate for $Re_D > 30$. A possible explanation for this is that the experimental system enters the transition to the turbulent regime for higher Re_D. This behavior is suppressed in our numerical simulation by the assumption of impermeable side walls for the computational domain. These boundary conditions do not allow the flow to meander. The numerical and experimental results show very clearly that for low Re_D the flow is approximately Darcy flow, and that the numerical simulation predicts the permeability of the array extremely well.

Figure 1.12a shows the experimental results for $\beta = 60°$ compared with the numerical solution that corresponds to the experimental geometry. The number of elements, the boundary conditions and general configuration used in the simulation were the same as those used in our earlier numerical work (sections 1.2 and 1.3). An adjustment was made to account for the specific geometry of the experimental system. Unlike our earlier numerical work, in the
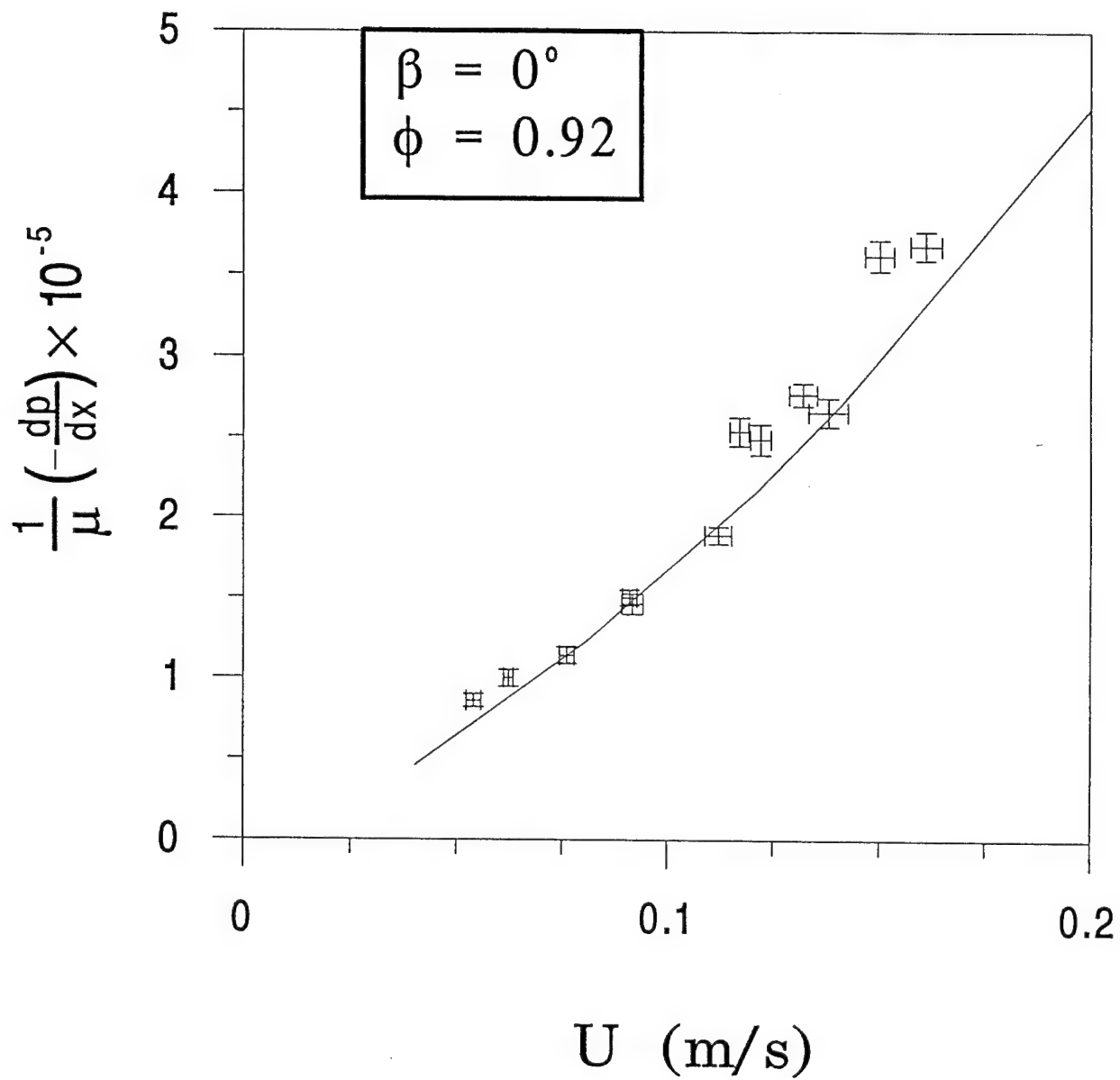
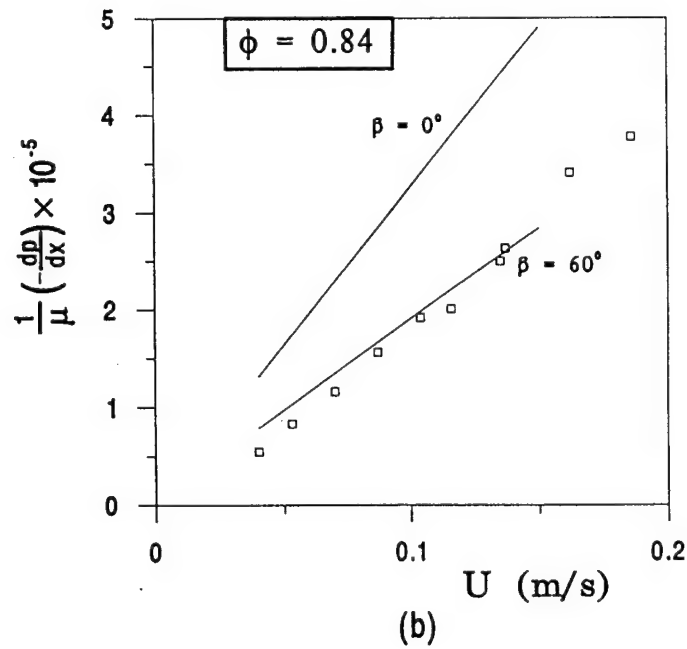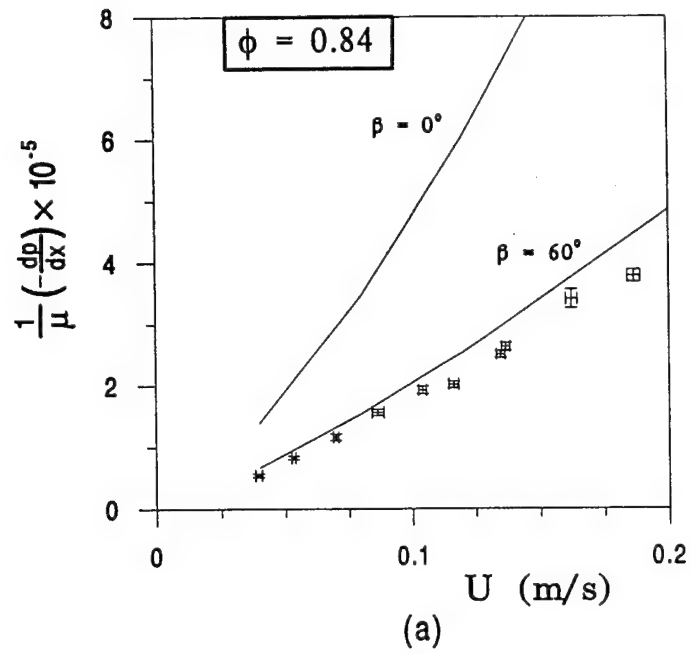Figure 1.11 Comparison between the experimental and numerical results for cylinders in cross-flow.

Figure 1.12 Cylinders inclined at 60° relative to the cross-flow position: (a) Comparison between experimental and numerical results, and (b) Comparison between the porous medium model (1.12) and the experimental results.

experiment the porosity is a function of the angle β, and the fibers are no longer arranged in equilateral triangles when $\beta \neq 0$. The two curves in Fig. 1.12a show the numerical solution for the experimental geometry at $\beta = 0°$ and $60°$. The agreement between the experimental and numerical results is excellent.

The results illustrated in Fig. 1.12a cover the Re_D range 10-50. In the $\beta = 60°$ array, where the porosity is lower than when $\beta = 0°$, the Darcy regime covers a wider Re_D range, and our numerical results agree with the measurements reasonably well over the entire Re_D domain.

Figure 1.12b shows the experimental data for $\beta = 60°$ next to the prediction based on the porous medium flow model, equation (1.12). In this model we combined the permeability from equation (1.13) with the angle effect documented in Figs. 1.2b and 1.2d. The agreement between the proposed model and the experimental data is excellent. We cannot make a similar comparison for $\beta = 0°$ because it falls outside the Darcy regime (the array orientation is 1, and the porosity is greater than 0.9).

Figure 1.13 shows the experimental and numerical results for $\beta = 45°$. There are no error bars on these data points because in this configuration we could not verify the precision error: the angle was such that the entrance and end region effects penetrated to two of the central pressure taps that were supposed to be in the fully developed flow region. Thus only two pressure taps were in the fully developed region, and only one pressure gradient measurement was possible. The pumping mechanism was not precise enough to duplicate exactly the flow conditions for two successive runs, and, therefore, to repeat runs while holding the velocity constant was not possible. Instead the experiment was run repeatedly at approximately the same flowrate. If repeated pressure gradient measurements indicated that the first run was not corrupted by an unseen bubble or other anomaly - i.e. if two runs of roughly the same flowrate showed roughly the same pressure drop - the measurement produced by the first run was plotted. The consistency of the data plotted in Fig. 1.13 is strong evidence that the measurements are sufficiently accurate, and they agree very well with the numerical prediction.

1.7. Conclusions

In this chapter we documented the pressure drop and heat transfer characteristics of flows through bundles of parallel cylinders when

    (a) the Reynolds number is low,

    (b) the flow is hydrodynamically and thermally fully developed, and

    (c) the cylinders may be inclined relative to the flow direction.

These three aspects had not been documented before, yet they are very important in applications with length scales smaller than the scales of conventional heat exchanger technology.

24
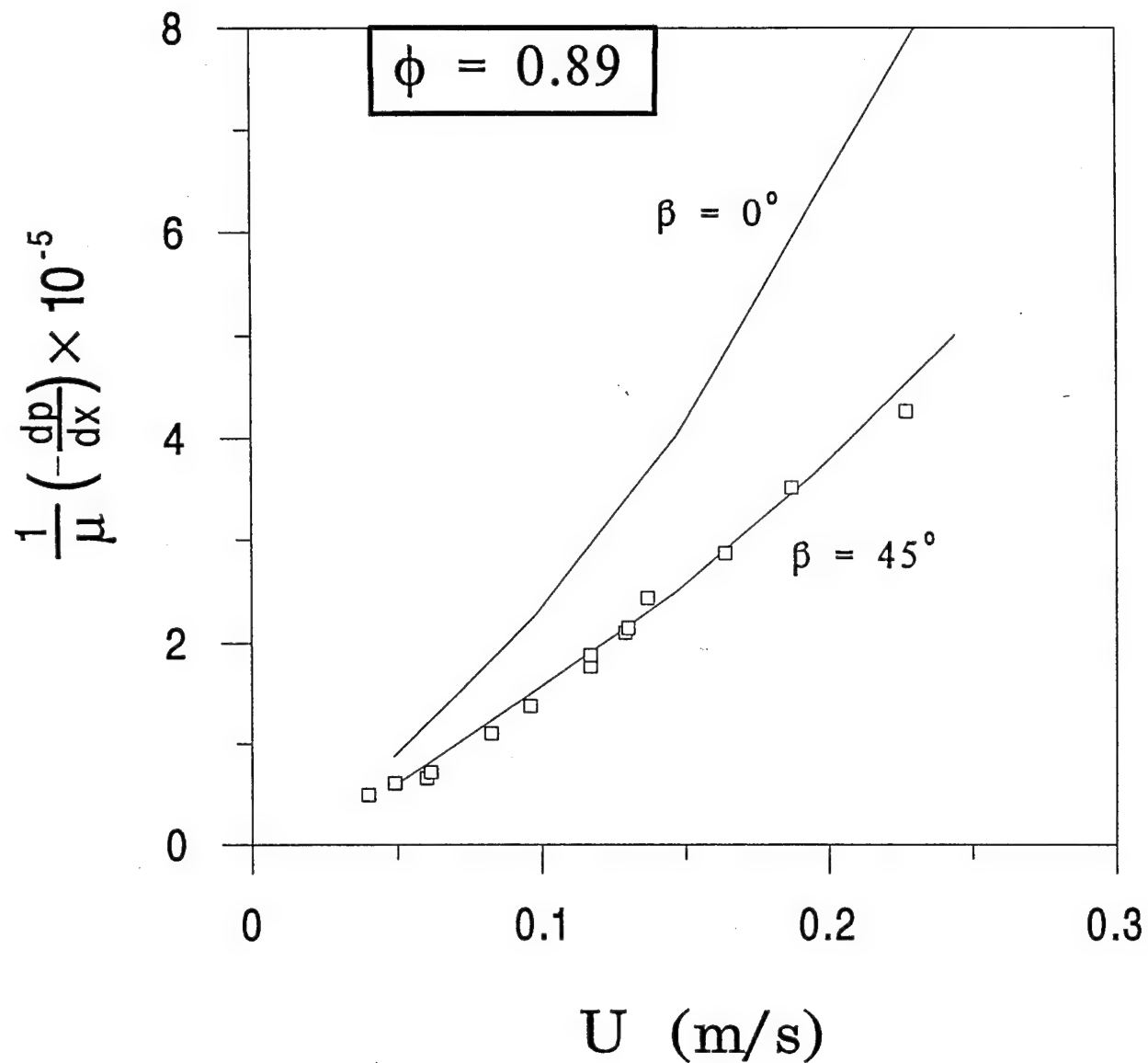
Figure 1.13 Comparison between the experimental and numerical results for the array inclined at 45°.

The results of this study demonstrate that the parametric domain represented by aspects (a)-(c) requires special attention, and that significant errors may occur if the available large-scale (heat exchanger-type) information is extrapolated to smaller scales. For this reason, a useful direction for future research would be to generate more data for pressure drop and heat transfer in the domain (a)-(c). Another direction would be to widen the Reynolds number range to Re_D values as high as 100, i.e. to cover the transitional regime where the flow behind each cylinder meanders (e.g. Minakami et al., 1993) and the symmetry assumed in Fig. 1 (top) breaks down.

1.8   Notation

A	wetted area
$\tilde{A}$	dimensionless wetted area
$\tilde{A}_{flow}$	dimensionless flow cross-sectional area
$B_{h,v,x}$	bias errors
c	constant
c_P	fluid specific heat at constant pressure
D	cylinder diameter
$\tilde{F}$	dimensionless mean velocity, equation (1.18)
H	height of computational domain
$\tilde{H}$	dimensionless height
K	permeability of porous medium
L	length of computational domain
$\tilde{L}$	dimensionless length
n	constant
Nu	row Nusselt number
p	pressure
P	dimensionless pressure
Pr	Prandtl number
$P_{h,F,v,\rho}$	precision errors
r	exponent

26

Re_D	Reynolds number
S	distance between cylinder centers
T	temperature
T_0	surface temperature
T_∞	inlet fluid temperature
u_i	velocity components
u,v,w	velocity components
U,V,W	dimensionless velocity components
U_∞	inlet velocity
W	width of computational domain
$\tilde{W}$	dimensionless width
x,y,z	cartesian coordinates
X,Y,Z	dimensionless cartesian coordinates
α	fluid thermal diffusivity
β	angle, Fig. 1.1
ΔT_{lm}	log-mean temperature difference
θ	dimensionless temperature
μ	viscosity
ν	kinematic viscosity
ρ	fluid density
ϕ	porosity

Chapter 2

FORCED CONVECTION FROM A SURFACE COVERED WITH FLEXIBLE FIBERS

2.1 Introduction

In this chapter we document the fundamental friction and heat transfer characteristics of a surface covered by a layer of flexible fibers. The associated forced convection phenomenon has important applications in several fields, for example, the enhancement of heat transfer, the control of the boundary layer, heat and mass transfer from plant canopies, and biological oceanagrophy, where suspension feeders and plant life are affected by the local flow behavior. Our own interest in surfaces covered with flexible fibers was stimulated by questions of how to maximize the insulation effect of hair on mammals.

The model and flow configuration described in this paper have as starting point the recent work on modelling convection through porous media in contact with fluids. In natural convection, the interaction between the flow through the porous medium and the flow of the pure fluid was documented by Poulikakos (1986) and Sathe *et al.* (1988). Forced convection was documented by Vafai and Thiyagaraja (1987) and Poulikakos and Kazmierczak (1987). Relative to these studies and our own work on surfaces covered with hair, the present study focuses on two new aspects:

1. The fibers that form the porous layer are flexible, and

2. The external flow is originally perpendicular to the surface.

Aspect (1) deserves scrutiny because when the fibers are flexible the interaction between the porous medium and the external fluid is more complex than when the fibers are rigid. The flow that penetrates the porous layer can change the local properties (directional permeabilities) of the solid matrix, which in turn influence the flow.

Aspect (2) is a more realistic geometric feature of the flow past a finite-size body covered with fibers (e.g. the body of a mammal). The approaching fluid strikes the body perpendicularly, penetrates the fiber cover in the stagnation region, and later flows parallel to the surface and around the body.

2.2 Physical Model

The outer flow. To study the effects of fiber cover and fiber bending we selected the convection heat transfer configuration shown in Fig. 2.1. The flow enters the computational

28

domain ($y = y_0$) with uniform velocity (U_∞) and temperature (T_c). The solid impermeable wall ($y = 0$) is maintained at a different temperature (T_h). The flow and temperature fields are symmetric about $x = 0$. In the region above the fibers ($y > H$), the flow is governed by the Navier-Stokes equations. The steady state conservation of mass and momentum for incompressible flow are

$$\frac{\partial u}{\partial x} + \frac{\partial v}{\partial y} = 0 \tag{2.1}$$

$$u\frac{\partial u}{\partial x} + v\frac{\partial u}{\partial y} = -\frac{1}{\rho}\frac{\partial p}{\partial x} + \nu\left(\frac{\partial^2 u}{\partial x^2} + \frac{\partial^2 u}{\partial y^2}\right) \tag{2.2}$$

$$u\frac{\partial v}{\partial x} + v\frac{\partial v}{\partial y} = -\frac{1}{\rho}\frac{\partial p}{\partial y} + \nu\left(\frac{\partial^2 v}{\partial x^2} + \frac{\partial^2 v}{\partial y^2}\right) \tag{2.3}$$

with the following boundary conditions in the plane of symmetry:

$$u = 0, \qquad \frac{\partial v}{\partial x} = 0 \qquad \text{at} \quad x = 0 \tag{2.4}$$

The pressure was set equal to an arbitrary constant ($p = 0$) at $x = L$ and $y = y_0$. The velocity components (u, v) were matched at the $y = H(x)$ interface with the volume averaged velocity components (u_f, v_f) of the flow through the layer with fibers.

$$u = u_f, \qquad v = v_f \qquad \text{at} \quad y = H(x) \tag{2.5}$$

The selection of velocity boundary conditions for the interface between a fluid and a porous medium saturated with the same fluid has generated considerable amount of work, which is reviewed in Nield and Bejan (1992). According, to the criteria developed by Vafai and Tien (1981)we do not need to include the Brinkman term in our porous flow model. It was shown by Vafai and Thiyagaraja (1987), however, that one cannot match shear stresses across the interface without the inclusion of the Brinkman term. If one does not match shear stresses then one has to account for the possibility of a slip in the tangential velocity of the pure fluid at the interface, as was demonstrated by Beavers and Joseph (1967). In this problem the flow is mainly perpendicular to the surface, therefore the pressure field, which drives the flow within the porous layer, is not a strong function of the frictional drag at the surface. The pressure field is almost completely determined by the decrease in the vertical momentum of the approaching fluid. The result of this is that the problem is insensitive to the degree of slip at the fluid-porous interface. Numerical tests indicated that if the no-slip condition is replaced with a free-slip condition, the resulting change is never greater than 2 % in the frictional drag experienced at the wall, or in the heat transfer.
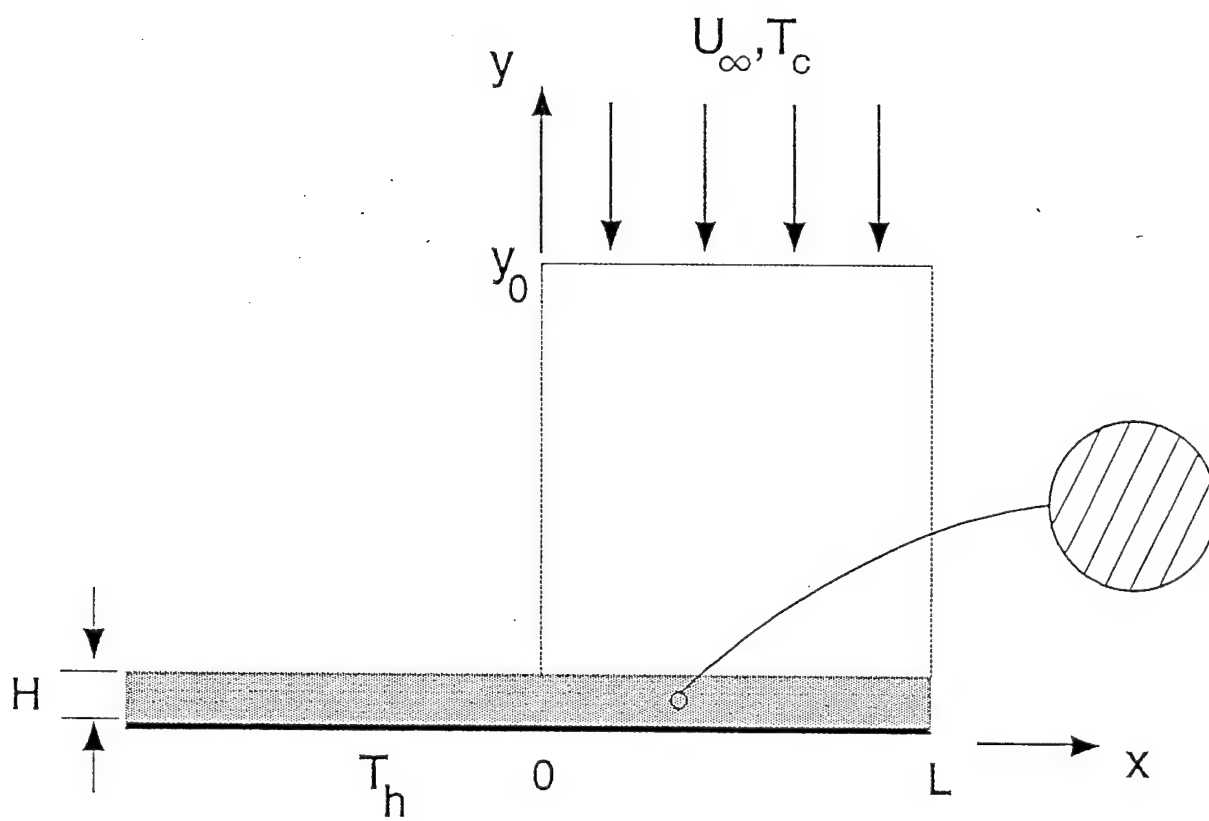
29

Figure 2.1: Two-dimensional flow against a plane surface covered with fibers.

The velocity boundary conditions for the flow out of the computational domain ($x = L$) were $\partial^2 u/\partial x^2 = 0$ and $\partial^2 v/\partial x^2 = 0$. The insensitivity of numerical results to the specification of outflow boundary conditions has been demonstrated by numerous researchers. These conditions were compared with the zero stress conditions $p - 2\mu\partial u/\partial x = 0$ and $\partial v/\partial x = 0$ at $x = L$. The results for wall friction were the same for both sets of boundary conditions, but the zero stress condition caused velocity oscillations at the outlet.

The energy conservation equation and boundary conditions for the region with pure fluid are

$$u\frac{\partial T}{\partial x} + v\frac{\partial T}{\partial y} = \alpha \left(\frac{\partial^2 T}{\partial x^2} + \frac{\partial^2 T}{\partial y^2} \right) \tag{2.6}$$

$$\frac{\partial T}{\partial x} = 0 \quad \text{at} \quad x = 0, \quad T = T_c \quad \text{at} \quad y = y_0 \tag{2.7}$$

$$\frac{\partial^2 T}{\partial x^2} = 0 \quad \text{at} \quad x = L, \quad T = T_f \quad \text{at} \quad y = H \tag{2.8}$$

In the last of equations (2.8), the fluid temperature is matched to the porous medium temperature (T_f) at the interface between the two regions. Not shown is the energy continuity equation, in which the heat fluxes are matched across the $y = H(x)$ interface.

The layer with fibers. It was assumed that the flow in the region with fibers ($0 < y < H$) is in the Darcy regime. In a representative elementary volume (r.e.v.) (Nield and Bejan, 1992) within this region, the solid matrix is a bundle of parallel equidistant fibers of diameter D. The volume-averaged flow direction almost never coincides with the local (r.e.v.) fiber direction because the outer flow is not uniform and the fibers can bend. When the flow through the fibers is perpendicular to the fiber direction, the permeability may be estimated using

$$K_\perp = \frac{D^2}{125} \left[\frac{\phi^3}{(1 - \phi)^2} \right]^{0.8} \tag{2.9}$$

In the opposite extreme, when the flow is parallel to the fibers, the permeability has been correlated by Sparrow and Loeffler (1959),

$$\frac{K_\parallel}{D^2} = \frac{-\ell n(1 - \phi) - \phi - \phi^2/2}{16\phi(1 - \phi)} \tag{2.10}$$

This correlation is valid for $\phi > 0.8$ and for fibers arranged in an equilateral triangular array.

By analogy with the irreversible thermodynamics of heat conduction through an anisotropic medium (Bejan, 1988), the Darcy flow equations for the general case where the flow is not parallel to the fibers ($\beta \neq 0$, Fig. 2.2) are
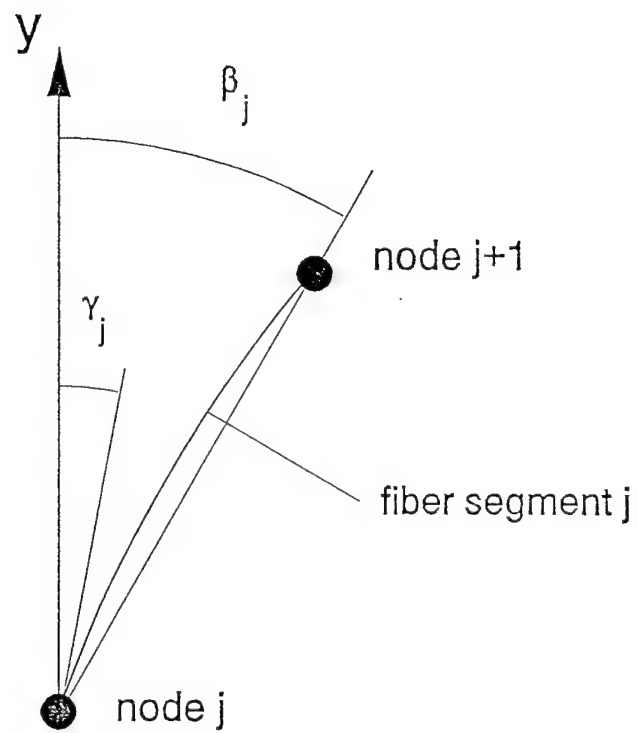
Figure 2.2: The deflection of one fiber segment

$$u_f = -\frac{K_x}{\mu}\frac{\partial p}{\partial x} - \frac{K_{xy}}{\mu}\frac{\partial p}{\partial y} \qquad (2.11)$$

$$v_f = -\frac{K_{xy}}{\mu}\frac{\partial p}{\partial x} - \frac{K_y}{\mu}\frac{\partial p}{\partial y} \qquad (2.12)$$

where

$$\begin{aligned}
K_x &= K_\perp \cos^2\beta + K_\parallel \sin^2\beta & (2.13)\\
K_y &= K_\perp \sin^2\beta + K_\parallel \cos^2\beta & (2.14)\\
K_{xy} &= (K_\parallel - K_\perp)\sin\beta\cos\beta & (2.15)
\end{aligned}$$

When equations (2.11, 2.12) are substituted into the mass conservation equation for the fiber region,

$$\frac{\partial u_f}{\partial x} + \frac{\partial v_f}{\partial y} = 0 \qquad (2.16)$$

the result is a partial differential equation for the pressure field,

$$\left(\frac{\partial K_x}{\partial x} + \frac{\partial K_{xy}}{\partial y}\right)\frac{\partial p}{\partial x} + K_x\frac{\partial^2 p}{\partial x^2} + \left(\frac{\partial K_{xy}}{\partial x} + \frac{\partial K_y}{\partial y}\right)\frac{\partial p}{\partial y} + K_y\frac{\partial^2 p}{\partial y^2} + 2K_{xy}\frac{\partial^2 p}{\partial x\partial y} = 0 \qquad (2.17)$$

This equation allows for the fact that the permeabilities vary from one r.e.v. to another inside the fiber region. The boundary conditions for equation (2.17) are

$$\frac{\partial p}{\partial x} = 0 \quad \text{at} \quad x = 0 \qquad (2.18)$$

$$\frac{\partial p}{\partial y} = 0 \quad \text{at} \quad y = 0 \qquad (2.19)$$

$$p = p(H) \quad \text{at} \quad x = L \qquad (2.20)$$

and the condition that p is continuous across the $y = H$ interface, which is the fourth boundary condition needed. The pressure $p(H)$ is provided by the solution to the pure fluid part of the flow field. The constant pressure condition (2.20) is the better of two conditions that were tried at $x = L$. The difficulty associated with equation (2.20) is that it forces $v_f = 0$ at $x = L$. This feature causes a sharp change in the vertical velocity component across the $y = H$ interface if Re_L is large. The alternative to equation (2.20) was $\partial p/\partial x$ = constant at $x = L$. This was superior in cases where the fibers did not bend, but when

33

the fibers bent a region of highly negative pressure formed around $x = L$ and $y = 0$. This was not acceptable given that $p = 0$ was the ambient pressure, so the constant-p condition (2.20) was adopted. It must be said that either condition, constant p or constant $\partial p/\partial x$, led to similar results for friction and heat transfer over the wall region $0 < x < L$: The relative error between the two sets of results decreased from 10% at $L/H = 2$ to less than 1% at $L/H = 5$. In these L/H ratios, H is the original height of the fiber layer before it is deformed by the flow, or simply H evaluated at $x = 0$.

We now turn our attention to the thermal aspects of the model. In each r.e.v., the temperature is represented by two values, the temperature of the solid (the fibers, T_s) and the temperature of the interstitial fluid (T_f). The conduction of heat along the fiber is described by the unidirectional fin conduction model

$$k_s \frac{\partial^2 T_s}{\partial s^2} + h \frac{p_s}{A_s}(T_f - T_s) = 0 \tag{2.21}$$

where s is the curvilinear coordinate measured along the fiber (s $=0$ is the base). In each r.e.v. cut perpendicular to the fiber direction, the sum of all the fiber wetted perimeters is p_s, and the sum of all the fiber cross-sections is A_s. For each local angle of fiber inclination β, the ratio p_s/A_s is a constant dictated by the fiber diameter and the fiber density (or the porosity ϕ along the $y = 0$ wall, where all the fibers are perpendicular to the wall).

The equation for the conservation of energy in the interstitial fluid is

$$\frac{u_f}{\phi} \frac{\partial T_f}{\partial x} + \frac{v_f}{\phi} \frac{\partial T_f}{\partial y} = \alpha \left(\frac{\partial^2 T_f}{\partial x^2} + \frac{\partial^2 T_f}{\partial y^2} \right) + \frac{h}{\rho c_p} \frac{A_{ht}}{\phi V_{rev}}(T_s - T_f) \tag{2.22}$$

where V_{rev} is the r.e.v. volume, and $A_{ht}/(\phi V_{rev})$ is the ratio of the total fiber-fluid contact area present in the r.e.v., divided by the volume inhabited by fluid in the r.e.v. The thermal diffusivity α refers to the fluid alone, $\alpha = k/(\phi c_p)$. The heat transfer coefficient appearing in equations (2.21, 2.22) was estimated based on the low Reynolds number correlation developed based on the work described in Chapter 1, where it was found that in the range $0° < \beta < 60°$ the effect of β on h is negligible,

$$h = (8.46 - 6.8\phi)\frac{h}{D} \left(\frac{U_\infty D}{\alpha} \right)^{0.18} \tag{2.23}$$

This correlation is valid in the range $0.9 \leq \phi \leq 0.95, 1 \leq U_\infty D/\alpha \leq 30$, and $0.72 \leq Pr \leq 100$. The boundary conditions for equations (2.21, 2.22) are

$$T_s = T_f = T_h \text{ at } y = 0 \tag{2.24}$$

$$\frac{\partial T_f}{\partial x} = 0 \text{ at } x = 0 \text{ and } x = L \tag{2.25}$$

34

$$T_f = T \text{ at } y = H \tag{2.26}$$

$$\frac{\partial T_s}{\partial s} = 0 \text{ at the fiber end} \tag{2.27}$$

Worth noting are: the outflow condition $\partial T_f/\partial x = 0$ at $x = L$, which is commonly used in numerical studies of convection in porous media with permeable walls, the fluid temperature continuity across the $y = H$ interface, equation (2.26), and the assumption that each fiber is slender enough so that the heat transfer through its tip can be neglected, equation (2.27).

The equations and boundary conditions described until now were nondimensionalized by defining

$$(U, U_f) = \frac{(u, u_f)}{U_\infty}, \qquad (V, V_f) = (v, v_f)\frac{H}{U_\infty L} \tag{2.28}$$

$$X = \frac{x}{L}, \qquad Y = \frac{y}{H} \qquad P = \frac{p}{\rho U_\infty^2} \tag{2.29}$$

$$(\theta, \theta_f, \theta_s) = \frac{(T, T_f, T_s) - T_c}{T_h - T_c} \tag{2.30}$$

For brevity, we omit the dimensionless equations and boundary conditions, and note that they contain the following dimensionless groups:

$$Re_L = \frac{U_\infty L}{\nu}, \qquad Pr = \frac{\nu}{\alpha}, \qquad A = \frac{L}{H} \tag{2.31}$$

$$Nu_L = \frac{hL}{k}, \qquad \tilde{A}_{ht} = \frac{A_{ht}L}{\phi V_{rev}}, \qquad Bi = \frac{hL}{k_s}, \qquad \tilde{p}_s = \frac{p_s L}{A_s} \tag{2.32}$$

The fiber shape. The third component of the model contains the equations needed for calculating the shape of the fibers. This component is based on the observation that in Darcy flow the pressure gradient in the fluid is balanced by the forces exerted on the solid matrix. We assume that the fibers do not touch, i.e. that each fiber acts independently of all other fibers. Consider a small volume $dxdyW$ that contains at least one r.e.v., where $W >> L$ is the dimension perpendicular to the plane of Fig. 2.1. The components of the total force experienced by the solid parts (fiber segments) found in this volume are

$$F_x = -\frac{\partial p}{\partial x}dxdyW, \qquad F_y = -\frac{\partial p}{\partial y}dxdyW \tag{2.33}$$

The number of fibers that pass through this volume is

$$n = (\cos \beta dx + \sin \beta dy)W\frac{1 - \phi}{\pi D^2/4} \tag{2.34}$$

where $(1 - \phi)/(\pi D^2/4)$ is the fiber density (number/area) in the plane perpendicular to the local fiber direction. Dividing equations (2.33) by n yields the components of the local load experienced by a single fiber. These forces can be arranged into a stress vector $\tilde{\sigma}$: the normal and tangent forces exerted at a certain point (s) on the fiber are obtained by performing the scalar product between $\tilde{\sigma}$ and the unit normal and unit tangent vectors.

Each fiber was divided into many small segments (N), typically $N = 50$. The forces were modelled as acting on the ends of each segment. Each small segment, therefore, behaved as a beam undergoing small deflection. The normal and tangential forces were transferred down the fiber according to the equations

$$FN_j = \tilde{\sigma}_j \cdot \hat{N}_j + (\hat{N}_j \cdot \hat{N}_{j+1})FN_{j+1} + (\hat{N}_j \cdot \hat{T}_{j+1})FT_{j+1} \tag{2.35}$$

$$FT_j = \tilde{\sigma}_j \cdot \hat{T}_j + (\hat{T}_j \cdot \hat{T}_{j+1})FT_{j+1} + (\hat{T}_j \cdot \hat{N}_{j+1})FN_{j+1} \tag{2.36}$$

where the unit normal $\hat{N}$ is defined as $(\cos\beta_j, -\sin\beta_j)$ and the unit tangent $\hat{T}$ is defined as $(\sin\beta_j, \cos\beta_j)$. Following the method of Knight and Barret (1980), these forces can be used to calculate the deflection of each fiber segment, and thereby build up the shape of the entire fiber.

Figure 2.2 illustrates the node placement relative to one fiber segment, where γ_j is the local fiber angle at node j. The angle β associated with the jth segment is the angle between the y axis and the straight line segment joining the j and $j + 1$ nodes. The fiber segments that join the nodes are not necessarily straight. The mass stations that would be present in a time-dependent beam analysis are not necessary because in this study we are concerned with the steady state. Only the elastic elements are represented,

$$\gamma_j = \Delta\gamma_j + \gamma_{j-1} \tag{2.37}$$

$$\Delta\gamma_j = \frac{M_j\Delta s}{EI} + \frac{FN_j(\Delta s)^2}{2EI} \tag{2.38}$$

$$M_j = M_{j+1} + \Delta s FN_{j+1} \tag{2.39}$$

In equations (2.38, 2.39) Δs is the length of the fiber segment, E is the elastic modulus, $I = \pi D^4/64$ is the area moment of inertia, and M_j is the bending moment at node j. Equations (2.35)-(2.39) and the end conditions $\gamma = 0$ at $s = 0$, and $M_N = 0$ at the free end are sufficient for calculating all the γ_js. To calculate the position of each node, we calculate the end deflection of each segment,

$$d_j = \frac{M_j(\Delta s)^2}{2EI} + \frac{FN_j(\Delta s)^3}{3EI} \tag{2.40}$$

The position vector for node j,

$$\tilde{P}_j = \Delta s \hat{T}(\gamma_{j-1}) + d_j \hat{N}(\gamma_{j-1}) \tag{2.41}$$

where $\hat{T}$ and $\hat{N}$ are the tangent and normal vectors are calculated in terms of the angles γ_j rather than β_j. The local fiber angle can be calculated for each segment,

$$\beta_{j-1} = \tan^{-1}\left(\frac{\tilde{P}_{jy} - \tilde{P}_{(j-1)y}}{\tilde{P}_{jx} - \tilde{P}_{(j-1)x}}\right) \tag{2.42}$$

where $\tilde{P}_{jy}$ refers to the y position of the jth node, and $\tilde{P}_{jx}$ refers to the x position of the jth node. These equations were also nondimensionalized, and this brought to light a new dimensionless group that describes the relative stiffness of the fibers,

$$S = \frac{EI}{\rho U_\infty^2 L^4} \tag{2.43}$$

2.3 Numerical Method

The equations governing the flow in the pure fluid region were solved using finite differences and ADI. The pressure field was solved in order to force the conservation of mass using the auxiliary potential method (Fletcher, 1991). The grid in the pure fluid region was uniform in x, but variable in y, so that a large number of grid points could be put in the boundary layer near the porous interface, Fig. 2.3. A shearing transformation was used to map the nonrectangular physical domain, which occurs when the fibers bend, onto a rectangular computational domain. The robustness of the solver was increased dramatically by including an artificial viscosity that was non-zero only in a region with positive v. There is no artificial viscosity in the final results because all the solutions are characterized by negative v velocities.

The pressure field in the layer with fibers was also solved using finite differences and ADI. The grid in the porous region was uniform in x and y in computational space, Fig. 2.3. Another shearing transformation was used to map the irregular porous domain onto a rectangular computational space.

The equations for the fluid temperature were solved using ADI on a non-sheared grid, with the same grid point placement as the fluid equations when the fibers were unbent. The temperature in the solid was determined using time stepping with the trapezoidal rule until convergence was reached.
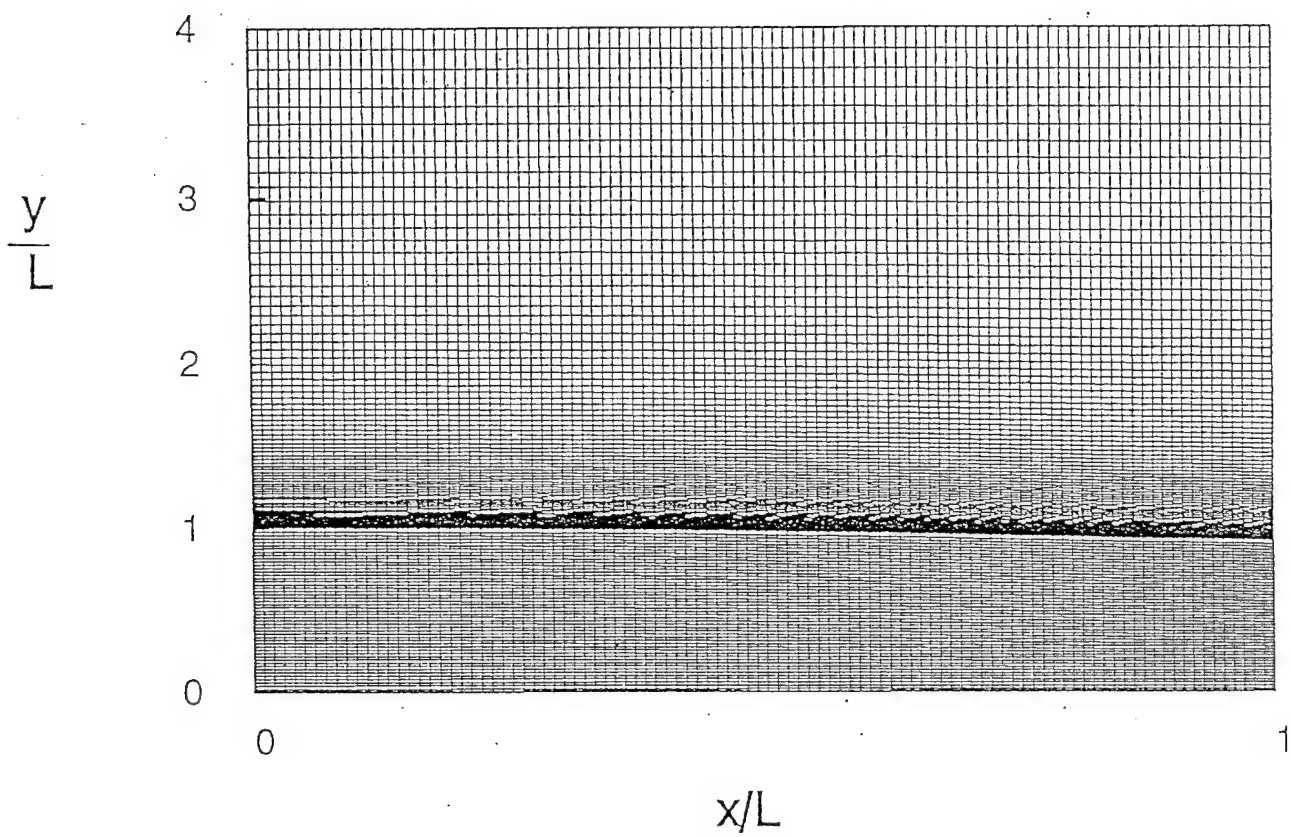
37

Figure 2.3: Example of the grid used ($Re_L = 1000, L/H = 2, \phi = 0.9, H/D = 20$)

The pure fluid velocity solution was iterated until the relative error (maximum change in velocity divided by the time step) was less than 0.1. The auxiliary potential solver was then iterated until its relative error became less than 0.001. Then the porous pressure field was solved, using the new pressure boundary conditions provided by the auxiliary potential solution. The porous pressure field was iterated until its relative error was less than 0.0001. When the fibers were bent, convergence testing indicated that a relative error of 10^{-5} was necessary.

The cycle continued until the average value of the auxiliary potential function was less than 0.001 (which indicates that continuity is being satisfied). All of these tolerances were determined doing convergence testing. In all cases, dividing any of the above convergence criteria by 2 resulted in a less than 1% change in the calculated friction force on the $y = 0$ surface. Two additional accuracy criteria that were met are that global mass conservation must be satisfied to better than 1%, and that mass conservation within the porous layer must be satisfied within 1%. The latter criterion was relaxed to 3% when the fibers underwent significant deformation. It was also found that setting $y_0 = 4L$ made the solution insensitive to further increases in the height of the computational domain.

Similarly, the fluid temperature was advanced by one time step (the size of which was determined by stability criteria) and then the solid temperature was iterated until convergence was reached, and the fluid temperature was advanced again. The system generally conserved energy to within 1% if the relative fluid temperature error was less than 0.001. In cases where the total conservation of energy was not satisfied to within 3%, error bars are attached to the plotted results.

Grid refinement tests were performed. The final grid was chosen such that further grid doubling in any direction resulted in a less than 1% change in the calculated surface friction. The final grid for $Re_L = 500$ was 101 points in x for both the porous and non-porous regions, 81 grid points in y for the pure fluid region, and 50 grid points in y for the porous region. An example of the mesh used for a solution in which the fibers are bent is illustrated in Fig. 2.3: note that the height of the porous layer decreases as x increases, because the fibers bend.

2.4 Surface with Inflexible Fibers

Before examining the effect of fiber bending on friction and heat transfer, it is necessary to understand the convection mechanism when the fibers do not bend. How stiff the fibers (or how large S) must be in this limit is one of the results presented in the next section.

The independent parameters in the system are Re_L, Pr, the porosity of the fiber layer ϕ, the aspect ratio L/H, the fiber height to fiber diameter ratio H/D, and the ratio of solid to fluid conductivities k_s/k. In this study the fluid is assumed to be air, $Pr = 0.72$. If the fibers are hairs in air then $k_s/k \cong 10$. We considered several Re_L values between 500 and 2000,

several porosities between 0.9 and 0.95, the H/D ratios 20 and 50, and the aspect ratios $L/H = 1$ through 5. The results are presented in terms of overall quantities: the average skin friction coefficient,

$$C_f = \frac{\int_0^L F''_x dx}{\frac{1}{2}\rho U_\infty^2 L} \quad \text{where} \quad F''_x = \int_0^H -\frac{\partial p}{\partial x}dy \qquad (2.44)$$

and the average Nusselt number

$$Nu_L = \frac{hL}{k} \quad \text{where} \quad h = \frac{\int_0^L q''|_{y=0}dx}{(T_h - T_c)L} \qquad (2.45)$$

Figure 2.4 shows that the average skin friction coefficient depends mainly on L/H, and is roughly inversely proportional to L/H. The insensitivity of C_f to changes in Re_L, ϕ and H/D is particularly evident when $L/H > 2$, although minor even when $L/H < 2$. The effect of increasing H/D is to increase C_f, while the effect of increasing ϕ is to decrease C_f.

The results for heat transfer are more complicated. Figure 2.5a shows the effect of the porosity and the Reynolds number: the total heat transfer rate increases with both ϕ and Re_L. More interesting is the alternative shown in Fig. 2.5b, where $Nu_L/Nu_{L,b}$ is the ratio between the actual Nu_L value (Fig. 2.5a) and the value calculated for the same Re_L in the limit where the wall surface is bare (no fibers, or $L/H \to \infty$). Interesting is how the ratio $Nu_L/Nu_{L,b}$ compares with 1. Below a critical porosity (roughly 0.94 in Fig. 2.5b), the fibers provide an insulation effect, and $Nu_L < Nu_{L,b}$. Above the critical porosity, the permeability of the porous layer is sufficiently high, and the cold flow entering from above is sufficiently strong, that the fibers act as fins surrounded by cold fluid. In this regime the fibers augment the heat transfer from the wall, $Nu_L > Nu_{L,b}$. These two extremes, i.e. the fact that hair-like fibers provide insulation in some cases and augmentation in others, confirm the main point of the theoretical work or surfaces covered with hair (Bejan, 1990).

The effect of Re_L on the heat transfer is illustrated in greater detail in Fig. 2.6. The heat transfer through the wall with fibers increases almost proportionally with Re_L. This increase is steeper than when the wall is bare, because $Nu_L/Nu_{L,b}$ also increases with L. In conclusion, the faster flow (higher Re_L) removes more heat because of two effects: (1) cold fluid comes closer to the wall, as in the case of a bare wall, and (2) the fibers provide a finning effect.

Figure 2.7 shows the end result of a search (Chapter 1) for a way to correlate the numerical heat transfer results for surfaces covered with stiff fibers. The parameter chosen on the abscissa is mL/H, where m is the fraction of the total external flow ($U_\infty L$) that penetrates into the fiber layer,
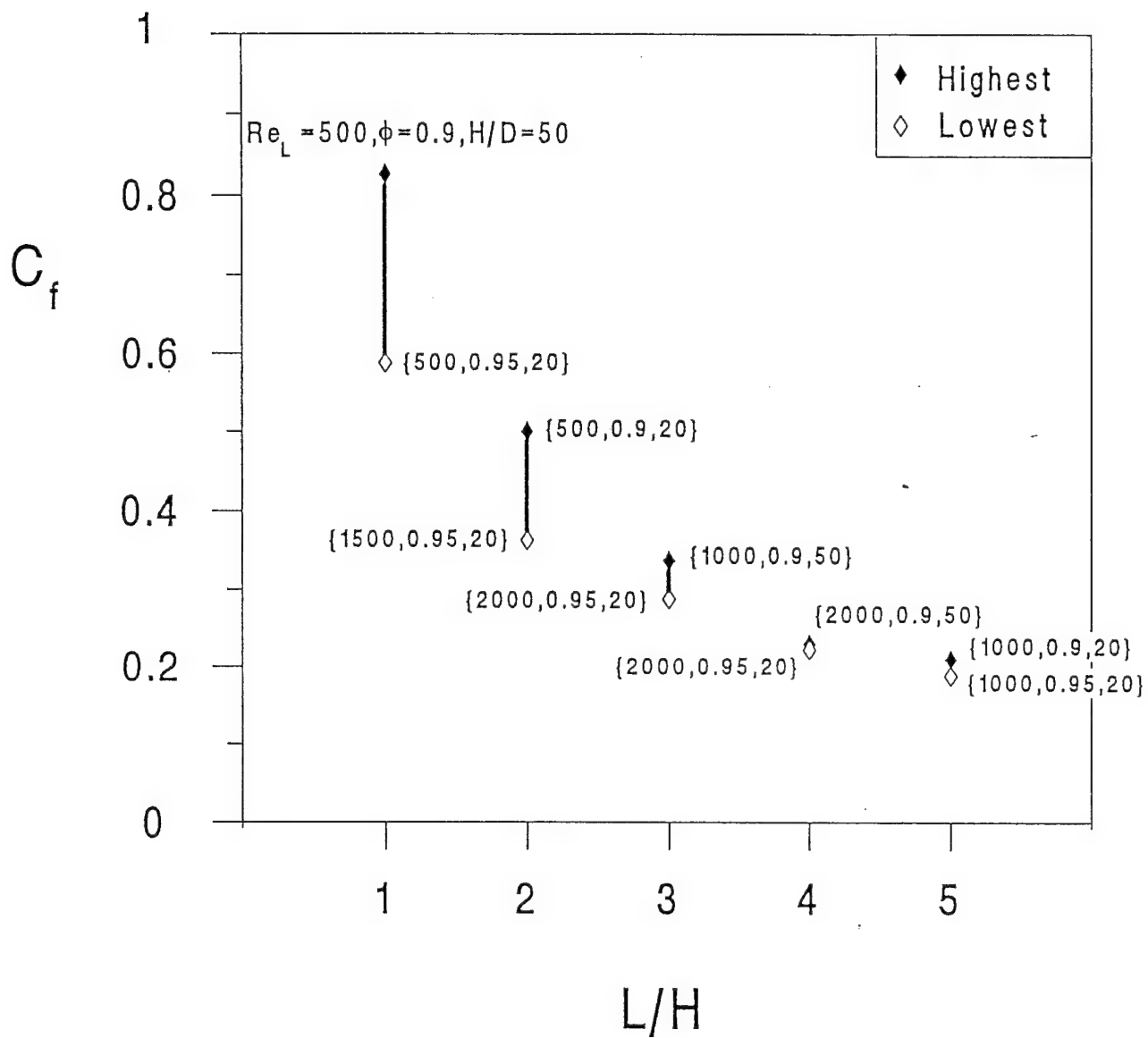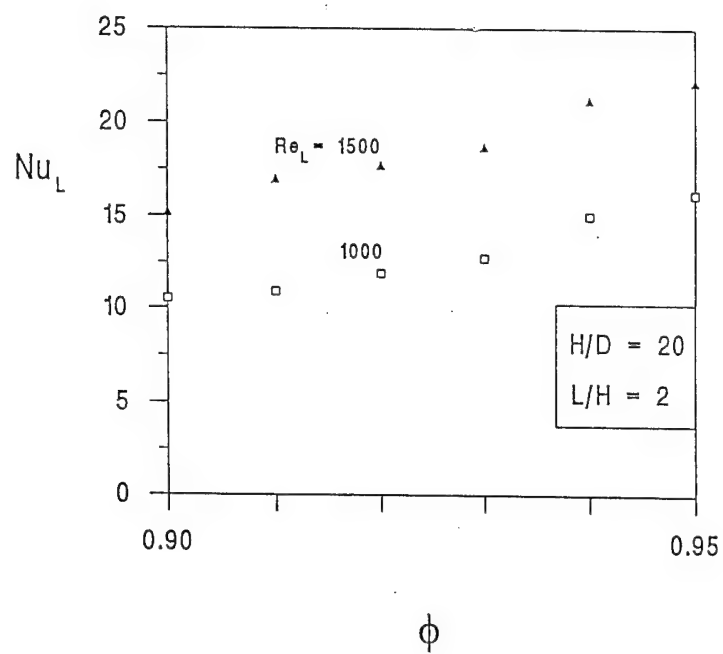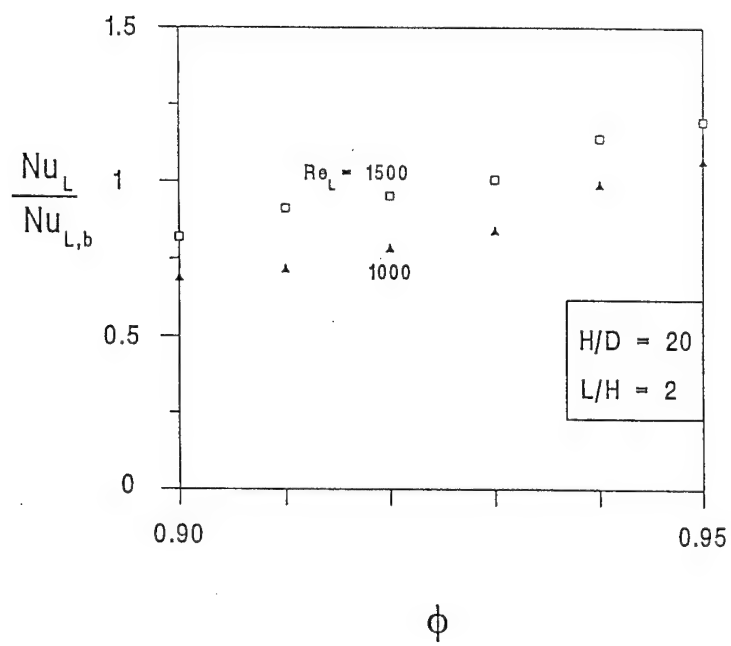
Figure 2.4: The average skin friction coefficient for a wall with inflexible fibers.

(a)

(b)

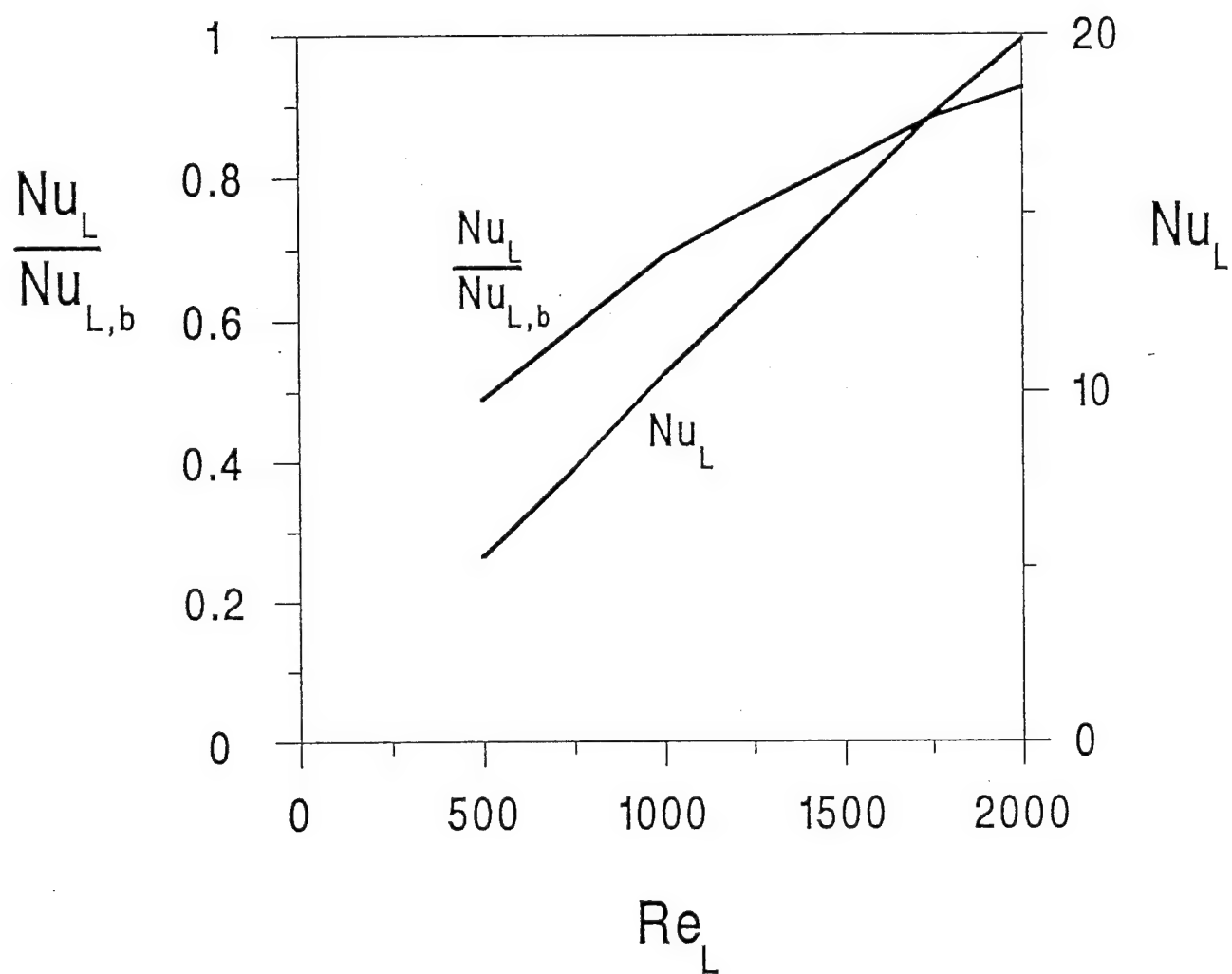Figure 2.5: The average Nusselt number for a wall with inflexible fibers.

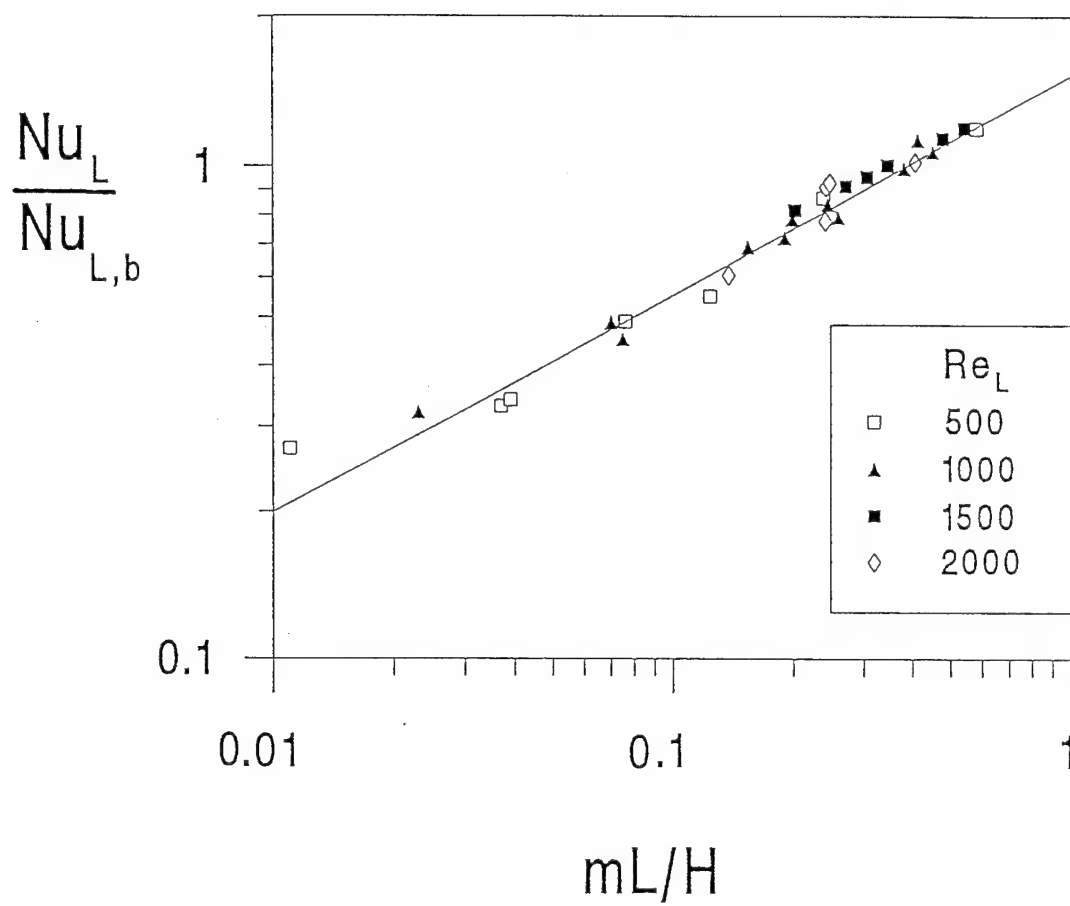Figure 2.6: The effect of Reynolds number on heat transfer when the fibers do not bend.

Figure 2.7: Heat transfer correlation for a wall with inflexible fibers.

$$m = \frac{1}{U_\infty L} \int_0^L (-v)_{y=H} dx \tag{2.46}$$

The numerical $Nu_L/Nu_{L,b}$ data correlated in Fig. 2.7 cover the range $0.9 \leq \phi \leq 0.95, 500 \leq Re_L \leq 2000, H/D = 20$ and 50, and $L/H = 1$ through 5. The line

$$\frac{Nu_L}{Nu_{L,b}} = 1.58(m\frac{L}{H})^{0.4} - 0.051 \tag{2.47}$$

approximates the data with a mean error of 5.2 %.

It is to be expected that equation (2.47) will fail in the limit $mL/H \to 0$, where there is no flow through the fiber layer. In that limit the Nusselt number reaches a minimum value, $Nu_{L,min}$, which can be evaluated based on the parallel thermal resistance model (trapped fluid in parallel with fibers)

$$Nu_{L,min} = \left(Nu_{L,b}^{-1} + \left\{ \frac{L}{H} \left[\phi + \frac{k_s}{k}(1 - \phi) \right] \right\}^{-1} \right)^{-1} \tag{2.48}$$

If the Nu_L value calculated with equation (2.47) is less than $Nu_{L,min}$, then the correct value is $Nu_{L,min}$ given by equation (2.48). To illustrate this observation, consider the left most datum (a square) plotted in Fig. 2.7: that point corresponds to $\phi = 0.9, L/H = 2, H/D = 50$ and $Re_L = 500$, for which equation (2.48) yields $Nu_{L,min} = 2.8$. This means that $Nu_{L,min}/Nu_{L,b} = 0.26$, which is greater than the ratio found using equation (2.47), $Nu_L/Nu_{L,b} = 0.2$. The actual Nu_L value determined numerically is 2.9, which is very close to $Nu_{L,min} = 2.8$ given by equation (2.48).

To calculate the heat transfer based on the correlation (2.47) or Fig. 2.7, we need a way to predict mL/H. Figure 2.8 shows the correlation

$$\frac{mL/H}{C_{f,b}} = 0.0476Re_p^{1.7} - 0.029 \tag{2.49}$$

where $C_{f,b}$ is the average skin friction coefficient for the bare wall. The mean error between the data and equation (2.49) is 18.6 %. The abscissa parameter is the Reynolds number used in convection through porous media (Nield and Bejan, 1992), namely $Re_p = U_\infty K_\perp^{1/2}/\nu$.

The skin friction and heat transfer correlations for the bare-wall limit are presented in Fig. 2.9. The dashed line shows an empirical correlation developed by Sparrow et $al.$ (1979) from experiments measuring mass transfer from a plate two and a half times as wide as it was long, which was subjected to incident flow at angles from 25° to 90°. The form of their correlation is $Nu_L = 0.939Re_{L^*}^{-1/2}Pr^{1/3}Re_L$, where $L^* = 4A/C$, A is the plate area, and C is the plate circumference. Sparrow et $al.$ found that by using Re_{L^*} in the correlation they eliminated almost entirely the geometric dependence of Nu_L. Their experiments showed,
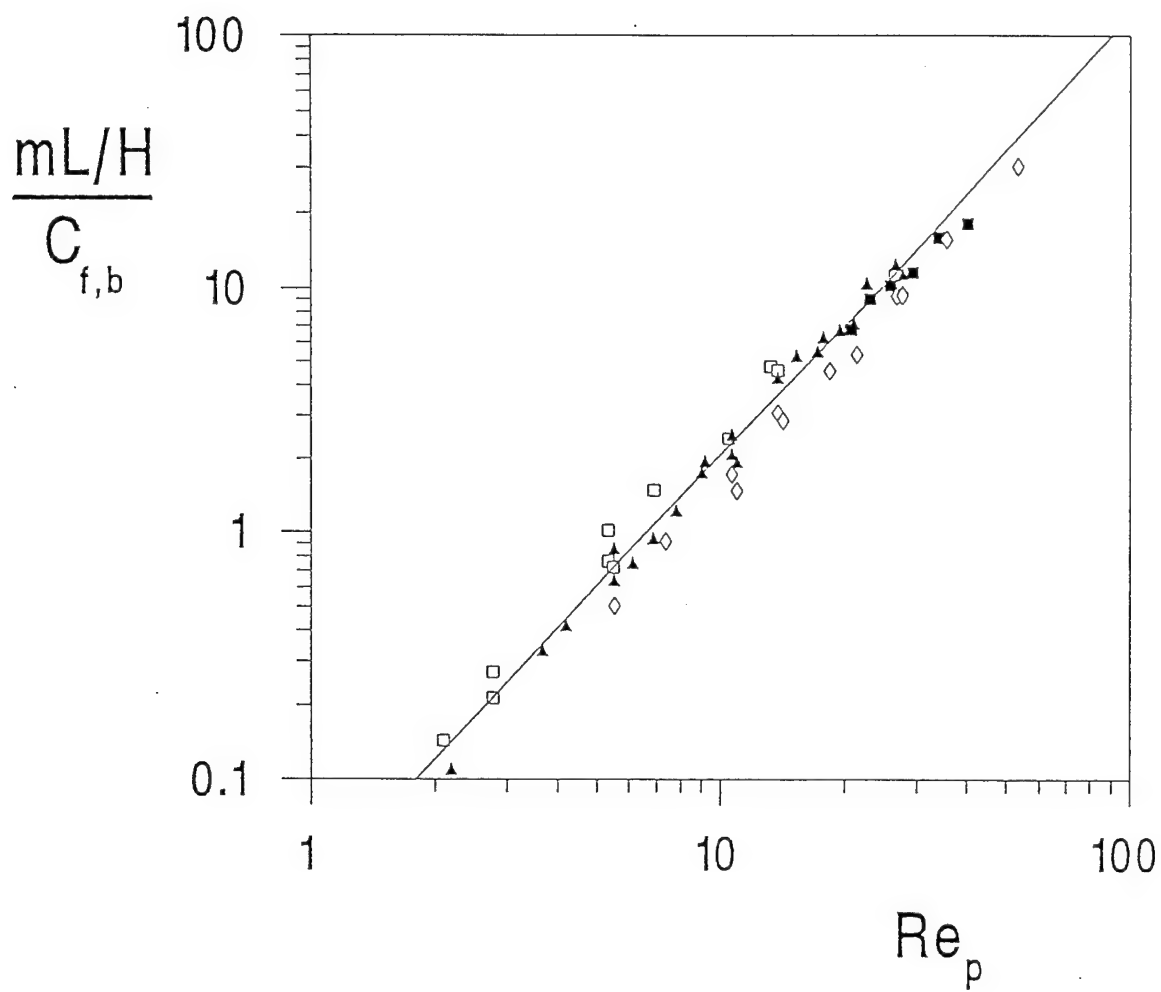
Figure 2.8: Correlation for the fraction of the external flow that penetrates into the layer with fibers.

however, a small geometric dependence for the leading factor (0.939 above): this factor increases as the width of the plate increases. In their experiments, the Nu_L increase from a narrow plate (width/length = 0.4) to the wider plate was 9%. This change is consistent with the 12% difference between the dashed line and our Nu_L results (the solid line), because our results are for a plate of infinite width.

2.5 The Effect of Fiber Bending

We examined the effect of fiber bending by varying the stiffness parameter S. We considered three cases: $(Re_L = 500, L/H = 1, \phi = 0.9, H/D = 20)$, $(Re_L = 1000, L/H = 2, \phi = 0.9, H/D = 20)$ and $(Re_L = 2000, L/H = 4, \phi = 0.95, H/D = 20)$. The selected ϕ and H/D values are such that a significant fraction of the external flow penetrates into the fiber layer. The characteristics of the fiber cover on the $L/H = 1$ and $L/H = 2$ surfaces are identical, so they correspond physically to two surfaces with identical covering, but with different lengths, L and $L/2$, respectively. The maximum fiber bending calculated was $\beta = 20°$ for $L/H = 1, \beta = 40°$ for $L/H = 2$ and $\beta = 38°$ for $L/H = 4$.

Figures 2.10 - 2.12 illustrate the effect of fiber bending on the skin friction, heat transfer and flow penetration into the fibers. In the geometries considered the transition from "no S effect" to "substantial S effect" is fairly abrupt. More flexible fibers (lower S values) mean smaller C_f, Nu_L and m values.

Figure 2.10 illustrates the effect of fiber bending on skin friction. For the three surfaces the effect is significant. The decrease in C_f from the case of no bending to the maximum bending calculated is about 15% in all cases (specifically, 14%, 18% and 15% for $L/H = 1, 2$ and 4, respectively). Figure 2.11 shows, however, that the effect of fiber bending on Nu_L is small. The total decrease in Nu_L is 5%, 8% and 6% for the three surfaces. From the result for surfaces with inflexible fibers one might conclude that the magnitude of the penetrating flow m must also be insensitive to the fiber bending. Examination of Fig. 2.12, however, shows that this is not the case.

The effect of fiber bending on the flow penetrating the fiber layer, m, is shown in Fig. 2.12. The effect is quite large: 45% for $L/H = 2$ and 43% for $L/H = 4$. According to the relationship developed for predicting Nu_L based on m for a surface covered with inflexible fibers, equation (2.47), a 45% decrease in m should result in about a 21% decrease in Nu_L; but as was shown in Fig. 2.11, Nu_L actually decreases by only 5 - 8% while m decreases by 43 - 45%. This suggests that while less flow enters the fiber layer as a whole, the flow must be penetrating to the warm surface at a rate roughly independent of fiber bending.

A possible explanation for this is that when the fibers bend they orient themselves in a direction closer to perpendicular to the downward coming flow: this decreases the layer's
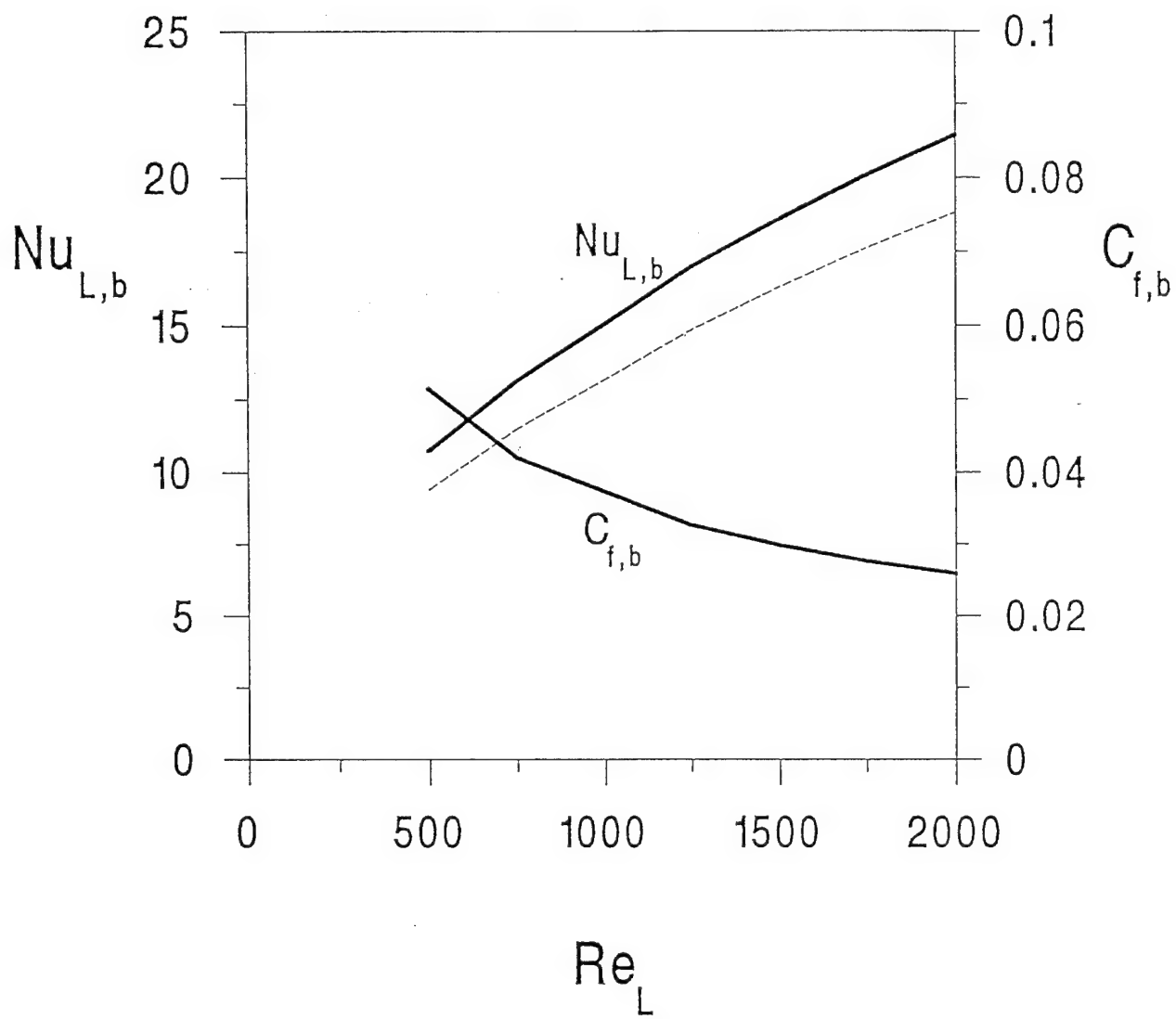
47

Figure 2.9: Skin friction and heat transfer results for the bare wall limit (Pr = 0.72)
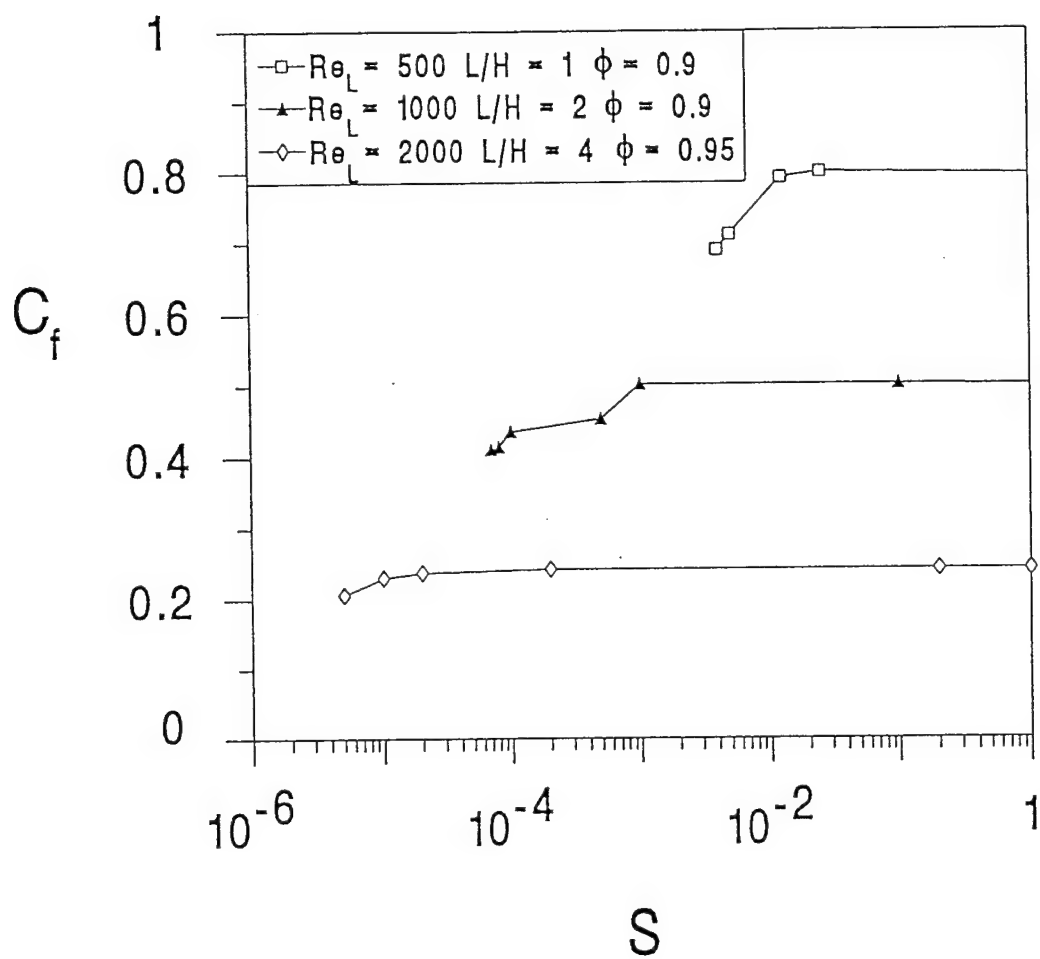
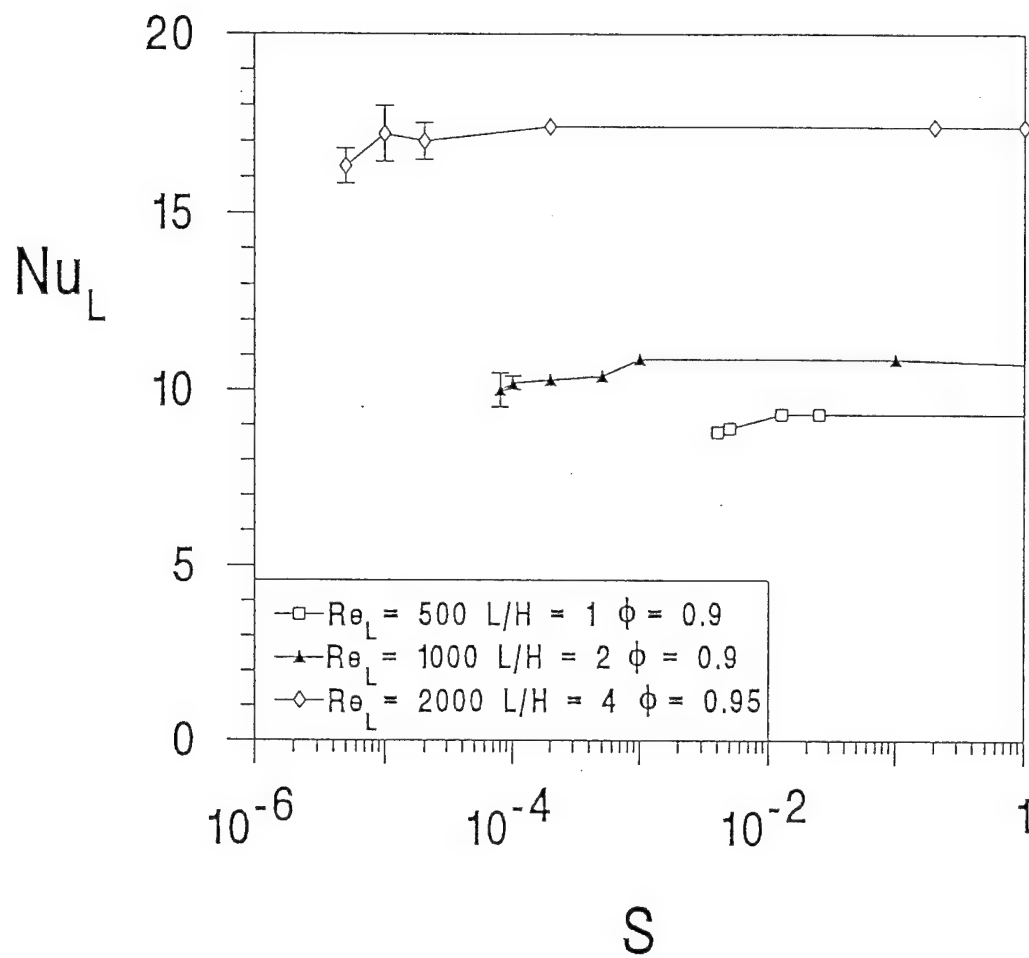Figure 2.10: The effect of fiber stiffness on skin friction.

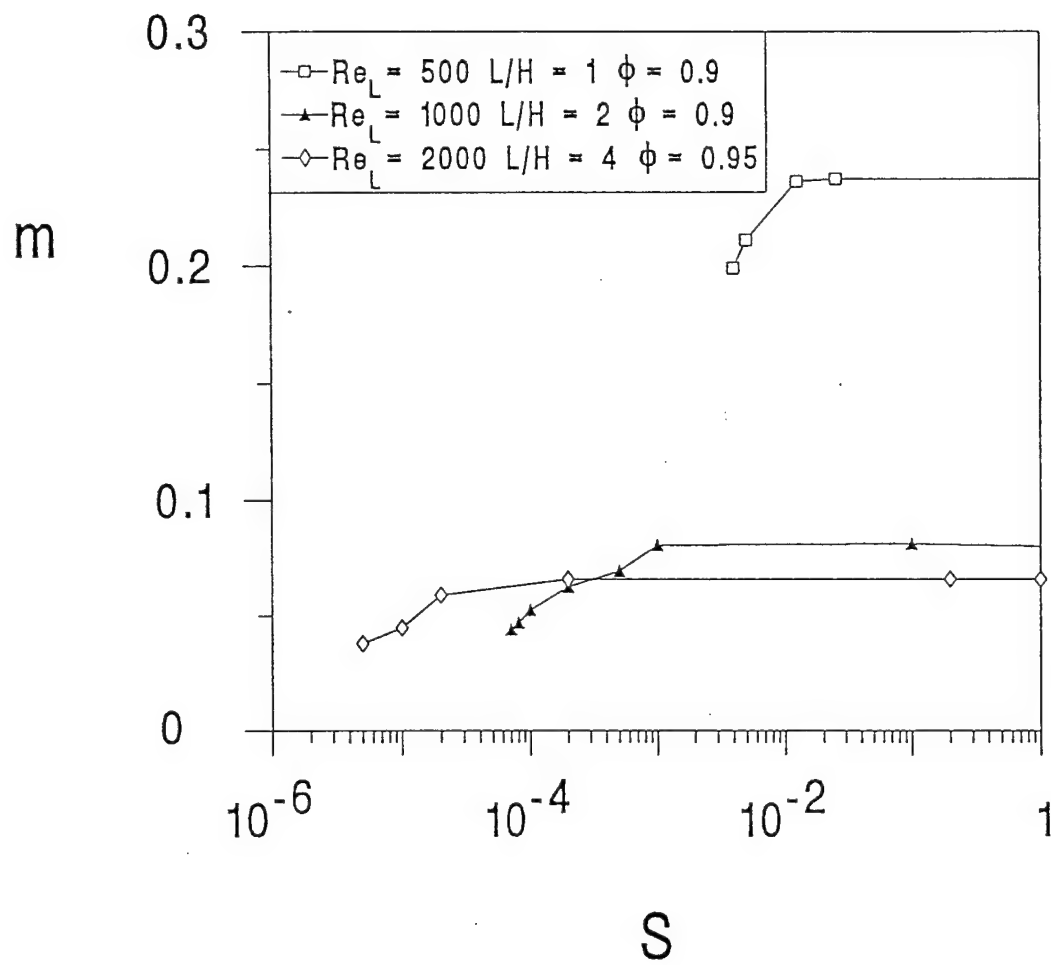Figure 2.11: The effect of fiber stiffness on heat transfer.

Figure 2.12: The effect of fiber stiffness on flow penetration into the fiber layer.

permeability. At the same time, however, the spreading of the fibers causes an increase in porosity, which causes an increase in permeability. The spreading tends to occur near $x = 0$, and the maximum fiber bending occurs near $x = L$ (Fig. 2.13). This results in a deflection of the $x = L$ fluid away from the fiber layer, but allows fluid into the small-x region at the same (or even a higher) rate as the rate that occurs when the fibers do not bend.

Figure 2.13 illustrates the progressive bending of the fibers as the stiffness S decreases for the $L/H = 4$ surface. Each "fiber" line drawn on the fiber surface represents many actual fibers. The number represented per line depends upon ϕ, and H/D. It is clear from the figure that the region near $x = L$ is much less permeable to downward flow because of the fiber angle and decreased porosity. The minimum porosity for the $L/H = 4$ surface was $\phi \cong 0.935$, which corresponds to $\phi = 0.95$ when the fibers are straight.

To summarize, Figs. 2.10 - 2.13 show that the bending of the fibers begins to have an effect when the stiffness number S drops below a certain, critical level. We recorded this effect quantitatively, by first defining the critical stiffness number S_c as the S value where m drops to 90% of its value for inflexible fibers,

$$m(S = S_c) = 0.9\, m(S \rightarrow \infty) \tag{2.50}$$

We then determined numerically the $m(S)$ dependence for a series of 12 cases, of which only three are illustrated in Fig. 2.10. The resulting S_c values can be correlated as

$$S_c = \frac{C}{1 - \phi} \left(\frac{H}{L}\right)^5 \left(\frac{D}{H}\right)^2 \tag{2.51}$$

for which the C coefficient is reported in Fig. 2.14. The analytical form of equation (2.51) was derived based on equation (2.38) and the hypothesis that the critical stiffness S_c corresponds to a critical fiber angle γ_c. Figure 2.14 shows that in the parametric domain considered the C coefficient does not depend systematically on Re_L. The most we can say is that C is a number of order 0.4. That a correlation of type (2.51) should hold is suggested also by Fig. 2.4, which implies that the dimensionless pressure field is largely insensitive to Re_L.

Setting $C = 0.4$ in equation (2.51) allows us to predict S_c to within a factor of 2 for all the cases tested. We expect this relationship to hold for high Re_L flows where the viscous effects on the pressure field will continue to be negligible. Equation (2.51) should break down at sufficiently low Re_L values, because in that direction viscous effects become important. Low Re_L flows, however, are also characterized by little or no penetrating flow in the fiber layer, which makes these flows of considerably less interest.

$S = 2 \times 10^{-5}$

0   0.5   1

$S = 1 \times 10^{-5}$

0   0.5   1

$S = 5 \times 10^{-6}$

0   0.5   1
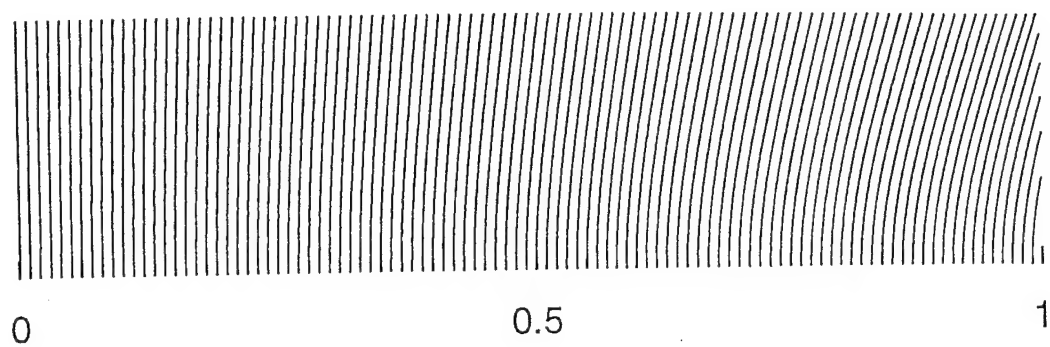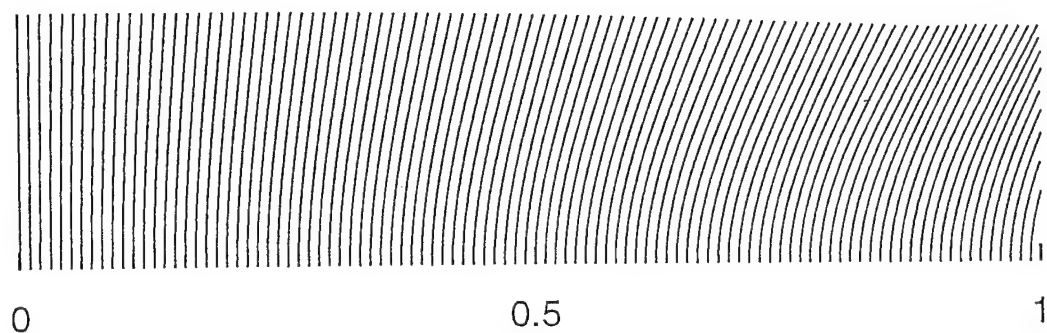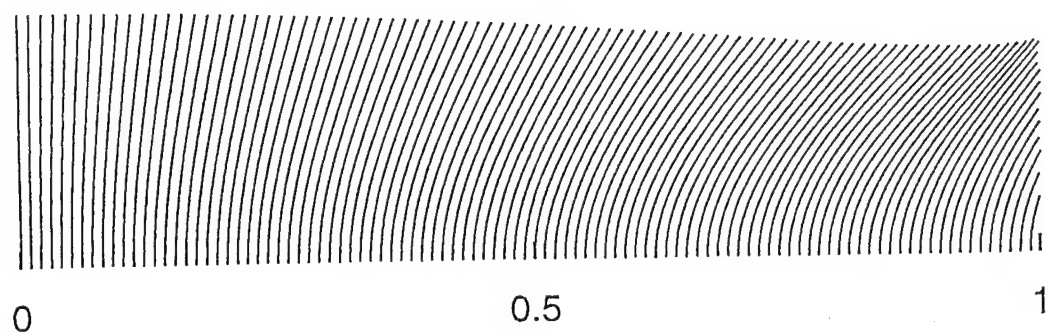
Figure 2.13: The effect of stiffness on the fiber shape ($Re_L = 200, L/H = 4, \phi = 0.95, H/D = 20$).
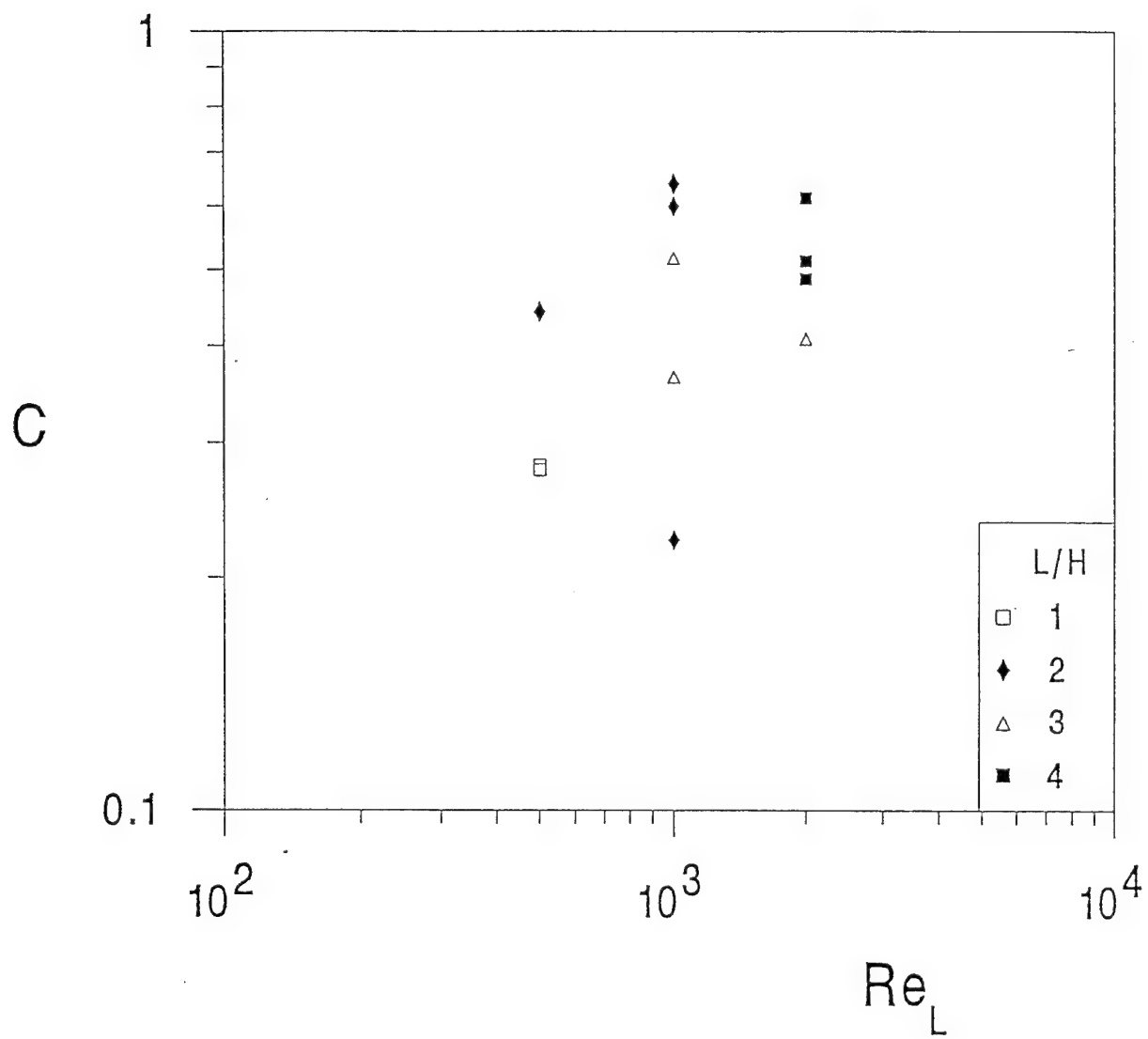
Figure 2.14: The C coefficient for the critical stiffness correlation (2.51) ($\phi = 0.9 - 0.95, H/D = 20$ and 50).

2.6 Concluding Remarks

In this chapter we investigated the interaction between a solid surface and an external flow when the solid is covered with a layer of fibers. The objective was to document the way in which the fiber layer properties affect the overall heat transfer and friction characteristics of the surface.

In the first part of the study we considered the limit in which the fibers are inflexible. The results presented in Figs. 2.4-2.9 and in the text show that the fiber layer can alter significantly the wall characteristics, especially the overall heat transfer. A peculiar effect is due to the porosity: at porosities lower than a critical value, the fiber cover acts as an insulation, while at higher porosities the fibers augment the heat transfer (Fig. 2.5b). We showed that the effect of the fiber cover can be correlated in terms of the flow fraction that penetrates into the fibers (Fig. 2.7, 2.8).

In the second part we examined the bending of the fibers, as they interact with the flow that penetrates the fiber layer. The fiber bending is governed by the nondimensional stiffness number S. We found that when S decreases below a critical value S_c, there is a sudden drop in wall friction, heat transfer and penetrating flow fraction (Fig.2.10-2.12). The least sensitive to changes in S is the overall heat transfer rate (Fig. 2.11). We showed that the critical stiffness number S_c values determined numerically can be correlated cf. equation (2.51) and Fig. 2.14.

2.7 Notation

A aspect ratio, L/H

A_{ht} heat transfer area in one r.e.v., m^2

$\tilde{A}_{ht}$ dimensionless heat transfer area

A_s sum of fiber cross-section in one r.e.v., m^2

Bi Biot number

c_p specific heat at constant pressure, $kJ/(kgK)$

C coefficient for the critical stiffness number correlation (2.51), Fig. 2.14

C_f average skin friction coefficient

d_j deflection of fiber segment, m

D fiber diameter, m

E modulus of elasticity, N/m^2

F_x, F_y force components, N

h heat transfer coefficient

H height of unbent fibers, m

I area moment of inertia, m^4

k fluid thermal conductivity, $W/(m \cdot K)$

k_s fiber thermal conductivity, $W/(m \cdot K)$

$K_x, K_y, K_{xy}, K_\perp, K_\parallel$ permeabilities, m^2

L half-length of plane wall, m

m penetrating flow fraction

M_j moment, $N \cdot m$

n number of fibers in one r.e.v.

N number of fiber segments

Nu_L average Nusselt number

p pressure, N/m^2

p_s sum of wetted perimeters in one r.e.v., m

$\tilde{p}_s$ dimensionless sum of perimeters in one r.e.v.

P dimensionless pressure

$\tilde{P}_j$ position vector, m

Pr Prandtl number, ν/α

q'' heat flux, W/m^2

r.e.v.   representative elementary volume

Re_L Reynolds number

Re_p porous medium Reynolds number

s curvilinear coordinate, m

S stiffness number

S_c critical stiffness number

T temperature, K

u, v velocity components, m/s

U, V dimensionless velocity components

U_∞ approach velocity, m/s

V_{rev} volume of one r.e.v., m^3

W width of plane wall, m

x, y coordinates, m

X, Y dimensionless coordinates

α fluid thermal diffusivity, m^2/s

β fiber angle, Fig. 2.2

γ_c critical fiber angle

γ_j local fiber angle at node j

θ dimensionless temperature

μ viscosity, $kg/(s \cdot m)$

ν kinematic viscosity, m^2/s

ρ fluid density, kg/m^3

$\tilde{\sigma}$ stress vector, N/m^2

ϕ porosity

$(\quad)_b$ bare wall

$(\quad)_c$ cold fluid

$(\quad)_h$ hot wall

$(\quad)_f$ fluid in the fiber layer

$(\quad)_s$ solid matrix (fibers)

$(\quad)''$ per unit area

$(\tilde{\ })$ dimensionless

Chapter 3

THE OPTIMAL SPACING BETWEEN HORIZONTAL CYLINDERS IN A FIXED VOLUME COOLED BY NATURAL CONVECTION

3.1 Introduction

In this chapter we report the results of a theoretical, numerical and experimental study of how to determine the optimal spacing for horizontal cylinders in an array with natural convection heat transfer. The volume occupied by the array is fixed. The number of cylinders in the array, or the spacing between cylinders of fixed diameter, can vary. The optimal spacing reported in this paper corresponds to the maximum overall heat transfer (or thermal conductance) between the array and the surrounding fluid.

The optimal spacing question is both important and timely. It is important because of its obvious implications in the design of heat exchangers, surfaces with horizontal pin fins, and, generally, the cooling by natural convection of a space of fixed size (e.g. electronic package). The question is timely in view of the large volume of research that has been devoted to arrays of horizontal cylinders with natural convection on the outside. This body of work was reviewed on several occasions (e.g. Guceri and Farouk, 1985; Sadeghipour and Asheghi, 1994) and will not be reviewed here. Most of this work delt primarily with the detailed interaction between adjacent cylinders, not with the overall performance (thermal conductance) of the entire array.

The existence of an optimal spacing for maximum heat transfer was noted by Sparrow and Vemuri (1985) in an experimental study of an array with a large number of horizontal pin fins. The heat transfer was by combined natural convection and radiation. The maximum exhibited by the overall heat transfer rate was very shallow and corresponded to using an array with approximately 35 pin fins.

Related aspects of this subject were considered by Tokura et al. (1983) and Sadeghipour and Asheghi (1994). Tokura et al. reported an optimal spacing for a vertical column of horizontal cylinders confined by two vertical plates. It is not at all clear, however, that their result corresponds to maximum heat transfer. Their recommendation to use 6 cylinders in the array appears to be a trade-off between transferring more heat and using more hardware (cylinders).

Sadeghipour and Asheghi reconsidered the optimal spacing question in Tokura et al.'s configuration. Their experimental results suggest a shallow maximum in the variation of the overall heat transfer rate with the cylinder-to-cylinder spacing. The final correlation for this relationship, however, does not indicate a maximum with respect to spacing: the overall

heat transfer increases monotonically with the spacing, and reaches its highest values (or plateau) when the S/D ratio exceeds approximately 15.

The absence of a correlation for the reported optimal spacings, and the inability of predicting optimal spacings in new configurations defined the objectives of the present study. To begin with, we focused exclusively on heat transfer by natural convection (without radiation). Our objective was not only to determine the optimal spacings for various situations, but also to correlate our results in a compact dimensionless relation valid for any array with laminar natural convection.

To achieve this objective we conducted the study in three phases. In the first, we developed a pure theory to prove the existence of the optimal spacing, and to reveal the proper dimensionless groups and analytical form of the optimal-spacing correlation. In the second phase, we simulated the natural convection flow and temperature fields, and varied the spacing (or number of cylinders) of the array to generate optimal-spacing data to be correlated based on the theory. Finally, in the third phase of the study we experimented with several arrays of cylinders that occupied the same volume. The purpose of these experiments was to determine the optimal spacing through direct heat transfer and temperature measurements, and to test in this way the accuracy of the numerical phase of the study.

3.2 Theoretical Results

We begin with a theoretical argument to demonstrate that there exists an optimal cylinder-to-cylinder spacing for maximum heat transfer, and to identify the proper dimensionless groups needed to correlate the optimal spacing results determined more accurately (numerically and experimentally).

Consider the bundle of horizontal cylinders shown in Fig. 3.1. The overall dimensions of the bundle (H, L, W) and the cylinder diameter (D) are fixed. Natural convection heat transfer (q) occurs between the cylinder surfaces (T_w) and the surrounding fluid reservoir (T_∞). In the following analysis we address the question of how to select the number of cylinders in the bundle, or the cylinder-to-cylinder spacing (S), such that the *overall* thermal conductance between the bundle and the ambient, $q/(T_w - T_\infty)$ is maximized. For the sake of conciseness we assume that the cylinders are staggered, and that their centers form equilateral triangles. Other array types can be treated similarly. The problem is similar to that of determining the optimal number of plates in a stack cooled by natural or forced convection.

When the spacing S and the Rayleigh number are sufficiently large each horizontal cylinder is coated by a distinct boundary layer, and the surrounding fluid is at the temperature T_∞. We are assuming that $(H, W) >> (D + S)$, and that $Ra_D >> 1$, where $Ra_D = g\beta D^3(T_w - T_\infty)/(\alpha\nu)$. The heat transfer from one cylinder is

59

$$q_1 \cong \frac{k}{D} Nu_D \pi DL(T_w - T_\infty) \tag{3.1}$$

where the overall Nusselt number is (cf. Morgan, 1975, $10^4 < Ra_D < 10^7$)

$$Nu_D = 0.48 Ra_D^{1/4} \tag{3.2}$$

The total number of cylinders in the bank of cross-sectional area $H \times W$ is

$$n = \frac{HW}{(S+D)^2 \cos 30^\circ} \tag{3.3}$$

therefore the total heat transfer from the bank is $q = nq_1$ or

$$q_{largeS} \cong 1.74 \frac{HLW}{(S+D)^2} k(T_w - T_\infty) Ra_D^{1/4} \tag{3.4}$$

This result shows that when the spacing is large, the overall thermal conductance $q/(T_w - T_\infty)$ decreases as S increases.

Consider now the opposite extreme when the cylinders almost touch, and the flow is almost cut off. In this limit the temperature of the coolant that exits slowly through the upper plane of the bundle ($L \times W$) is essentially the same as the cylinder temperature T_w. The heat transfer from the bundle to the coolant is equal to the enthalpy gained by the coolant, $q = \dot{m}c_p(T_w - T_\infty)$, where $\dot{m}$ is the mass flow rate through the $L \times W$ plane.

To obtain an order-of-magnitude estimate for the flow rate, we note that $\dot{m}$ is composed of several streams [total number $= W/(S+D)$], each with a cross-sectional area $S \times L$ in the plane of one horizontal row of cylinder axes. The thickness of the channel traveled upward by each stream varies between a minimum value (S) at the row level, and a maximum value at a certain level between two rows. The volume-averaged thickness of one channel is

$$\overline{S} = S + D - 0.907 \frac{D^2}{S+D} \tag{3.5}$$

however, we may adjust this estimate by using 1 in place of the factor 0.907 to account for the fact that the channel closes (i.e. the flow must stop) when the cylinders touch ($S = 0$):

$$\overline{S} = S \frac{S+2D}{S+D} \tag{3.6}$$

When $\overline{S}$ is sufficiently small, the flow rate through each channel of cross sectional area $\overline{S}L$ and flow length H is proportional to the pressure difference that drives the flow. The pressure difference is $\Delta P = \rho g H \beta(T_w - T_\infty)$, or the difference between the hydrostatic pressures under two H-tall columns of coolant, one filled with T_∞ fluid, and the other with
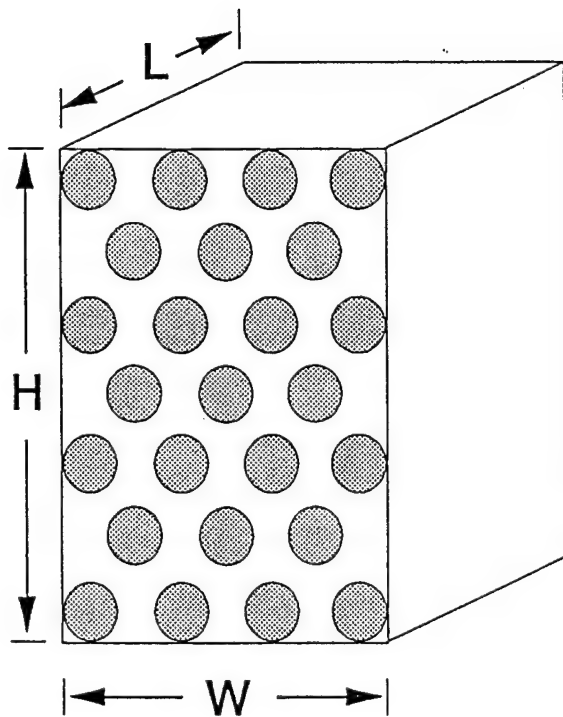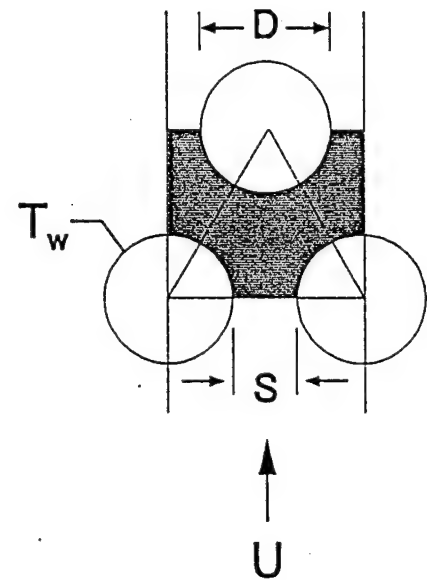
Figure 3.1: Bundle of horizontal cylinders immersed in a quiescent fluid (a), and detail of one of the channels traveled by the fluid (b).

T_w fluid. The mean velocity of the channel flow, U, can be approximated using the Hagen-Poiseuille solution for flow between two parallel plates (spacing $\overline{S}$, flow length H),

$$U = \frac{\overline{S}^2 \Delta P}{12 \mu H} \tag{3.7}$$

The total flow rate through the bundle, $\dot{m}(\rho U \overline{S} L) \cdot W/(S+D)$, leads to the total heat transfer rate $\dot{m} c_p (T_w - T_\infty)$, which can be summarized as

$$q_{smallS} \cong \frac{\overline{S}^3 L W}{12 D^3 (S+D)} k(T_w - T_\infty) Ra_D \tag{3.8}$$

The key feature of this estimate is that when S is small and decreases, the thermal conductance $q/(T_w - T_\infty)$ decreases as S^3.

Figure 3.2 summarizes the trends uncovered so far. The actual thermal conductance would be represented by the solid curve sketched in the figure. The peak of this curve corresponds to a spacing (S_{opt}) that can be approximated by intersecting the two asymptotes, $q_{largeS} = q_{smallS}$. The result of eliminating q between equations (3.4) and (3.8) is

$$\frac{S_{opt}}{D} \cdot \frac{2 + S_{opt}/D}{(1 + S_{opt}/D)^{2/3}} \cong 2.75 \left(\frac{H}{D}\right)^{1/3} Ra_D^{-1/4} \tag{3.9}$$

This relation is plotted in Fig. 3.3, which shows that S_{opt}/D is almost proportional to the group $(H/D)^{1/3} Ra_D^{-1/4}$. In other words, a simpler alternative to the order of magnitude estimate obtained in equation (3.9) is

$$\frac{S_{opt}}{D} \sim \left(\frac{H}{D}\right)^{1/3} Ra_D^{-1/4} \tag{3.10}$$

or

$$\frac{S_{opt}}{H} \sim \left(\frac{H}{D}\right)^{1/12} Ra_H^{-1/4} \tag{3.11}$$

where $Ra_H = g\beta H^3 (T_w - T_\infty)/(\alpha \nu)$. Equation (3.11) shows that the optimal spacing is approximately proportional to $H^{1/3} D^{-1/12}$, which means that it is almost insensitive to changes in the cylinder diameter.

3.3 Numerical Results

In this section and the next we report numerical and experimental results for the optimal cylinder-to-cylinder spacing. The objective of these empirical phases of our study was to test and improve the accuracy of the correlation determined theoretically, equations (3.9)-(3.11).

The natural convection and heat transfer in an array of horizontal cylinders was simulated numerically by focusing on a vertical channel formed between two adjacent rows of cylinders, Fig. 3.4. It was assumed that the flow is laminar, such that there is no exchange of fluid and energy between adjacent channels. The regime is laminar when $Ra_H \leq 10^9 Pr$ (Bejan and Lage, 1990), because H is the relevant vertical dimension of the channel with boundary layer flow.

The mass, momentum and energy equations were simplified in accordance with the assumptions of two-dimensional steady state, nearly constant properties, and Boussinesq approximation in the buoyancy term of the momentum equation for the vertical (y) direction:

$$\frac{\partial u}{\partial x} + \frac{\partial v}{\partial y} = 0 \tag{3.12}$$

$$u\frac{\partial u}{\partial x} + v\frac{\partial u}{\partial y} = -\frac{1}{\rho}\frac{\partial p}{\partial x} + \nu\nabla^2 u \tag{3.13}$$

$$u\frac{\partial v}{\partial x} + v\frac{\partial v}{\partial y} = -\frac{1}{\rho}\frac{\partial p}{\partial y} + \nu\nabla^2 v + g\beta(T - T_\infty) \tag{3.14}$$

$$u\frac{\partial T}{\partial x} + v\frac{\partial T}{\partial y} = \alpha\nabla^2 T \tag{3.15}$$

where $\nabla^2 = \partial^2/\partial x^2 + \partial^2/\partial y^2$. The horizontal and vertical velocity components are u and v. The origin of the Cartesian frame (x, y) is located in the bottom left corner of the computational domain. The computational domain contains the actual channel of height H/D (fixed), plus an inlet (bottom) section and an outlet (top) section. Accuracy tests showed that when the inlet length is 2.5 D and the outlet length $3D$, the calculated heat transfer from the channel is insensitive (with changes less than 1 percent) to further doubling of the inlet and outlet lengths.

The flow boundary conditions were: zero normal stress and vertical flow $(u = 0)$ at the inlet to the computational domain $(x = 0)$; free slip and no penetration at the fluid interfaces (planes of symmetry) between two consecutive cylinders; no slip and no penetration at the cylinder surfaces, and free slip and no penetration on the vertical boundaries of the inlet section. It is important to note that the forcing of free slip and no penetration conditions on the vertical boundaries of the outlet section would induce an artificial acceleration of the fluid (updraft, chimney effect) through the cylinder-to-cylinder channel. To avoid this effect, a zero stress inlet condition was specified along one of the sides of the outlet section, specifically, on the side opposite the topmost cylinder (Fig. 3.4).

The temperature boundary conditions were $T = T_w$ on the cylinder surfaces, and $T = T_\infty$ at the bottom end of the computational domain. The remaining portions of the boundary of the computational domain were modelled as adiabatic.
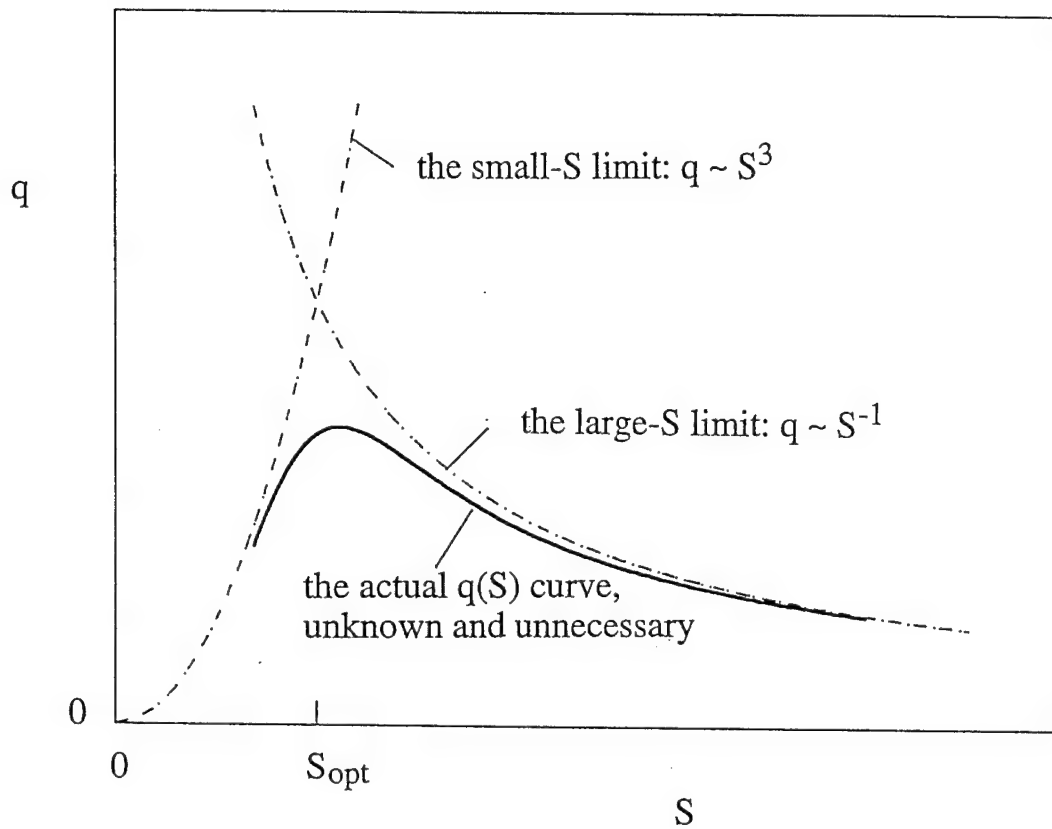
Figure 3.2: The optimal cylinder-to-cylinder spacing for maximum thermal conductance, as the intersection of the large-S and small-S asymptotes.
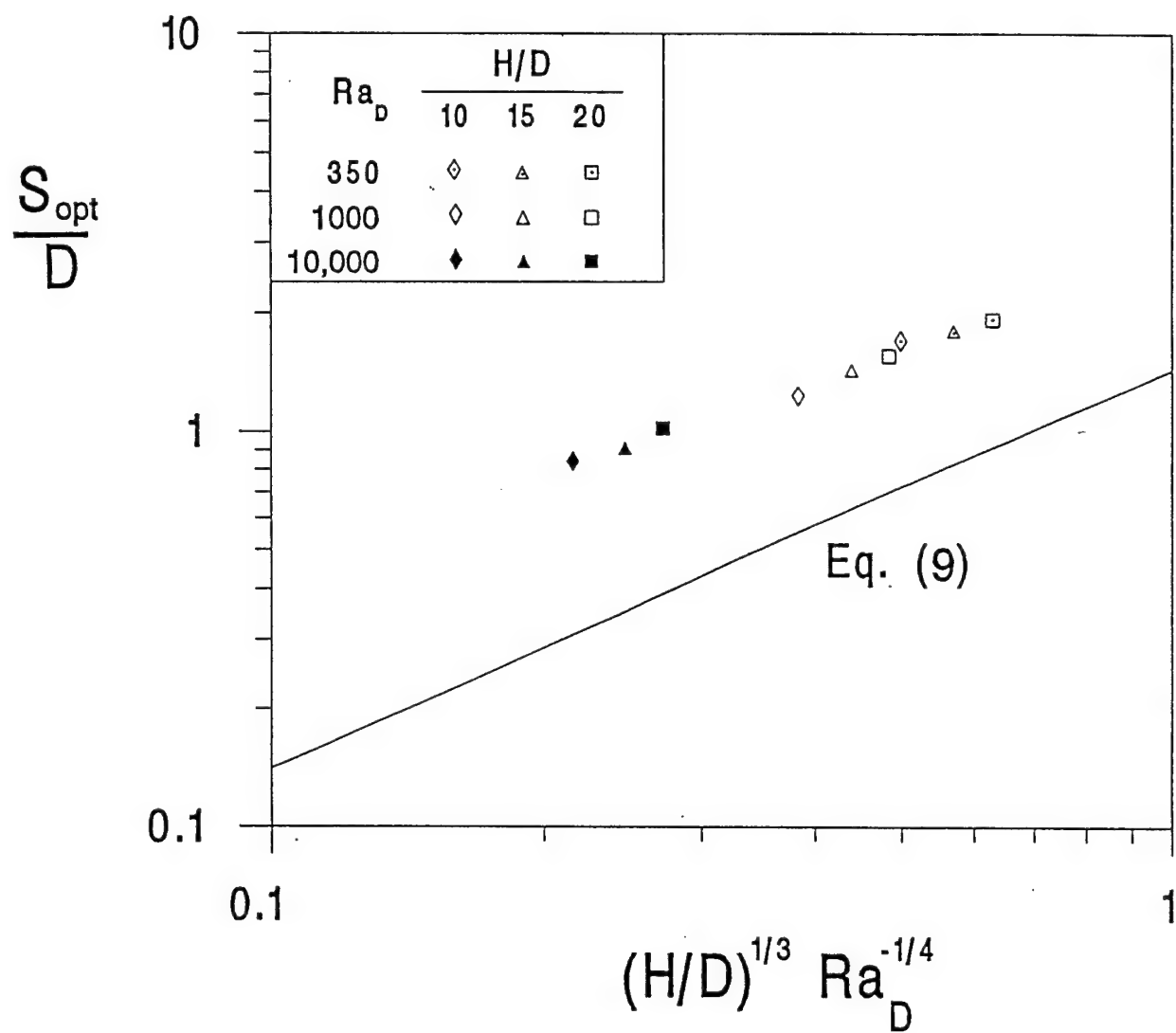
Figure 3.3: The optimal cylinder-to-cylinder spacing as a function of bundle height and cylinder diameter (Pr=0.72).

Equations (3.12) - (3.15) were nondimenionalized by defining the dimensionless variables

$$(X, Y) = \frac{(x, y)}{D}, \qquad (U, V) = \frac{(u, v)}{(\alpha/D)(Ra_D Pr)^{1/2}} \tag{3.16}$$

$$\theta = \frac{T - T_\infty}{T_w - T_\infty}, \qquad P = \frac{pD^2}{\mu\alpha(Ra_D Pr)^{1/2}} \tag{3.17}$$

Numerical solutions were generated for $Pr = 0.72$. The system of equations was solved on a Cray-YMP using a finite element package (FIDAP, 1991). Grid refinement tests showed that 40 nodes per D in x and y were necessary for $Ra_D = 10^4$, such that the further doubling of the number of nodes caused a change of less than 2 percent in the heat flux from each cylinder.

The accuracy of the numerical method was checked further by placing a single half cylinder in the computational domain, and calculating the overall Nusselt number Nu_D. The values obtained were $Nu_D = 3.20$ for $Ra_D = 10^3$, and $Nu_D = 5.10$ for $Ra_D = 10^4$. These values agree within 6 percent with the large body of empirical results compiled by Morgan (1975), and fall between the error bars indicated by Morgan for the correlation listed in equation (3.2).

For each array geometry $(H/D, S/D)$ the solutions were generated by solving for $Ra_D = 10^3$ first, and then using that solution as initial condition for the next higher Ra_D. The computational time depended strongly on the array geometry and Rayleigh number.

Figure 3.4 shows a sample of the flow and temperature fields calculated for $H/D = 10$ and $Ra_D = 10^4$. The streamline and isotherm patterns are arranged in a way that illustrates our search for the optimal cylinder-to-cylinder spacing of an array in a *fixed volume*. We fixed the height of the array (H), and decreased the spacing (S): we did this discretely (in steps), each time by adding one more to the number of cylinders (n_c) in the channel of height H.

During this sequence we monitored the total heat transfer from all the half-cylinders, to see how it responds to changes in S. A sample is shown in Fig. 3.5, where the ordinate parameter represents the dimensionless heat transfer volumetric density,

$$\tilde{q} = \frac{q}{HLW} \frac{D^2}{k(T_w - T_\infty)} \tag{3.18}$$

where q is the total heat transfer from an array of fixed volume HLW. Figure 3.5 shows that there is an optimal spacing for maximum heat transfer. The S_{opt}/D values were determined by fitting the highest three $\tilde{q}$ points with a parabola, and solving $\partial\tilde{q}/\partial(S/D) = 0$. The best practical spacing, of course, corresponds to the number of cylinders n (an integer) that maximizes the total heat transfer rate from the given space.
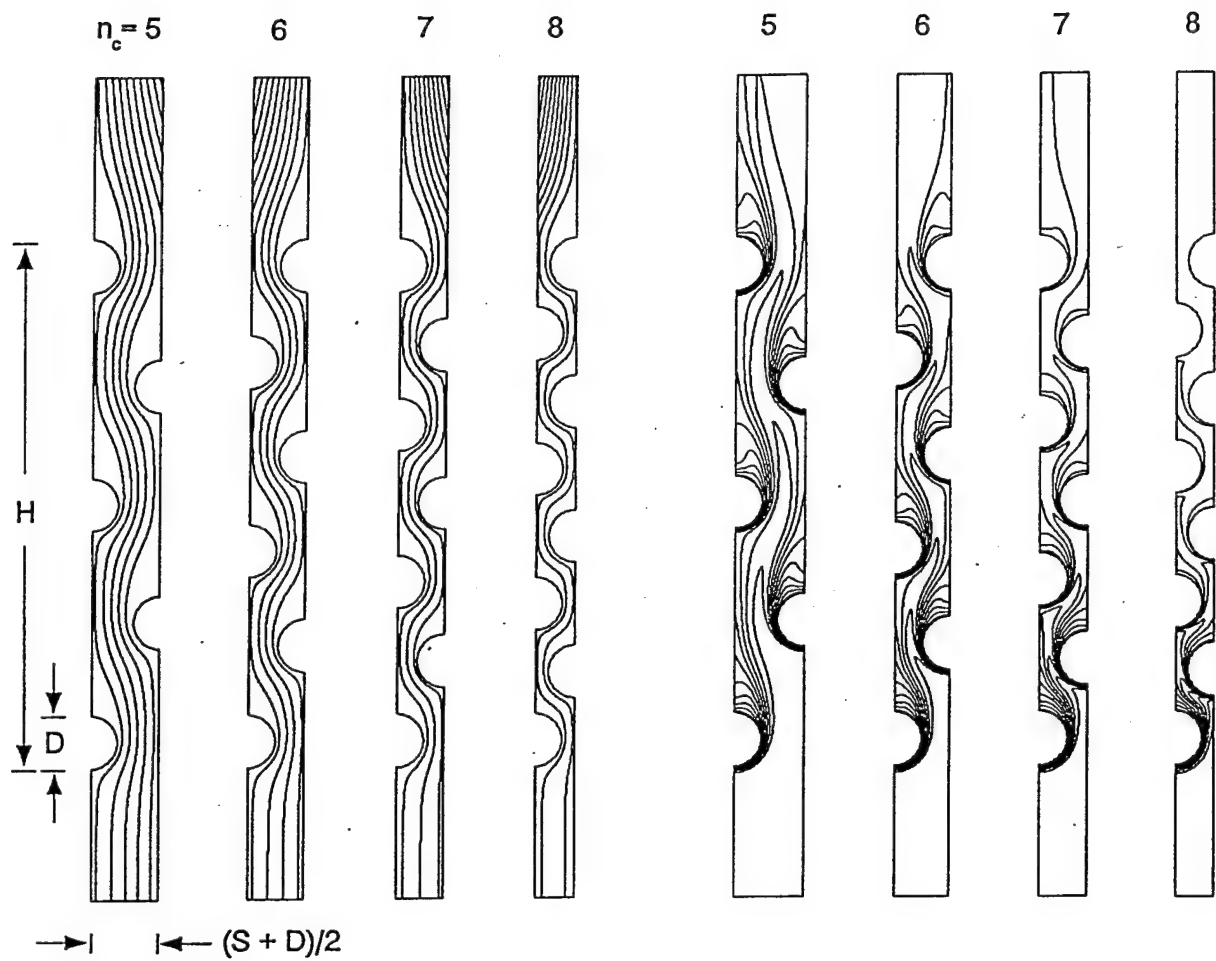
Figure 3.4: The computational domain, and the effect of cylinder-to-cylinder spacing on the flow and temperature fields ($H/D = 10, Ra_D = 10^4, Pr = 0.72$). The streamliners are on the left, and isotherms on the right.

The resulting S_{opt}/D data are reported in Fig. 3.3. They are correlated very nicely in the manner anticipated in section 3.2, namely by using the group $(H/D)^{1/3}Ra_D^{-1/4}$ on the abscissa. The optimal spacings, however, are consistently 2.5 times larger than the values calculated based on equation (3.9). The function of type (3.10) that fits the numerical data the best (within 1.7 percent mean error) is

$$\frac{S_{opt}}{D} = 2.72 \left(\frac{H}{D}\right)^{1/3} Ra_D^{-1/4} + 0.263 \tag{3.19}$$

where 0.263 is a small correction term.

The maximum heat transfer density that corresponds to the optimal spacing of Fig. 3.3 is reported in Fig. 3.6. The dimensionless group used on the abscissa of Fig. 3.6 is result of the theory: it is easy to show that when equation (3.19) is substituted without the 0.263 correction into equation (3.4) or equation (3.8), the group $\tilde{q}/Ra_D^{1/4}$ becomes a function of only the group $(H/D)^{1/3}Ra_D^{-1/4}$, which appeared also on the abscissa of Fig. 3.3. The numerical data, however, are correlated better if we plot $\tilde{q}$ instead of $\tilde{q}/Ra_D^{1/4}$ on the ordinate. The data shown in Fig. 3.6 are reproduced within 1.7 percent by the correlation

$$\tilde{q}_{max} = 0.448 \left[\left(\frac{H}{D}\right)^{1/3} Ra_D^{-1/4}\right]^{-1.6} \tag{3.20}$$

3.4 Experimental Results

Figure 3.7 shows the main features of the arrays used in the experimental phase of this study. The array volume was fixed: $H = 39.4$mm, $L = 142$mm and $W = 44.5$mm. Three arrays were constructed by varying from 5 to 3 the number of horizontal rows in the $H \times W$ cross-section. The number of cylinders of the three arrays were 23, 14 and 8, and the respective spacings S/D were 0.5, 1 and 2.

The longitudinal conduction and loss of heat through the cylinder ends were minimized by holding each cylinder between two vertical wooden walls. The array assembly was held inside a 2m-high enclosure with a horizontal cross-section of 0.4m × 0.4m. The bottom and top ends of the enclosure were open to room air. To reduce the effect of radiation, the internal and external surfaces of the enclosure were covered with aluminum foil. By using the method of calculation outlined in Morgan (1975) and Sadeghipour and Asheghi (1994), we estimated that in our experiments the radiation contribution to the overall heat transfer rate was less than 1.6 percent. The maximum temperature recorded on the array (T_{w1}, Fig. 3.7) was 47.2°C.

Each cylinder was a low density electrical heater consisting of a helically wound heating element (resistance 96 Ω) held in a ceramic insulator filled with conductive magnesium

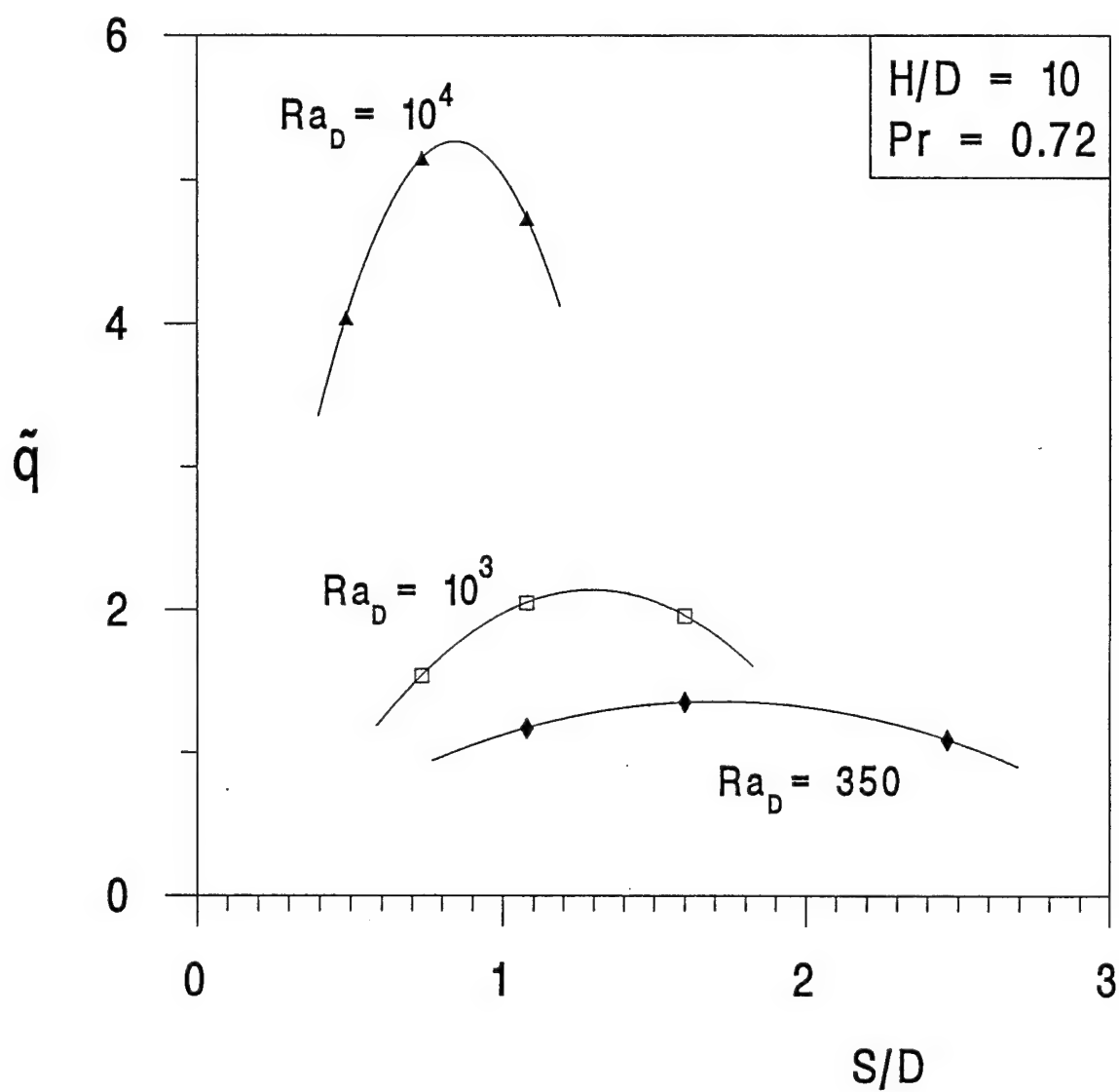Figure 3.5: The effect of the cylinder-to-cylinder spacing on the total heat transfer from the array ($H/D = 10, Pr = 0.72$)
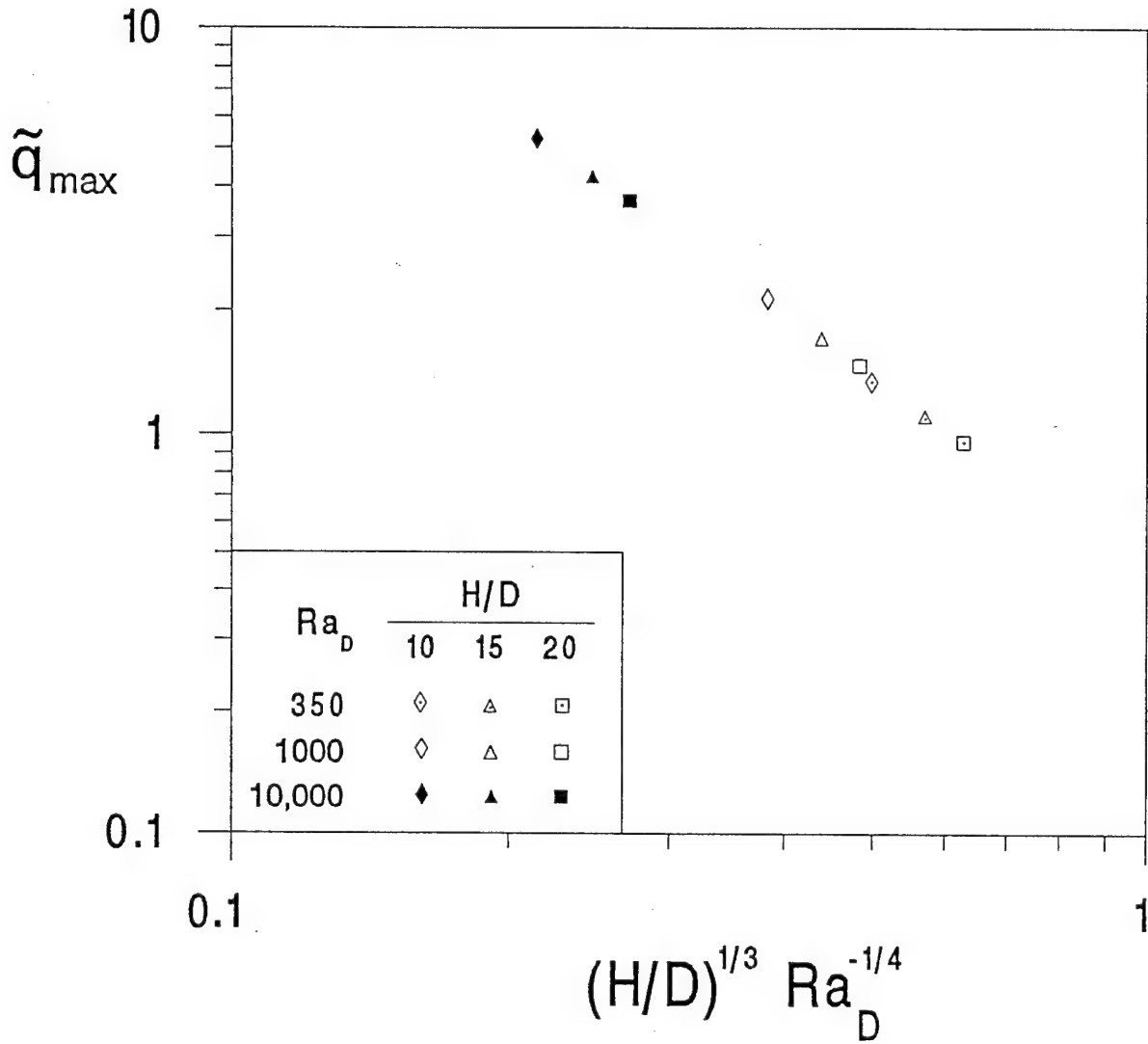
Figure 3.6: The maximum array heat transfer rate, or maximum heat transfer density, corresponding to the numerical optimal spacing data of Fig. 3.3.

$\frac{S}{D}$=0.5, n=23
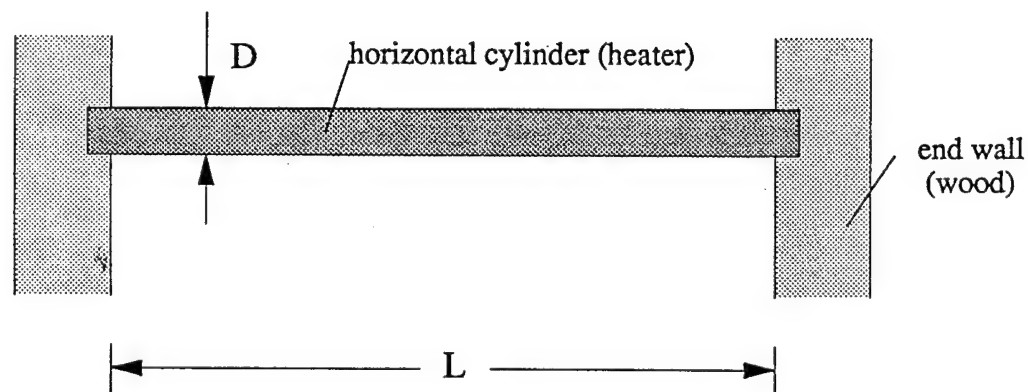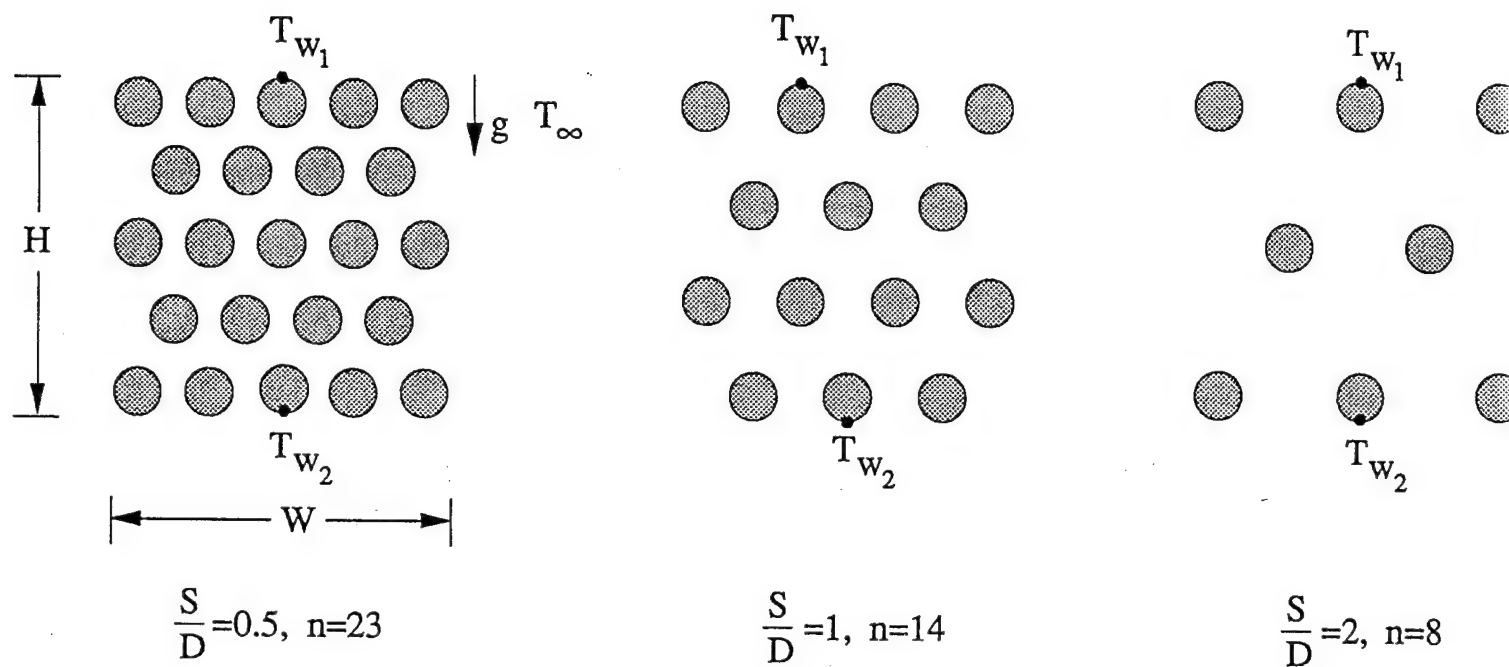
$\frac{S}{D}$=1, n=14

$\frac{S}{D}$=2, n=8

Figure 3.7: Details of the test section of the experimental apparatus.

oxide. The outer cover was polished 304 stainless steel, which provided adequate rigidity and resistance to oxidation. The heaters were connected in parallel, and powered by a variable autotransformer that produced a voltage between 0 and 140 V.

The temperatures T_{w1}, T_{w2} and T_∞ were measured in the vertical midplane of the array, i.e. half-way between the two wooden walls. Copper-constantan type T thermocouples were imbedded in 1mm hemispherical depressions machined into the stainless steel sheath of the heater. The thermocouple readings were referenced to a mixture of crushed ice and water. As the heat transfer rate per cylinder was distributed uniformly throughout the array, the maximum temperature was registered on the trailing row of cylinders (T_{w1}). The temperature was practically uniform (within 0.04°C) around the cylinder circumference: we measured this variation by running experiments with a single cylinder, and rotating the cylinder to change the position of the thermocouple on the circumference.

The overall thermal conductance $\tilde{q}$ was calculated after measuring the power dissipated in all the heaters (q), the maximum temperature (T_{w1}) and the room temperature at the bottom (inlet) of the enclosure (T_∞). The $\tilde{q}$ values were calculated using T_{w1} in place of T_w in equation (3.18). The properties of air were evaluated at the average temperature $(T_w + T_\infty)/2$, where $T_w = (T_{w1} + T_{w2})/2$.

The uncertainties associated with the $\tilde{q}$ and Ra_D values determined in this manner were 2.5 percent and, respectively, 4.9 percent. These were estimated based on the method of Kline and McClintock (1953), and the following inputs: 0.84 percent uncertainty in T_{w1}, T_{w2} and T_∞, resulting from the calibration of the thermocouples; 0.5 and 1 percent uncertainties in the measurement of voltage and, respectively, current; and 0.28 percent for c_p, 2 percent for μ, and 1 percent for k.

We started each run by setting the voltage and current for the resistance heaters. We then waited 3 to 4 hours while monitoring the changes in voltage, current, T_{w_1}, T_{w_2} and T_∞. We ended the run by taking final readings when the relative change in voltage, current and temperature readings was less than 0.2 percent, 0.2 percent and 0.06 percent (determined by repeating 10 hour-long runs at the same spacing and Ra_D), respectively. These relative changes are small when compared with the uncertainties in the respective measurements.

Figure 3.8 shows a summary of the heat transfer experiments. The figure shows also the curve fitting procedure used for determining S_{opt}/D, i.e. the same procedure as in the numerical part of the study (Fig. 3.5). The optimal spacings calculated in this manner are reported in Table 3.1. Again, the best practical array is the one with the largest overall thermal conductance, namely the case $n = 14$ (Figs. 3.7 and 3.8). The curve fitting of the $\tilde{q}$ data in Fig. 3.8 is used only as a test of the accurancy of the method employed in the numerical part of the study.
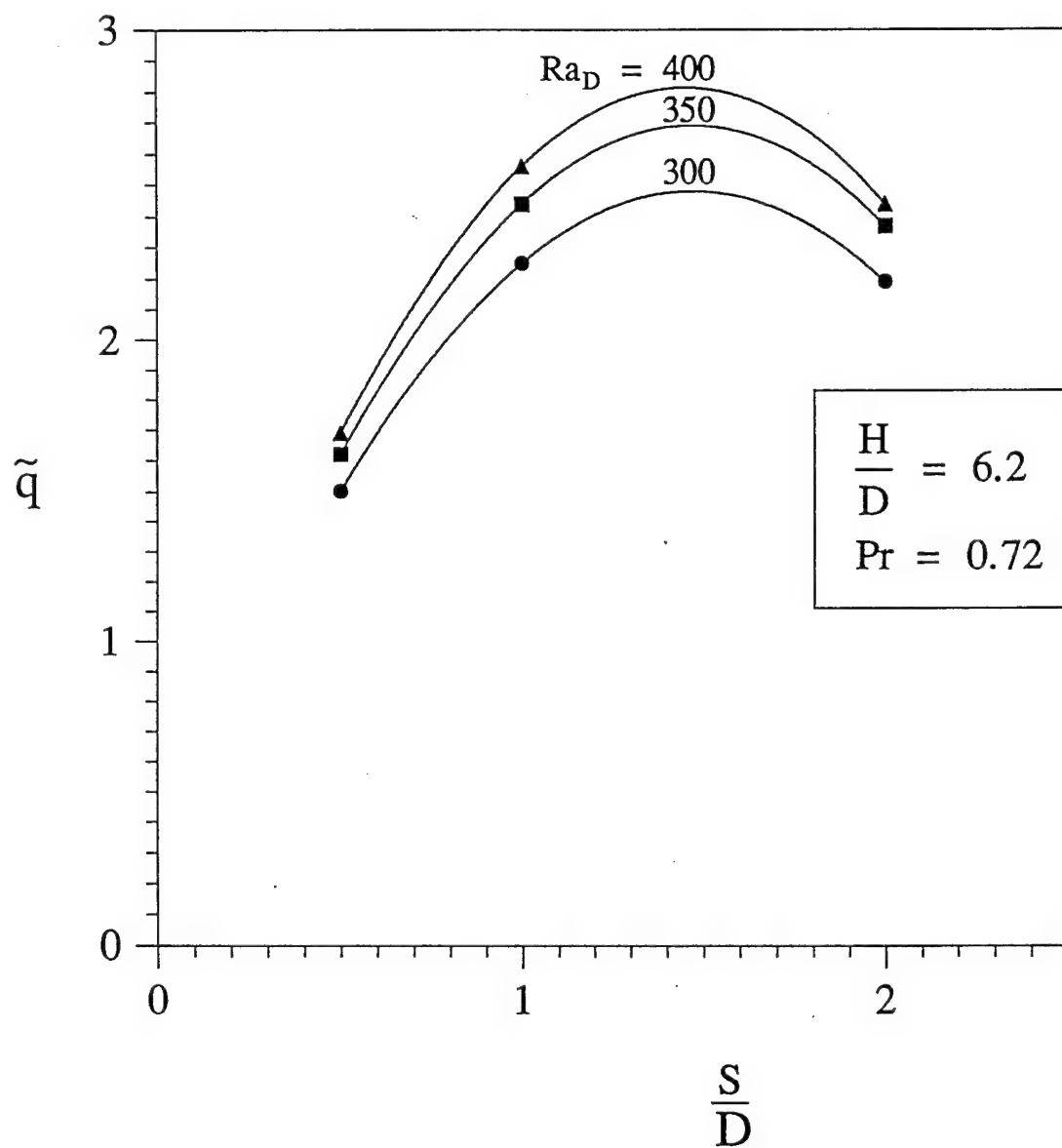
Figure 3.8: Experimental results for the total heat transfer rate from the array ($H/D = 6.2, Pr = 0.72$).

We used these experimental results to verify the accuracy of the numerical method described in the preceding section. The numerical results have been added to Table 3.1. We performed the numerical work for $H/D = 6.2$ and $Pr = 0.72$, which correspond to the experimental conditions. First, we modelled the cylinders as surfaces with uniform flux, and found that the maximum temperature occurs at the top of the topmost cylinder. The optimal spacing determined numerically agrees within 17 percent with the corresponding experimental result.

Table 3.1. Comparison between the optimal spacings determined experimentally, and the corresponding results obtained based on numerical simulations ($H/D = 6.2, Pr = 0.72$).

S_{opt}/D	Ra_D			
	200	300	350	400
Experiments		1.44	1.47	1.45
Numerical, uniform flux cylinders	1.78	1.68	1.62	1.61
Numerical, isothermal cylinders	1.54	1.48	1.46	1.44

We used this opportunity to see if the type of cylinder thermal boundary condition has an effect on the optimal spacing. We solved again the experimental configuration numerically, this time modelling the cylinders as isothermal, and found the results listed in the bottom line of Table 3.1. In place of T_w in equation (3.18) we used the average temperature of the topmost cylinder. It is clear that the optimal spacing is relatively insensitive to whether the array is uniform-flux or isothermal. This conclusion is important, because it means that the corelation (3.19) is general.

Additional evidence that the present results are correct is provided by the experimental study of Sparrow and Vemuri (1985). As pointed out in the Introduction, Sparrow and Vemuri maximized the total heat transfer rate from an isothermal vertical plate ($H = W = 7.62$ cm) with horizontal pin fins ($D = 0.635$ cm). Because the heat transfer maximum was rather flat, Sparrow and Vemuri concluded that the optimal spacing occurs when the total number of pins fins is between 30 and 40. The flat maximum was observed at Rayleigh numbers (based on H) in the range $4 \times 10^5 - 16 \times 10^5$.

Translated into the terminology employed in the present study, Sparrow and Vemuri's

conclusion means that the optimal spacing is in the range $1.04 < S_{opt}/D < 1.35$, when the Rayleigh number is in the range $230 < Ra_D < 920$. Their S_{opt}/D estimate agrees very well (within 10 percent) with the present experimental results (Table 3.1), especially if we recognize that (i) the H/D ratios were different (12 for Sparrow and Vemuri, versus 6.2 in the present study), (ii) in their experiments radiation was important, and (iii) their cylinders (pin fins) conducted heat longitudinally.

3.5 Conclusion

In this chapter we developed fundamental results for the selection of the spacing between horizontal cylinders in an array of fixed volume. The heat transfer is by laminar natural convection. The optimal spacing reported in equation (3.19) corresponds to the maximum thermal conductance between the entire array and the surrounding fluid.

More important fundamentally is the conclusion that the optimal spacing and maximum thermal conductance can be expressed in compact dimensionless relations. The relevant dimensionless groups have been identified, and each relation contains only two groups: S_{opt}/D and $(H/D)^{1/3}Ra_D^{-1/4}$ for optimal spacing, equation (3.19), and $\tilde{q}_{max}$ and $(H/D)^{1/3}Ra_D^{-1/4}$ for maximum thermal conductance, equation (3.20).

These developments were possible only because we began the study with a purely theoretical look at the problem of predicting the optimal spacing. It was only after the theory that we resorted to empiricism (numerical and experimental), which was necessary in order to improve the accuracy of the theoretical expressions found for S_{opt}/D and $\tilde{q}_{max}$. Furthermore, the dimensionless groups and analytical expressions revealed by the theory had the effect of minimizing the amount of numerical and experimental information needed for developing the recommended results, equations (3.19) and (3.20).

3.6 Notation

D diameter

g gravitational acceleration

H height of array, Fig. 3.1

k thermal conductivity

L cylinder length, Fig. 3.1

n number of cylinders in the volume HLW

n_c number of half-cylinder in the computational domain

75

Nu_D	single cylinder overall Nusselt number
p	pressure
P	dimensionless pressure
Pr	Prandtl number, ν/α
q_1	heat transfer from a single cylinder
q	heat transfer from the entire array
$\tilde{q}$	dimensionless heat transfer volumetric density
Ra_D	Rayleigh number, $g\beta D^3(T_w - T_\infty)/(\alpha\nu)$
Ra_H	Rayleigh number, $g\beta H^3(T_w - T_\infty)/(\alpha\nu)$
S	cylinder-to-cylinder spacing
$\overline{S}$	volume averaged spacing
T	temperature
T_w	cylinder surface temperature
T_∞	coolant inlet temperature
u, v	velocity components
U, V	dimensionless velocity components
U	mean velocity through $\overline{S}$-wide channel
W	frontal width of array, Fig. 3.1
x, y	horizontal and vertical coordinates
X, Y	dimensionless coordinates
α	thermal diffusivity
β	coefficient of volumetric thermal expansion
θ	dimensionless temperature
ρ	density

Chapter 4

THE OPTIMAL SPACING FOR CYLINDERS IN CROSS-FLOW FORCED CONVECTION

4.1 Introduction

In this chapter we focus on new fundamental aspect of the heat transfer performance of a bundle of parallel cylinders with cross-flow forced convection, namely, the maximization of the thermal contact between the bundle and the fluid, when the volume occupied by the bundle is fixed. In the experiments described by Jubran *et al.* (1993) we have seen empirical evidence that the total heat transfer rate is maximum when the cylinder-to-cylinder spacing S has a certain value. This finding is important because it has been overlooked for decades, while forced convection from cylinders in cross-flow grew into one of the most researched topics in heat transfer.

Jubran *et al.* (1993) did not offer any theoretical explanation or way of predicting the optimal spacing. The objectives in this chapter are two:

(a) To show that the optimal S/D ratio can be predicted based on a simple theory (Bejan and Sciubba, 1992), and that contrary to Jubran *et al.'s* conclusion, the S_{opt}/D ratio is not a constant.

(b) To also show that, if the theory (a) is known, all the empirical information necessary for predicting S_{opt}/D *accurately* is already available in the large volume of heat and fluid flow data published for cylinders in cross-flow.

4.2 The Method of Intersecting the Asymptotes

It is useful to begin with the simplest analysis that (i) proves the existence of an optimal spacing, and (ii) reveals the proper trends and dimensionless groups. Consider the bundle shown in Fig. 4.1. The cylinders occupy the fixed volume $H \times L \times W$, where H is aligned with the flow direction. The cylinder diameter D, the pressure drop across the bundle ΔP and the upstream temperature T_∞ are also fixed. The cylinder temperature is of order T_w; this order of magnitude characterizes all the cylinders in the bundle. We are interested in maximizing the total heat transfer q between the bundle and the surrounding fluid, by selecting the cylinder-to-cylinder spacing S, or the number of cylinders in the bundle.

Consider first the limit where the spacing S is sufficiently large that each cylinder acts as if it is alone in its own cross-flow of free-stream velocity U_∞. The total heat transfer rate experienced by the bundle is $q = nq_1$, where q_1 is the heat transfer associated with a single cylinder,
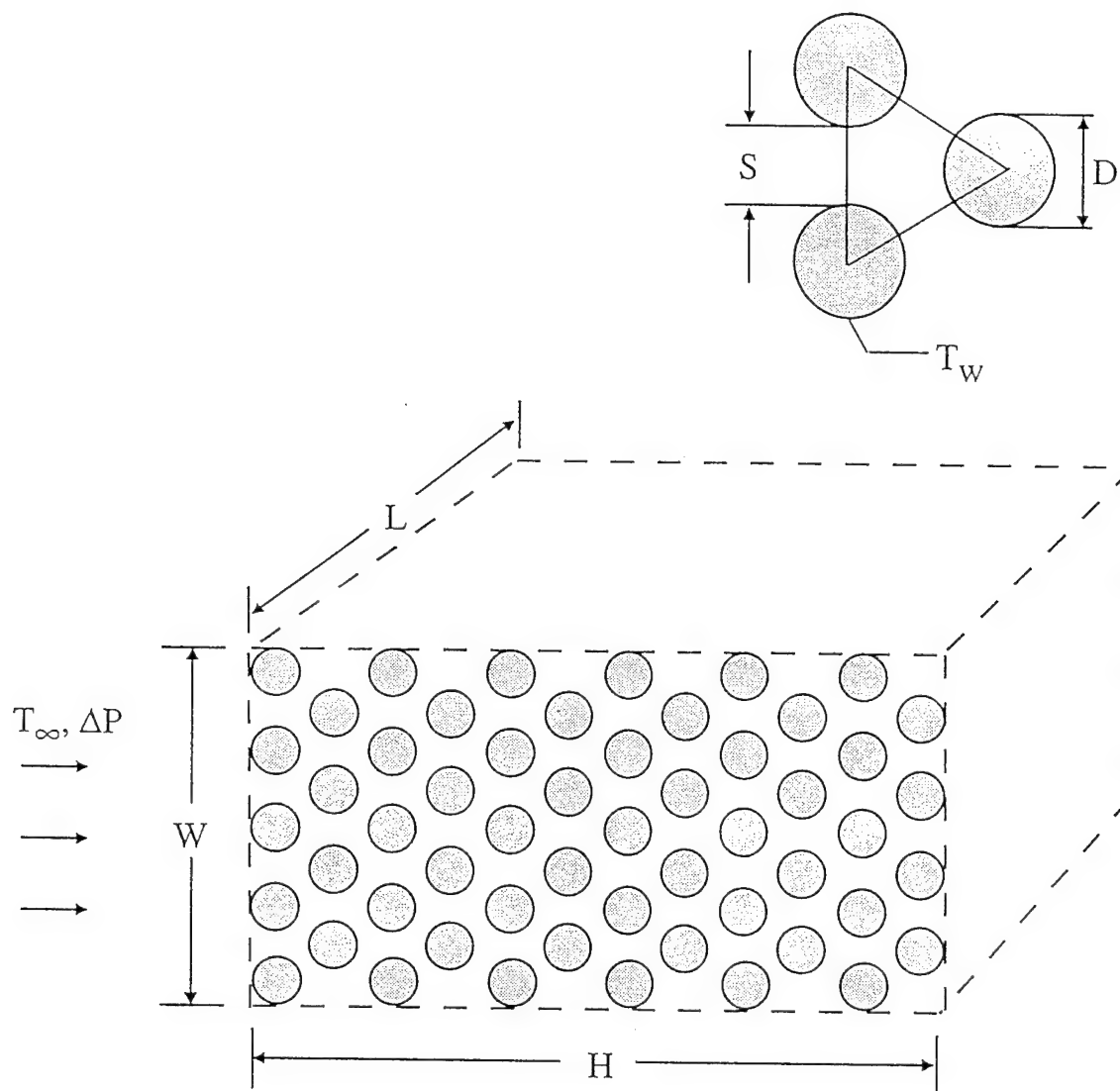
Figure 4.1: Fixed volume $H \times L \times W$ containing a bundle of parallel cylinders perpendicular to a free stream.

$$q_1 = \frac{k}{D} Nu \pi DL(T_w - T_\infty) \tag{4.1}$$

and n is the total number of cylinders,

$$n = \frac{HW}{(S+D)^2 \cos 30^\circ} \tag{4.2}$$

We are assuming that W is considerably greater than $(S+D)$. In the range $0.7 < Pr < 500$ and $40 < U_\infty D/\nu < 1000$, the average Nusselt number is given by the correlation (Zukauskas, 1987b)

$$Nu = 0.52 Pr^{0.37} Re^{1/2} \tag{4.3}$$

The free stream velocity U_∞ is not given. It is determined by the force balance on the entire bundle, $\Delta P \cdot WL = nF_1$, where F_1 is the drag force experienced by one cylinder, $F_1 = C_D DL(\rho U_\infty^2/2)$. The drag coefficient varies from 2 to 1 in the Re range 40 - 1000, therefore in this order of magnitude analysis it is sufficient to use $C_D \sim 1.5$. The force balance yields U_∞, or Re,

$$Re \cong 1.1(\tilde{S}+1)\left(\frac{\tilde{P}}{\tilde{H}}\right)^{1/2}, \quad \text{with} \quad \tilde{S} = \frac{S}{D}, \qquad \tilde{H} = \frac{H}{D} \tag{4.4}$$

where $\tilde{P}$ is the dimensionless pressure group identified by Bhattacharjee and Grosshandler (1988)

$$\tilde{P} = \frac{\Delta P \cdot D^2}{\mu \nu} \tag{4.5}$$

Combining equations (4.1) - (4.6) we find that the total heat transfer rate behaves as

$$q_{large S} \cong 2kL\frac{W}{D}(T_w - T_\infty)\frac{\tilde{H}^{3/4}\tilde{P}^{1/4}Pr^{0.37}}{(\tilde{S}+1)^{3/2}} \tag{4.6}$$

Consider now the opposite extreme when the cylinders almost touch, and the flow is almost cut off. In this limit the temperature of the coolant that exits slowly through the right end of the bundle (the plane $L \times W$) is essentially the same as the cylinder temperature T_w. The heat transfer from the bundle to the coolant is equal to the enthalpy gained by the coolant, $q = \dot{m}c_P(T_w - T_\infty)$, where $\dot{m}$ is the mass flowrate through the $L \times W$ plane.

To obtain an order-of-magnitude estimate for the flowrate, we note that $\dot{m}$ is composed of several streams [total number $n_t \cong W/(S+D)$], each with a cross-sectional area $S \times L$ in the plane of one row of cylinder axes. The thickness of the channel traveled by each stream

varies between a minimum value (S) at the row level, and a maximum value at a certain level between two rows. The volume-averaged thickness of one channel of this kind is

$$\overline{S} = S + D - 0.907\frac{D^2}{S + D} \tag{4.7}$$

however, we may adjust this estimate by using 1 in place of the factor 0.907 to account for the fact that the flow *must* cease when the cylinders touch $(S = 0)$:

$$\overline{S} = S\frac{S + 2D}{S + D} \tag{4.8}$$

The mean velocity U through a channel of length H and cross-sectional area $\overline{S}L$ can be estimated using the solution for Hagen-Poiseuille flow through a parallel plate channel of spacing $\overline{S}$ and length H,

$$U \cong \frac{\overline{S}^2 \Delta P}{12\mu H} \tag{4.9}$$

The mass flowrate through one channel is $\dot{m}_1 = \rho U \overline{S} L$. There are n_t channels, therefore the mass flowrate through the entire bundle is $\dot{m} = \dot{m}_1 W/(S + D)$, and q becomes

$$q_{smallS} \cong \frac{1}{12}kL\frac{W}{D}(T_w - T_\infty)\frac{\tilde{P}Pr\tilde{S}^3(\tilde{S} + 2)^3}{\tilde{H}(\tilde{S} + 1)^4} \tag{4.10}$$

The two asymptotic trends are sketched in Fig. 4.2. The actual (unknown) curve $q(S)$, which is indicated by the solid line in the figure, has a maximum where the spacing S is approximately the same as the S value obtained by intersecting the two asymptotes (Bejan and Sciubba, 1992). The S_{opt} value obtained by eliminating q between equations (4.6) and (4.10) is given implicitly by

$$\tilde{S}_{opt}\frac{(2 + \tilde{S}_{opt}^{-1})^{6/7}}{(1 + \tilde{S}_{opt}^{-1})^{5/7}} \cong 2.5\frac{\tilde{H}^{1/2}}{\tilde{P}^{3/14}Pr^{0.18}} \tag{4.11}$$

The optimal spacing increases with the length of the bundle, and decreases with the applied pressure difference and the Prandtl number. It is also interesting that in equation (4.11) the exponents of $\tilde{P}$ and Pr are almost the same (note that $3/14 = 0.21$). This means that instead of the product $\tilde{P}^{3/14}Pr^{0.18}$ we may use approximately $\Pi^{3/14}$, Fig. 4.3,

$$\tilde{S}_{opt}\frac{(2 + \tilde{S}_{opt}^{-1})^{6/7}}{(1 + \tilde{S}_{opt}^{-1})^{5/7}} \cong 2.5\frac{\tilde{H}^{1/2}}{\Pi^{3/14}} \tag{4.12}$$

where the Π group is defined as $\Pi = \Delta P \cdot D^2/(\mu\alpha) = \tilde{P}Pr$, (Bejan, 1993). The intersection of the large-S and small-S regimes provides also an estimate for the scale of the maximum
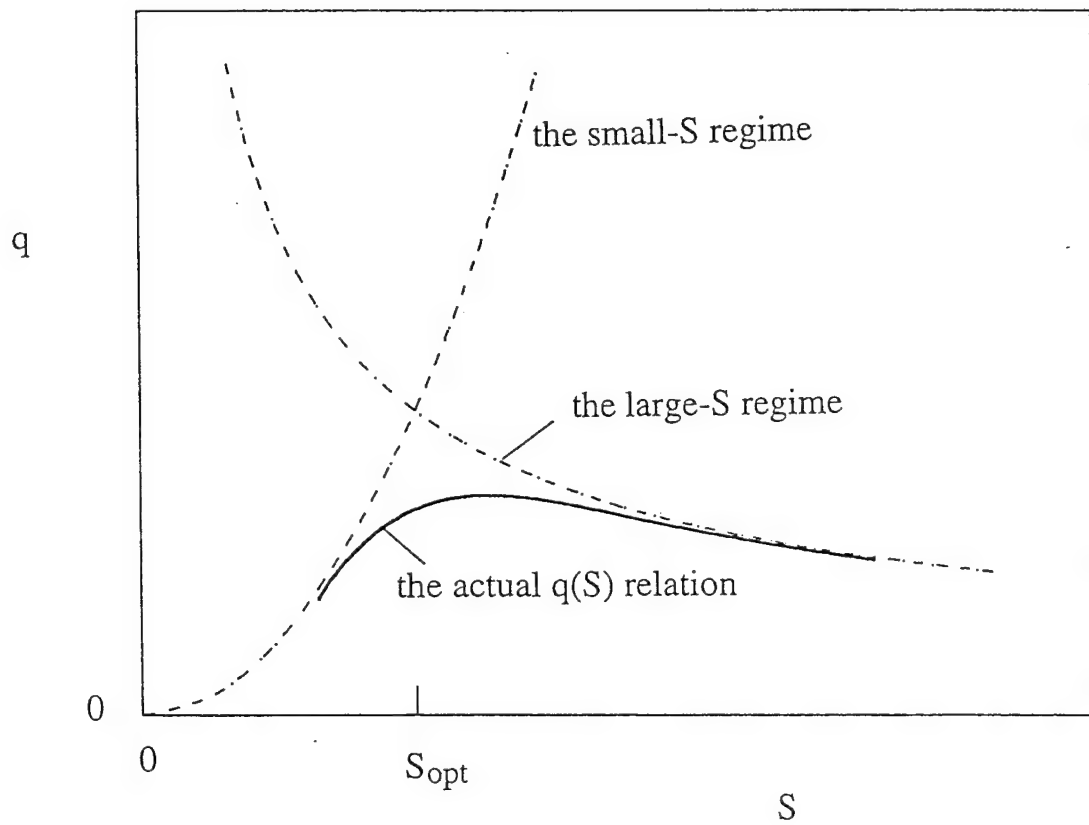
Figure 4.2: The optimal cylinder-to-cylinder spacing as the intersection of the large-S and small-S asymptotes.
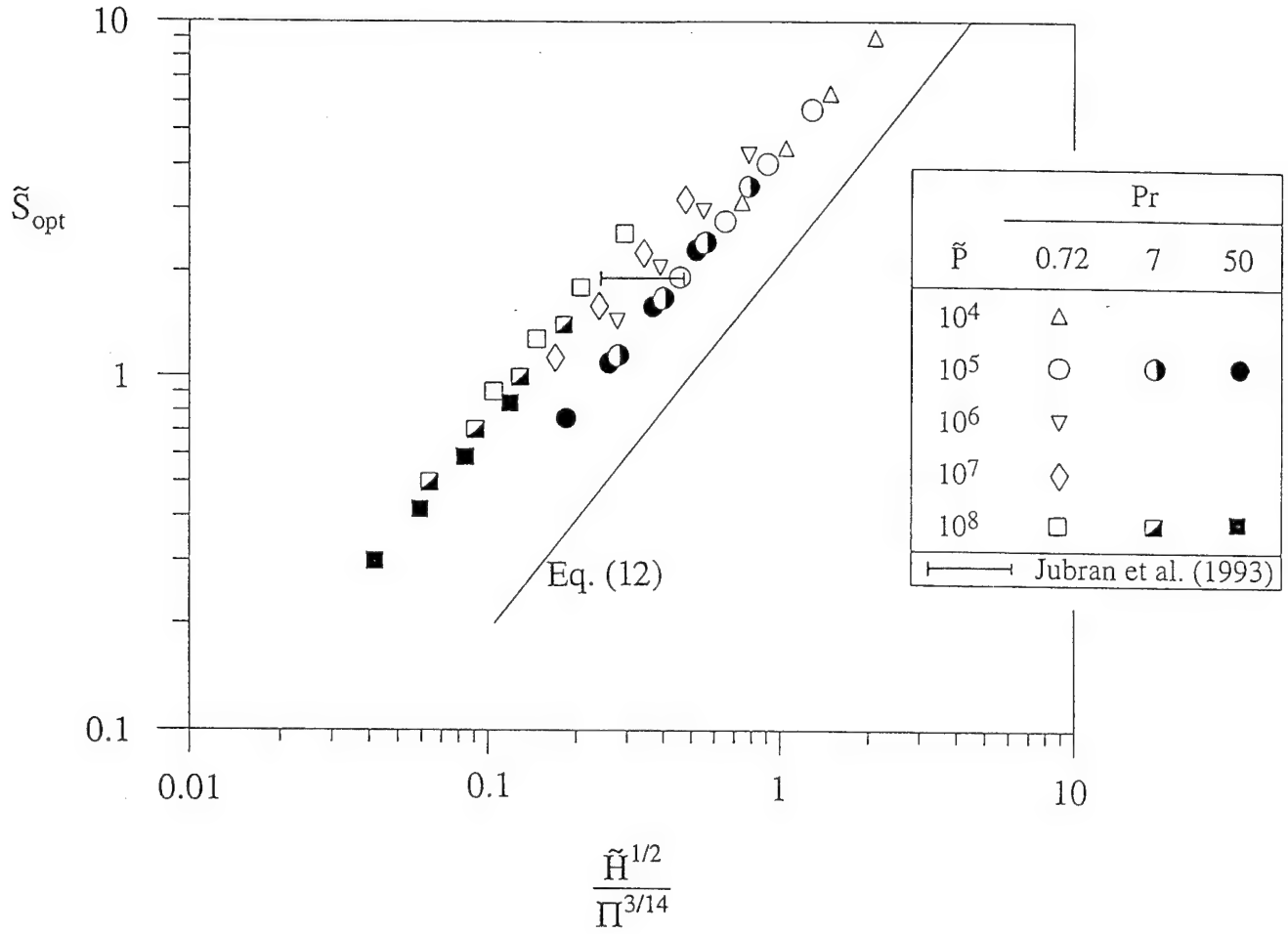
Figure 4.3: The optimal cylinder-to-cylinder spacing as a function of the bundle flow length, applied pressure difference, and Prandtl number.

thermal conductance between bundle and coolant, $q/(T_w - T_\infty)$. Figure 4.2 shows that the result of this operation will always overestimate the peak value of the actual $q/(T_w - T_\infty)$ curve:

$$\left[\frac{kLW}{qD}(T_w - T_\infty)\right]_{min} \geq \frac{1.85}{\tilde{P}^{4/7} Pr^{3/7}} \tag{4.13}$$

4.3 Estimates Based on Experimental Correlations for Cross-Flow

Now that we have theoretical reasons to expect an optimal spacing and a scaling of type (4.13), we turn our attention to a more precise analysis that is based on published experimental data. A very large effort has been devoted to documenting the pressure drop and heat transfer coefficient for bundles of parallel cylinders in cross-flow (e.g. Zukauskas, 1987b). These results are expressed in terms of the Reynolds number based on the maximum average velocity between adjacent cylinders, $Re_{max} = V_{max}D/\nu$. To determine the relation between the applied pressure difference and Re_{max} we use

$$\Delta P = n_\ell f \chi \frac{1}{2} \rho V_{max}^2 \tag{4.14}$$

with $\chi = 1$ for the equilateral triangle array, and n_ℓ for the number of rows in the flow direction, $n_\ell = 1 + (\tilde{H} - 1)/0.866(\tilde{S} + 1)$. Equation (4.14) becomes

$$\tilde{P} = \frac{1}{2} n_\ell f Re_{max}^2 \tag{4.15}$$

The friction factor f is available in graphic form (see Fig. 6.20 in Zukauskas, 1987b) as a function of Re_{max} and cylinder-to-cylinder spacing. In the range $10 < Re_{max} < 10^4$ and $0.25 \leq \tilde{S} \leq 1.5$, the f curves are approximated within 10 percent by $f = (C_1/Re_{max}) + C_2$, where $C_1 = 68\tilde{S}^{-0.76}$ and $C_2 = 0.37\tilde{S}^{-0.31}$. Equation (4.15) provides the function $Re_{max}(\tilde{P}, \tilde{S})$ that accounts for the flow part of the problem.

When the total heat transfer q is divided equally among the cylinders the peak temperature (T_{max}) belongs to the cylinders positioned in the last row. The maximum temperature difference $(T_{max} - T_\infty)$ can be calculated in two steps (Knight $et\ al.$, 1991),

$$T_{max} - T_{out} = \frac{(q/n)D}{\pi DLkNu} \quad \text{and} \quad T_{out} - T_\infty = \frac{q}{\dot{m}c_P} \tag{4.16}$$

where T_{out} is the bulk temperature of the fluid leaving the bundle, $\dot{m} = \rho V_{max} S L n_t$ is the total mass flowrate, and $n_t = W/(S + D)$. Eliminating T_{out} we obtain

$$\tilde{T} = \frac{kLW}{qD}(T_{max} - T_\infty) = \frac{\tilde{S} + 1}{\pi n_\ell Nu} + \frac{\tilde{S} + 1}{\tilde{S} Pr Re_{max}} \tag{4.17}$$

where $\tilde{T}$ is the dimensionless maximum temperature difference. Finally, we assume that there are many cylinders in the longitudinal flow direction ($n_\ell > 16$), such that the Nusselt number for the last row is the same as the value averaged over the entire bundle. The numerical results reported below were developed using Table 6.3 of Zukauskas (1987b).

In conclusion, the result of combining equations (4.15) and (4.17) is a maximum temperature difference function $\tilde{T}$ that depends on $\tilde{P}, \tilde{H}, Pr$ and $\tilde{S}$. The $\tilde{T}$ function can be minimized numerically with respect to the spacing $\tilde{S}$, to obtain the optimal spacing $\tilde{S}_{opt}(\tilde{P}, \tilde{H}, Pr)$. Figure 4.3 shows the $\tilde{S}_{opt}$ results obtained for a total of 36 $\tilde{P}, \tilde{H}$ and Pr combinations in the range $10^4 \leq \tilde{P} \leq 10^8$, $25 \leq \tilde{H} \leq 200$, and $0.72 \leq Pr \leq 50$. In conclusion, the estimate obtained in the preceding section is adequate as intended (i.e. in an order of magnitude sense), and the predicted trends are also correct.

The scatter of the points plotted in Fig. 4.3 suggests that the use of the combined group $\tilde{H}^{1/2}/\Pi^{3/14}$ on the abscissa may not be the best way to correlate the empirical data. After examining individually the effects of $\tilde{H}, \tilde{P}$ and Pr on $\tilde{S}_{opt}$, we found that the following correlation approximates the data with a standard deviation of 5.6 percent:

$$\tilde{S}_{opt} = 1.59 \frac{\tilde{H}^{0.52}}{\tilde{P}^{0.13} Pr^{0.24}} \tag{4.18}$$

The minimum last-row (i.e. peak) temperature occurs when the spacing is optimal, $\tilde{T}_{min} = \tilde{T}(\tilde{S}_{opt})$. The $\tilde{T}_{min}$ values for the 36 cases documented in Fig. 4.3 are correlated with a standard deviation of 16 percent by the expression

$$\tilde{T}_{min} = \frac{3.33}{\tilde{P}^{0.45} Pr^{0.64}} \tag{4.19}$$

In both equations (4.13) and (4.19), the denominator on the right-hand side is approximated well by $\Pi^{1/2}$. This allows us to rewrite equation (4.19) as the maximum power density installed in the fixed volume HLW,

$$\frac{q}{HLW} \sim 0.3 \Pi^{1/2} \frac{k(T_{max} - T_\infty)}{HD} \tag{4.20}$$

We note that Π is proportional to D^2, therefore the maximum power density does not depend on the cylinder diameter. Important is to set the spacing S *in proportion to D*, c.f. equation (4.18).

4.4 Concluding Remarks

It is instructive to compare the optimal spacing reported by Jubran *et al.* (1993) with the data plotted in Fig. 4.3. In the present notation, Jubran *et al.*'s conclusion reads $\tilde{S}_{opt} = 1.89$, and was reached during experiments with air flow through arrays of parallel pin fins ($D = $

84

6.35 mm, $L = 60$ mm) attached to a base plate ($H = 300$ mm, $W = 175$mm). A direct comparison with the present results is not possible because in Jubran et $al.$'s experiments S was varied at constant air mass flowrate (or constant upstream velocity, U_{in}), instead of constant ΔP. The experiments covered the U_{in} range 2.2 - 10m/s.

An order of magnitude comparisons can be made, however, by noting that when $\tilde{S} \sim 2$ the array is dense and long enough such that the overall ΔP scale is $\Delta P \sim \frac{1}{2}\rho U_{in}^2$. The array appears "dense" from the point of view of the approaching stream, to which the array looks opaque (without clear openings). The stream has two choices, to penetrate the array, or to flow around it (Morega et $al.$, 1994). It does both, with less penetration as $\tilde{S}$ decreases.

If we use this approximation we find that Jubran et $al.$'s experiments cover a range characterized by $4.2 \times 10^5 < \tilde{P} < 9 \times 10^6$, $\tilde{H} = 47.3$ and $Pr = 0.72$. Their conclusion that $\tilde{S}_{opt} = 1.89$ is shown as a horizontal bar in Fig. 4.3, and agrees very well with the $\tilde{S}_{opt}$ values determined by minimizing the $\tilde{T}$ expression of equation (4.17). This agreement is remarkable especially in view of the fact that in Jubran et $al.$'s experiments the cylinders were pin fins attached to a base surface, i.e. the cylinders were not long relative to their diameter, their temperature varied along their length, and the time-averaged flow was not two-dimensional.

The same ΔP approximation can be used to convert the empirical correlations (4.18) and (4.19) into order-of-magnitude formulas for bundles exposed to a free stream of velocity U_{in},

$$\tilde{S}_{opt} \sim 1.7 \frac{\tilde{H}^{0.52}}{Re_{in}^{0.26} Pr^{0.24}}, \qquad \tilde{T}_{min} \sim \frac{4.5}{Re_{in}^{0.9} Pr^{0.64}} \qquad (4.21)$$

where $Re_{in} = U_{in}D/\nu$, which is the same as $Re_{in} \sim (2\tilde{P})^{1/2}$. The correlations (4.21), cover the range $140 < Re_{in} < 14000$, $25 < \tilde{H} < 200$, and $0.72 < Pr < 50$.

The relative progress made in this chapter is illustrated in Fig. 4.3. Known until now was the single point reported by Jubran et $al.$ (1993): the point (horizontal bar) shown in Fig. 4.3, however, is more general because the cartesian coordinates are dimensionless. These coordinates are the product of this chapter. The other product is the complete curve, equation (4.18), which is based on experimental heat and fluid flow data, and covers all the possible flow conditions.

4.5 Notation

$C_{1,2}$ functions of $\tilde{S}$

C_D drag coefficient

D	cylinder diameter
f	friction factor
F_1	drag force per cylinder
h	average heat transfer coefficient
H	bundle flow length
$\tilde{H}$	dimensionless length, H/D
k	coolant thermal conductivity
L	cylinder length
$\dot{m}$	total mass flowrate
n	total number of cylinders
n_l	number of rows in the longitudinal direction
n_t	number of rows in the transversal direction
Nu	average Nusselt number, $hD\,/k$
$\tilde{P}$	pressure drop number, $\Delta P \cdot D^2/(\mu\nu)$
q	total heat transfer rate
q_1	heat transfer rate per cylinder
Re, Re_{in}, Re_{max}	Reynolds numbers, $U_\infty D/\nu,\ U_{in}D/\nu,\ V_{max}D/\nu$
S	cylinder-to-cylinder spacing
$\tilde{S}$	dimensionless spacing, S/D
$\overline{S}$	average spacing
$\tilde{T}$	dimensionless maximum temperature difference
T_{out}	coolant outlet temperature
T_w	cylinder temperature scale
T_∞	coolant inlet temperature

U	mean velocity
U_{in}	inlet free-stream velocity
U_∞	free-stream velocity around one cylinder
V_{max}	maximum average velocity
W	bundle width
α	coolant thermal diffusivity
ΔP	pressure difference
μ	viscosity
ν	kinematic viscosity
Π	pressure drop number, $\Delta P \cdot D^2/(\mu\alpha)$
ρ	coolant density
χ	correction factor

Chapter 5

THE OPTIMAL SIZES OF BODIES WITH EXTERNAL FORCED CONVECTION HEAT TRANSFER

5.1   Introduction

External forced convection is one of the most common heat transfer modes that occur in the heat exchangers used in the power and refrigeration industry (e.g. plate and cylindrical fins, tubes in cross-flow). It is also well known that each heat transfer process is accompanied by entropy generation, which a quantity proportional to the corresponding useful work (exergy) destroyed by the power or refrigeration plant. The ways to minimize the generation of entropy in such processes have become a fundamental topic in contemporary heat transfer.

The objective of this chapter is to show how to optimize the size of a body engaged in external forced convection, when its heat transfer duty is specified. Two optimization approaches are used. The first is based on minimizing the total rate of entropy generation due to fluid friction and imperfect thermal contact. In the second approach, the minimized quantity is the total cost associated with the material of the body and the imperfect heat transfer.

5.2   Optimal Sizes for Minimum Entropy Generation

The rate of entropy generation associated with external forced convection is, in general (Bejan, 1982, 1988),

$$\dot{S}_{gen} = \frac{q\left(\overline{T}_w - T_\infty\right)}{T_\infty^2} + \frac{F_D U_\infty}{T_\infty} \tag{5.1}$$

In writing equation (5.1) it is assumed that the surface-averaged temperature difference between the body and the free stream $(\overline{T}_w - T_\infty)$ is at least one order of magnitude smaller than the absolute temperature T_∞. The two terms on the right-hand side of equation (5.1) represent, in order, the contribution due to heat transfer across a finite temperature difference, and the contribution due to fluid friction. The first applications of equation (5.1) were to the flat plate with laminar and turbulent boundary layer flow (Bejan, 1982, Example 5.3 and Problem 5.4) and the sphere (Bejan, 1982, Problem 5.3), where it was shown that the body dimension can be selected such that $\dot{S}_{gen}$ is minimized. The cylinder in cross-flow and the flat plate with turbulent boundary layer flow were optimized by Poulikakos and Johnson (1989). We begin the correlation work by extending the existing results to wider Reynolds number ranges.

5.2.1   The smooth cylinder in cross-flow. Consider the heat transfer and friction between a long cylinder of diameter D and length W, and a uniform cross-flow (U_∞, T_∞). The total heat transfer rate (the heat transfer duty) is fixed, $q = h\pi DW\left(\overline{T}_w - T_\infty\right)$, where $\overline{T}_w$ is the perimeter averaged temperature. The heat transfer coefficient h can be estimated based on

88

Churchill and Bernstein's (1977) correlation, which is valid for all values of Re_D and Pr, provided $Re_D Pr > 0.2$. The total drag force is $F_D = C_D DW \rho U_\infty^2 / 2$, for which the relationship between the drag coefficient C_D and Re_D is available in graphical form (e.g. Bejan, 1993, p. 266). We digitized and curve-fitted the $C_D(Re_D)$ data in the Re_D range $0.1 - 10^5$, and substituted this information into the second term on the right side of equation (5.1),

$$\frac{\dot{S}_{gen}/W}{\mu U_\infty^2 / T_\infty} = \frac{B^2 Pr^{1/3}}{\pi Nu (Re_D, Pr)} + \frac{1}{2} Re_D C_D (Re_D) \tag{5.2}$$

where $Nu = hD / k$ and B is the nondimensional heat transfer duty parameter of the cylinder,

$$B = \frac{q / W}{U_\infty \left(k \mu T_\infty Pr^{1/3} \right)^{1/2}} \tag{5.3}$$

We minimized the expression (5.2) numerically by choosing the optimal diameter (dimensionless $Re_{D, opt}$) for a given (B, Pr) pair. The B definition (5.3) was chosen in such a way that the results can be projected as a single curve $Re_{D, opt}$ (B) in Fig. 5.1, if the Prandtl number is 0.7 or greater.

5.2.2 The smooth sphere. The same optimization method can be applied to a sphere (D) with heat transfer to an external flow (U_∞, T_∞). For conciseness, we show only the beginning and the end of the analysis. The overall Nusselt number can be estimated based on Whitaker's (1972) correlation, which has been tested for $0.71 < Pr < 380$ and $3.5 < Re_D < 7.6 \times 10^4$. The drag force is $F_D = C_D \left(\pi D^2 / 4 \right) \rho U_\infty^2 / 2$ where $C_D(Re_D)$ is the drag coefficient (Bejan, 1993). After making this substitution for F_D in equation (5.1) we were able to write

$$\frac{\dot{S}_{gen}}{v^2 \rho U_\infty / T_\infty} = \frac{B_s^2 Pr^{1/3}}{\pi Re_D Nu (Re_D, Pr)} + \frac{\pi}{8} Re_D^2 C_D (Re_D) \tag{5.4}$$

where, $Nu = hD / k$, and the given heat transfer rate is $q = h \pi D^2 \left(\overline{T}_w - T_\infty \right)$. We minimized this expression numerically with respect to Re_D, and plotted the resulting $Re_{D, opt}$ values versus B_s in Fig. 5.1. Once again, B_s was chosen such that the results are represented by a single curve when $Pr > 0.7$. The sphere heat transfer duty parameter B_s is defined by

$$B_s = \frac{q}{v \left(k \mu T_\infty Pr^{1/3} \right)^{1/2}} \tag{5.5}$$

5.2.3 The flat plate in parallel flow. Projected on Fig. 5.1 are also the results known for the flat plate of length L, with the heat flux q'' on both sides. The total heat transfer rate is fixed, $q = 2 L W q''$, where W is the plate width. Using the present nondimensionalization approach, the results known for laminar boundary layer flow ($Re_L < 5 \times 10^5$) can be summarized here as
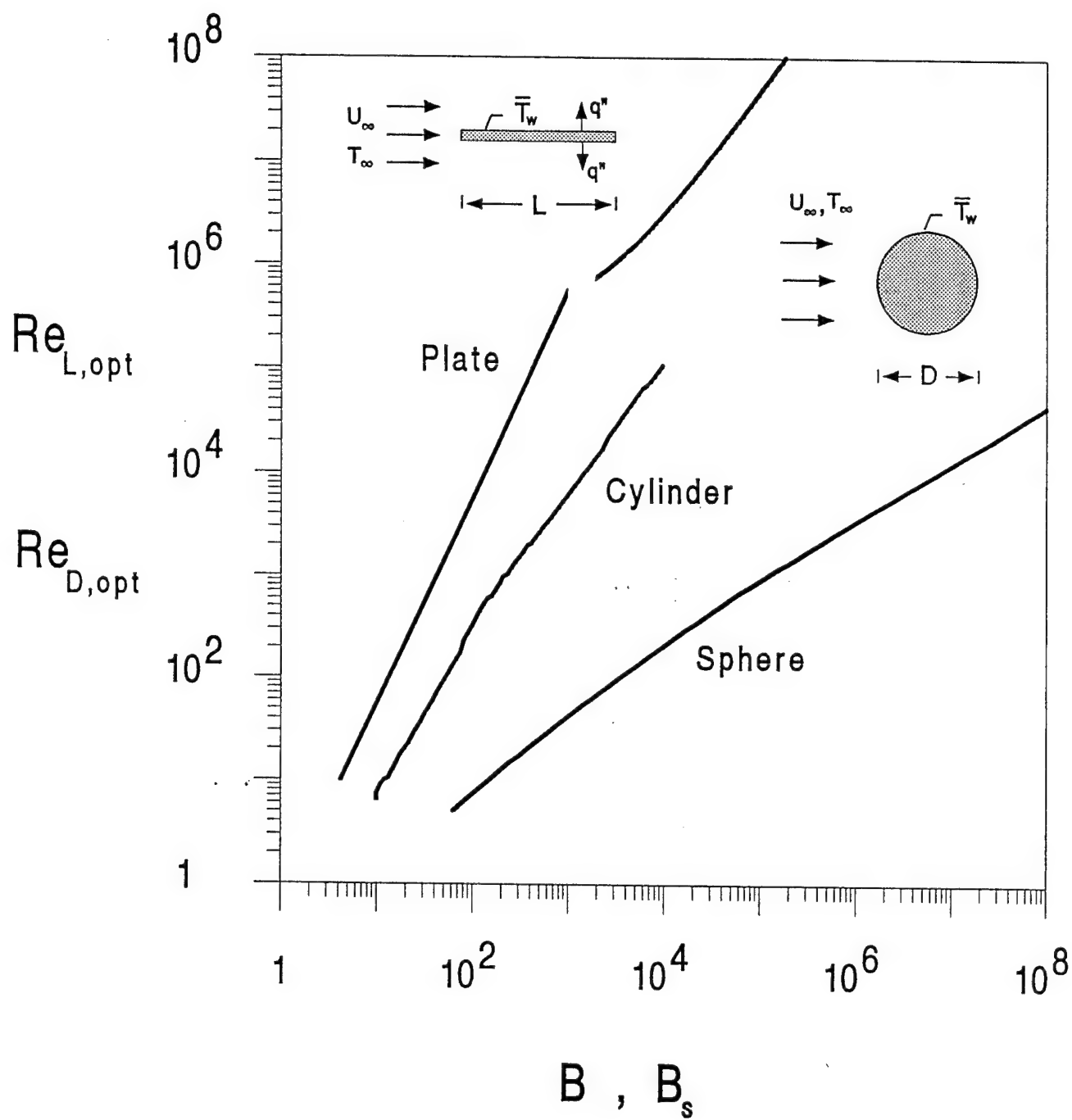
Figure 5.1   The optimal sizes of a plate, cylinder and sphere for minimum entropy generation.

90

$$Re_{L,opt} = 0.554 B^2, \quad \frac{\dot{S}_{gen,min}/W}{\mu U_\infty^2 / T_\infty} = 2B \tag{5.6}$$

For the optimization of the flat plate in the turbulent boundary layer regime, a wider Re_L range (5×10^5 - 10^8) is covered by the correlation (e.g. Bejan, 1993, p. 261): $q''L/k(\overline{T}_w - T_\infty) = 0.037 \, Pr^{1/3} (Re_L^{4/5} - 23{,}550)$. To estimate the drag force $F_D = 2LW\overline{\tau}$ we used $\overline{\tau} = 0.037 \, \rho \, U_\infty^2 \, Re_L^{-1/5}$. The optimal Re_L that minimizes the resulting $\dot{S}_{gen}$ expression is (Fig. 5.1)

$$Re_{L,opt} = (13.51B + 23{,}550)^{5/4} \tag{5.7}$$

5.2.4 Effective length, and universal duty parameter. The main contribution of the dimensionless chart constructed in Fig. 5.1 is to show that the optimal size of the object ($Re_{D,opt}$, $Re_{L,opt}$) increases *monotonically* with its respective duty parameter (B, B_s). The challenge then is to identify a more general set of coordinates in which the three curves of Fig. 5.1 fall on the same curve.

A step in this direction is presented in Fig. 5.2. The parameter that is used now on the ordinate for the flat plate is the Reynolds number based on the boundary layer thickness at the trailing edge, $Re_{\delta,opt} = U \delta_{opt} / \nu$. We made this choice because δ is the *transversal* length scale of the flow, i.e. the same type of flow length scale as the thickness of the wake (D) behind the cylinder and the sphere. For the laminar regime on the flat plate we used the estimate $\delta \cong 4.92 \, L \, Re_L^{-1/2}$, so that equation (5.6) was replaced by $Re_{\delta,opt} = 3.66B$. For the turbulent regime we used $\delta \cong 0.37 \, L \, Re_L^{-1/5}$ and replaced equation (5.7) with $Re_{\delta,opt} = 0.37 \, (13.51B + 23{,}550)$.

The abscissa of Fig. 5.2 shows the duty parameter B of equation (5.3), which was defined in the same way for the cylinder and the plate, and the new parameter B_* for the sphere. The latter is based on the observation that the B and B_s definitions (5.3) and (5.5) differ with respect to the way in which the heat transfer duty is specified, q / W as opposed to q. We can construct a sphere duty parameter of type B, by regarding the spherical surface πD^2 as equal (in an order of magnitude sense) to the lateral surface of a short cylinder ($D_c = W$) in cross-flow and with insulated ends. From the area conservation statement $\pi D^2 = \pi D_c W$ we learn that $D_c = D$, in other words, the diameter of the equivalent short cylinder is the same as that of the actual sphere. By substituting D in place of W in the B definition (5.3), we arrive at the B-type duty parameter for the sphere

$$B_* = \frac{q/D}{U_\infty \left(k \mu T_\infty \, Pr^{1/3} \right)^{1/2}} = \frac{B_s}{Re_{D,opt}} \tag{5.8}$$

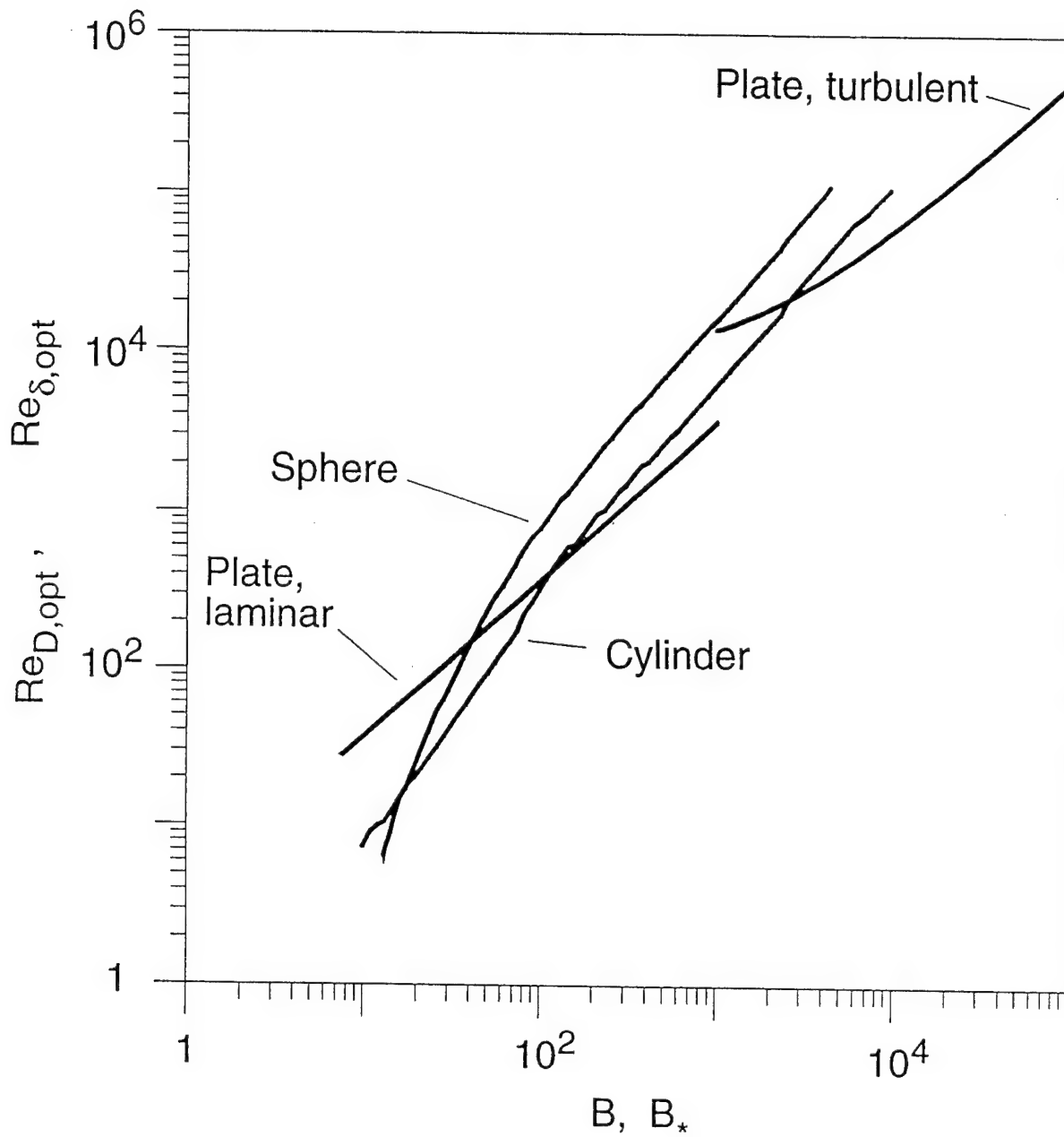Figure 5.2 shows that the consistent use of the transversal length scale and the duty

Figure 5.2   The optimal sizes of Fig. 5.1 correlated in terms of a universal duty parameter (B, B∗) and the Reynolds number based on the transversal length scale of the flow.

parameter of type B brings the curves much closer than in the original plot of Fig. 5.1. This discovery suggests that the unknown (and, presumably, more complicated) curve that represents a body of another shape will fall not far from the curves of Fig. 5.2, provided the ordinate and abscissa parameters are defined in a manner consistent with those of Fig. 5.2.

5.3 Optimal Sizes for Minimum Cost

5.3.1 When heat transfer losses dominate. To see the reasons for the alternative approach followed in this section, we begin with a numerical example. The question pursued in this example is how the optimal sizes of Fig. 5.1 compare with the usual sizes that occur in real-life applications. It is sufficient to use a textbook example like the one given on p. 415 in Incropera and DeWitt (1990). A cylinder with D = 1.27 cm, W = 9.4 cm and q = 39.1 W is cooled in a cross-flow of air with $U_\infty = 10$ m/s and $T_\infty = 300$ K. If we evaluate the air properties at the film temperature 335 K, the duty parameter calculated with equation (5.3) is B $\cong$ 3400. We place this value on the abscissa of Fig. 1, and read $Re_{D, opt} \cong 3.5 \times 10^4$, from which we deduce that $D_{opt} \cong 6.6$ cm.

In conclusion, in this example the actual diameter (1.27 cm) is roughly one order of magnitude smaller than the optimal diameter for minimum total entropy generation. When D < D_{opt} the total entropy generation rate is dominated by the contribution made by heat transfer. The question then is how to determine the size of an object with forced convection heat transfer when its irreversibility is *dominated by heat transfer irreversibility*. The way to reduce the heat transfer irreversibility when the heat transfer duty is fixed is by increasing the size (or wetted surface) of the immersed object. This increase in size is always accompanied by an increase in the cost of the object itself. We arrive in this way at a trade-off between saving exergy and spending more on a larger object.

In this section we examine this trade-off by putting both the destroyed exergy and the object on a cost basis. According to equation (5.1), the entropy generation rate due to heat transfer is $q(\overline{T}_w - T_\infty)/T_\infty^2$. We multiply this by the absolute temperature T_∞ and obtain the corresponding rate of exergy destruction in the installation that employs the object as a heat transfer device, $q(\overline{T}_w - T_\infty)/T_\infty$. The exergy destroyed during the lifetime of operation t_0 is $t_0 q(\overline{T}_w - T_\infty)/T_\infty$. The cost associated with this quantity is $c_e t_0 q(\overline{T}_w - T_\infty)/T_\infty$, where $c_e(\$/J)$ is the unit cost of exergy (e.g. electric energy from the network).

5.3.2 The smooth cylinder in cross-flow. If the object (cylinder, in this case) is solid, its cost is proportional to its volume, $c_m(\pi/4) D^2 W$, where $c_m(\$/m^3)$ is the unit cost of the cylinder material. This unit cost may refer to the purchase of the material if the material is expensive, or to its weight if the entire installation is to be part of an aerospace application. In summary, the two cost items can be linked into an additive cost formula,

$$C = c_e t_o q \left(\frac{\overline{T}_w}{T_\infty} - 1 \right) + c_m \frac{\pi}{4} D^2 W \qquad (5.9)$$

which can be nondimensionlized as

$$\frac{C/W}{c_m (v/U_\infty)^2} = \frac{F^2 Pr^{1/3}}{\pi Nu} + \frac{\pi}{4} Re_D^2 \qquad (5.10)$$

The dimensionless heat transfer duty parameter is now

$$F = \frac{q/W}{v/U_\infty} \left(\frac{c_e t_o}{c_m k T_\infty Pr^{1/3}} \right)^{1/2} \qquad (5.11)$$

The Nusselt number Nu (Re_D, Pr) is given by the Churchill and Bernstein (1977) correlation. The optimal Reynolds number for which the total cost of equation (5.10) is minimized emerges as a single curve of $Re_{D, opt}$ versus F when Pr > 0.7. This curve is shown in Fig. 5.3.

5.3.3 The smooth sphere. The minimization of the cost associated with a solid sphere can be performed in a similar way. The second term on the right side of equation (5.9) is replaced by $c_m (\pi/6)D^3$, so that the dimensionless total cost formula becomes

$$\frac{C}{c_m} \left(\frac{U_\infty}{v} \right)^3 = \frac{F_s^2 Pr^{1/3}}{\pi Re_D Nu} + \frac{\pi}{6} Re_D^3 \qquad (5.12)$$

where

$$F_s = q \left(\frac{U_\infty}{v} \right)^2 \left(\frac{c_e t_o}{c_m k T_\infty Pr^{1/3}} \right)^{1/2} \qquad (5.13)$$

By using the Nu (Re_D, Pr) correlation given by Whitaker (1972), it is possible to minimize the expression (5.12) with respect to Re_D. The results can be plotted as a single curve if Pr > 0.7, Fig. 5.3.

5.3.4 The flat plate. If the boundary layer flow is laminar and the heat flux q'' is uniform on both sides of the plate, the two-term cost formula reduces to

$$\frac{C/W}{c_m t \, v/U_\infty} = 0.736 \, F^2 Re_L^{-1/2} + Re_L \qquad (Pr > 0.5) \qquad (5.14)$$

where t is the plate thickness, t << L, and

$$F = \frac{q/W}{(t \, v/U_\infty)^{1/2}} \left(\frac{c_e t_o}{c_m k T_\infty Pr^{1/3}} \right)^{1/2} \qquad (5.15)$$
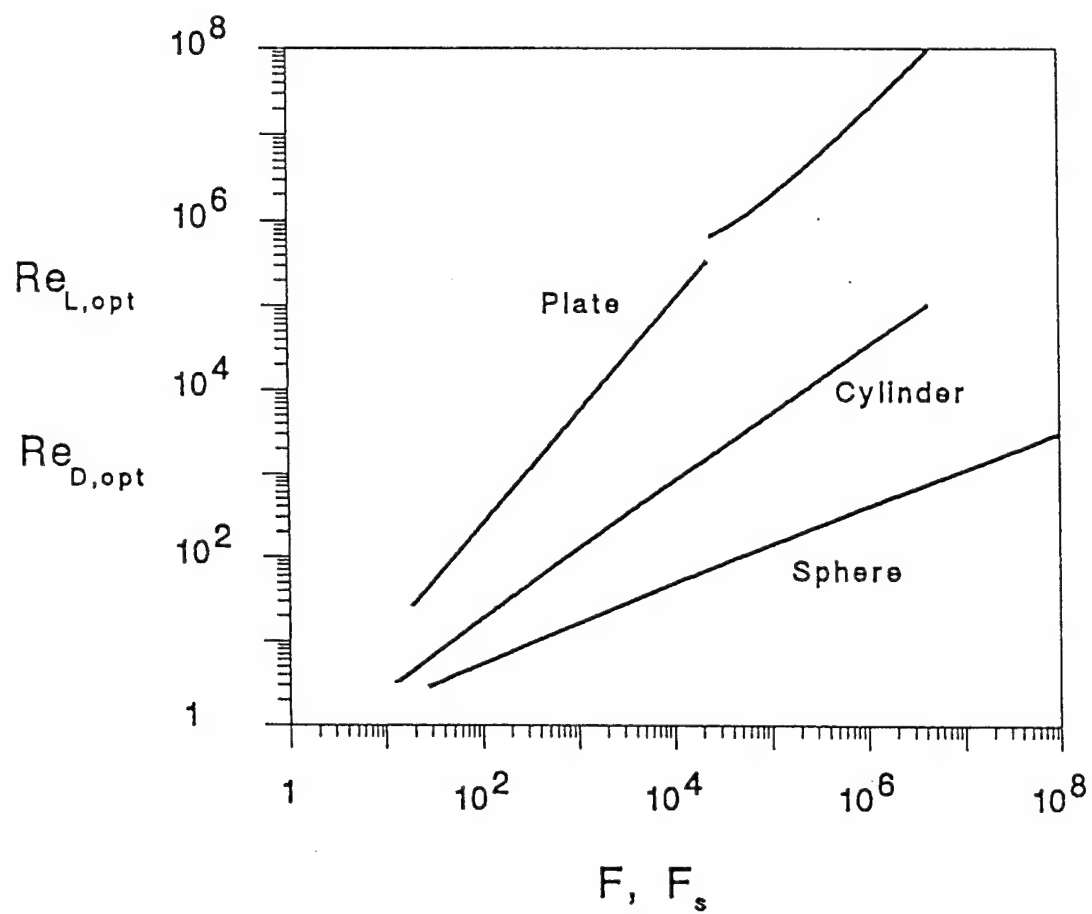
The optimal plate length that minimizes the total cost is

Figure 5.3 The optimal sizes of a plate, cylinder and sphere for minimum cost.

$$Re_{L,\,opt} = 0.514\,F^{4/3} \tag{5.16}$$

For cases in which the flow is turbulent, we use the correlation listed under equation (5.6) and obtain a relation similar to equation (5.14), except that the first term on the right side is replaced by $13.51\,F^2/\left(Re_L^{4/5} - 23{,}550\right)$. The end result is that the optimal plate length for minimum cost is described implicitly by

$$F = 0.304\left(Re_{L,\,opt}^{9/10} - 23{,}550\,Re_{L,\,opt}^{1/10}\right) \tag{5.17}$$

where the duty parameter F continues to be defined as in equation (5.15). Both equations (5.16) and (5.17) have been added to Fig. 5.3.

5.3.5 Correlation of the optimal sizes of the cylinder, sphere and plate. The results assembled in Fig. 5.3 look remarkably similar to those in Fig. 5.1. These similarities are due to the fact that the new dimensionless duty parameters (F, F_s) were carefully chosen so that they have the same structure as the abscissa parameters of Fig. 5.1. This means that we should be able to correlate the three curves of Fig. 5.3 into a universal curve, by following the method of section 5.2.4, which led to Fig. 5.2.

First, in place of the sphere duty parameter F_s we use the equivalent parameter of type F [equation (5.11)] by imagining a short cylinder $(D = W)$ that has a cylindrical area equal to that of the sphere,

$$F_* = \frac{q/D}{v/U_\infty}\left(\frac{c_e\,t_o}{c_m\,k\,T_\infty\,Pr^{1/3}}\right)^{1/2} = \frac{F_s}{Re_D} \tag{5.18}$$

The relation between the abscissas of Figs. 5.3 and 5.4 for the sphere is $F_* = F_s/Re_{D,\,opt}$. Second, for the plate we base the Reynolds number on the transversal length scale of the flow, which is $\delta \cong 4.92\,L\,Re_L^{-1/2}$ in the laminar regime, and $\delta \cong 0.37\,L\,Re_L^{-1/5}$ in the turbulent regime. The ordinate for the plate changes to $Re_{\delta,\,opt} = U_\infty\delta_{opt}/v$, and equations (5.16) and (5.17) are replaced by $Re_{\delta,\,opt} \cong 3.53\,F^{2/3}$ and, respectively, $F = 0.0173\,Re_{\delta,\,opt}^{9/5} - 5206\,Re_{\delta,\,opt}^{1/5}$. Figure 5.4 shows once again that this method of correlation (transversal length scale on the ordinate and cylinder-type duty parameter on the abscissa) works very well.

5.4 Conclusions

In this chapter we showed how to optimize the size of a body with external forced convection when the heat transfer duty is specified, and when the total entropy generation rate or the total cost must be minimized. We illustrated the two methods by modelling the body as a cylinder, sphere or flat plate.

The main conclusion made visible by the charts of Figs. 5.1 and 5.3 is that the optimal size increases monotonically with the heat transfer duty parameter. The chief objective of the

Re$_{\delta,opt}$

Re$_{D,opt}$

10^8

10^6

10^4

10^2

1

Plate, turbulent

Cylinder

Plate, laminar

Sphere

1   10^2 10^4 10^6 10^8 10^{10} 10^{12}
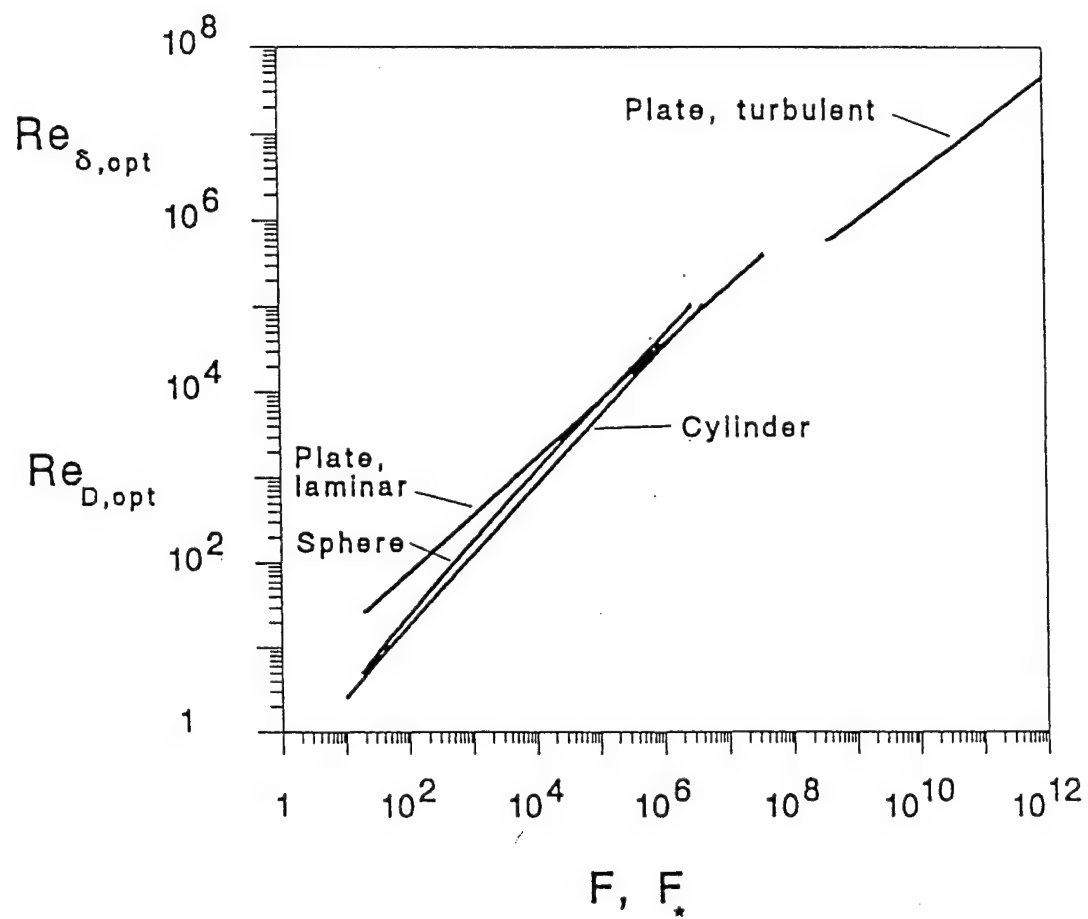
F, F$_*$

Figure 5.4   The optimal sizes of Fig. 5.3 correlated in terms of a universal duty parameter (F, F$_*$) and the Reynolds number based on the transversal length scale of the flow.

analysis was to reveal the most appropriate way to nondimensionalize the heat transfer duty parameter, so that (1) the Prandtl number does not appear as an additional parameter in the final charts (Figs. 5.1 and 5.3), and (2) all the curves show the same trend. This common trend is an indication that a body with a more complicated shape (for example, a short cylinder, or a spheroid) can be optimized numerically based on a procedure that will have the same steps as that presented in section 5.2 or section 5.3.

Progress in the direction of applying the present results directly to the optimal sizing of other shapes was made in the correlations presented in Figs. 5.2 and 5.4. A universal relation between optimal size and heat transfer duty emerges when (1) the size parameter is nondimensionalized as a Reynolds number based on the transversal length scale of the flow (Re_δ, Re_D), and (2) the duty parameter is nondimensionlized as the total heat transfer rate of an equivalent body in two-dimensional flow. This unique, universal trend is reported in Figs. 5.2 and 5.4.

5.5   Notation

B	duty parameter, equation (5.3)
B_s	sphere duty parameter, equation (5.5)
B_*	sphere duty parameter, equation (5.8)
c_e	unit cost of electric energy, \$/J
c_m	unit cost of material, \$/m3
C	total cost, \$
C_D	drag coefficient
D	diameter
F	duty parameter, equations (5.11) and (5.15)
F_D	drag force
F_s	sphere duty parameter, equation (5.13)
F_*	sphere duty parameter, equation (5.18)
h	average heat transfer coefficient
k	fluid thermal conductivity
L	swept length of plate
Nu	overall Nusselt number
Pr	Prandtl number
q	total heat transfer rate
q"	heat flux
$Re_{D,L,\delta}$	Reynolds number, $(D, L, \delta)\, U_\infty/\nu$)
$\dot{S}_{gen}$	entropy generation rate

t	plate thickness
t_0	time of operation
$\overline{T}_w$	average surface temperature
T_∞	free stream temperature
U_∞	free stream velocity
W	plate width, cylinder length
δ	boundary layer thickness, flat plate
μ	viscosity
ν	kinematic viscosity
ρ	density
τ	average wall shear stress

6.   REFERENCES

Beavers, G. S. and Joseph, D. D., 1967, Boundary conditions at a naturally permeable wall, *J. Fluid Mech.*, **30**, 197-207.

Bejan, A., 1982, *Entropy Generation through Heat and Fluid Flow*, Wiley, New York.

Bejan, A., 1988, *Advanced Engineering Thermodynamics*, Wiley, New York, 606.

Bejan, A., 1993, *Heat Transfer*, Wiley, New York.

Bejan, A. and Lage, J. L., 1990, The Prandtl number effect on the transition in natural convection along a vertical surface, *J. Heat Transfer*, **112**, 787-790.

Bejan, A. and Sciubba, E., 1992, The optimal spacing of parallel plates cooled by forced convection, *Int. J. Heat Mass Transfer*, **35**, 3259-3264.

Bergelin, O. P., Brown, G. A., Hull, H. L. and Sullivan, F. W., 1950, Heat transfer and fluid friction during viscous flow across banks of tubes - III, *Trans. ASME.*, **72**, 881-888.

Bergelin, O. P., Davis, E. S. and Hull, H. L., 1949, A study of three tube arrangements in unbaffled tubular heat exchangers, *Trans. ASME*, **71**, 369-374.

Bhattacharjee, S. and Grosshandler, W.L., 1988, The formation of a wall jet near a high temperature wall under microgravity environment, *ASME HTD*, **96**, 711-716.

Carman, P. C., 1937, Fluid flow through granular beds, *Trans. Inst. Chem. Eng.*, **15**, 150-166.

Chang, Y., Beris, A. N. and Michaelides, E. E., 1989, A numerical study of heat and momentum transfer for tube bundles in crossflow, *Int. J. Num. Meth. in Fluids,* **9**, 1381-1394.

Cheng, P., 1978, Heat transfer in geothermal systems, *Adv. Heat Transfer*, **14**, 1-105.

Churchill, S. W. and Bernstein, M., 1977, A correlating equation for forced convection from gases and liquids to a circular cylinder in crossflow, *J. Heat Transfer*, **99**, 300-306.

FIDAP Theoretical Manual, 1991, Fluid Dynamics International, Evanston, IL, V.6.02.

Fletcher, C. A. J., 1991, *Computational Techniques for Fluid Dynamics*, **2**, Springer-Verlag, 360-362.

Groehn, H.G., 1981, Thermal hydraulic investigation of yawed tube bundle heat exchangers, *Heat Exchangers Thermal-Hydraulic Fundamentals and Design*, Kakac, S., Bergles, A.E. and Mayinger, F., eds., Hemisphere, Washington, DC, 97-109.

Guceri, S. and Farouk, B., 1985, Numerical solutions in laminar and turbulent natural convection, *Natural Convection Fundamentals and Applications*, S. Kakac, W. Aung and R. Viskanta, eds., Hemisphere, Washington, DC, 615-654.

Incropera, F. P. and DeWitt, D. P., 1990, *Fundamentals of Heat and Mass Transfer*, Wiley, New York.

Jubran, B.A., Hamdan, M.A. and Abdualh, R. M., 1993, Enhanced heat transfer, missing pin, and optimization of cylindrical pin fin arrays, *J. Heat Transfer*, **115**, 576-583.

Kays, W. M. and London, A. L., 1984, *Compact Heat Exchangers*, 3rd ed., McGraw Hill, New York.

Kline, S. J. and McClintock, F. A., 1953, Describing uncertainties in single-sample experiments, *Mechanical Engineering*, 3, Jan.

Knight, J. D. and Barrett, L. E., 1980, The effect of flexible couplings on the undamped lateral vibrations of rotor-bearing systems, Report No. UVA/464761/MAE30/170, University of Virginia, Charlottesville.

Knight, R. W., Goodling, J. S. and Hall, D. J., 1991, Optimal thermal design of forced convection heat sinks—analytical, *J. Electronic Packaging*, 113, 313-321.

Minakami, K., Mochizuki, S., Murata, A., Yagi, Y. and Iwasaki, H., 1993, Heat transfer characteristics of the pin-fin heat sink (mechanism and effect of turbulence in the pin array), *The 6th International Symposium on Transport Phenomena in Thermal Engineering*, 67-72, Seoul, Korea.

Morega, Al. M., Bejan, A. and Lee, S. W., 1994, Free stream cooling of a stack of parallel plates, *Int. J. Heat Mass Transfer*, 37, to appear.

Moreno, A. A. Y. and Sparrow, E. M., 1987, Heat transfer, pressure drop, and fluid flow patterns in yawed tube banks, *Int. J. Heat Mass Transfer*, 30, 1979-1995.

Morgan, V. T., 1975, The overall convective heat transfer from smooth circular cylinders, *Adv. Heat Transfer*, 11, 199-264.

Nield, D. A. and Bejan, A., 1992, *Convection in Porous Media,* Springer-Verlag, New York.

Omohundro, G. A., Bergelin, O. P. and Colburn, A. P., 1949, Heat transfer and fluid friction during viscous flow across banks of tubes, *Trans. ASME,* 71, 27-34.

Poulikakos, D., 1986, Buoyancy-driven convection in a horizontal fluid layer extending over a porous substrate, *Phys. Fluids*, 29, 3949-3957.

Poulikakos, D. and Johnson, J. M., 1989, Second law analysis of combined heat and mass transfer phenomena in external flow, *Energy*, 14, 67-73.

Poulikakos, D. and Kazmierczak, M., 1987, Forced convection in a duct partially filled with a porous material, *J. Heat Transfer*, 109, 653-662.

Sadeghipour, M. S. and Asheghi, M., 1994, Free convection heat transfer from arrays of vertically separated horizontal cylinders at low Rayleigh numbers, *Int. J. Heat Mass Transfer*, 37, 103-109.

Sathe, S. B., Lin, W. Q. and Tong, T. W., 1988, Natural convection in enclosures containing an insulation with a permeable fluid-porous interface, *Int. J. Heat Fluid Flow*, 9, 389-395.

Sparrow, E. M. and Loeffler, Jr., A. L., 1959, Longitudinal laminar flow between cylinders arranged in a regular array, *AIChE J*, 5, 325-330.

Sparrow, E. M. and Vemuri, S. B., 1985, Natural convection/radiation heat transfer from highly populated pin fin arrays, *J. Heat Transfer*, **107**, 190-197.

Sparrow, E. M., Ramsey, J. W. and Mass, E. A., 1979, Effect of finite width on heat transfer and fluid flow about an inclined rectangular plate, *J. Heat Transfer*, **101**, 199-204.

Tokura, I., Saito, H. Kishinami, K. and Muramoto, K., 1983, An experimental study of free convection heat transfer from a horizontal cylinder in a vertical array set in free space between parallel walls, *J. Heat Transfer*, **105**, 102-107.

Vafai, K. and Thiyagaraja, R., 1987, Analysis of flow and heat transfer at the interface region of a porous medium, *Int. J. Heat Mass Transfer*, **30**, 1391-1405.

Vafai, K. and Tien, C. L., 1981, Boundary and inertia effects on flow and heat transfer in porous media, *Int. J. Heat Mass Transfer*, **24**, 195-202.

Whitaker, S., 1972, Forced convection heat transfer correlations for flow in pipes, past flat plates, single cylinders, single spheres, and flow in packed beds and tube bundles, *AIChE J*, **18**, 361-371.

Willins, R. E. and Griskey, R. G., 1975, Mass transfer from cylinders at various orientations to flowing gas streams, *Canadian J. Chemical Eng.*, **53**, 500-504.

Zukauskas, A., 1972, Heat transfer from tubes in cross flow, *Adv. Heat Transfer*, **8**, 93-160.

Zukauskas, A., 1987a, Heat transfer from tubes in crossflow, *Adv. Heat Transfer*, **18**, 87-159.

Zukauskas, A., 1987b, Convective heat transfer in cross flow, *Handbook of Single-Phase Convective Heat Transfer*, eds. Kakac, S., Shah, R. K. and Aung, W., Wiley, New York, chapter 6.

7. PUBLICATIONS

Fowler, A. J., 1993, Fundamental topics in heat transfer through deformable two-phase media, Ph. D. Thesis, Duke University, Durham, NC, December.

Fowler, A. J. and Bejan, A., 1994, Forced convection in banks of inclined cylinders at low Reynolds numbers, *Int. J. Heat Fluid Flow*, Vol. 15, pp. 90-99.

Fowler, A. J. and Bejan, A., 1995, Forced convection from a surface covered with flexible fibers, *Int. J. Heat Mass Transfer*, Vol. 38, to appear.

Bejan, A., Fowler, A. J. and Stanescu, G., 1995, The optimal spacing between cylinders in a fixed volume cooled by natural convection, *Int. J. Heat Mass Transfer*, Vol. 38, to appear.

Bejan, A., 1993, Optimal density (packing) of fibrous insulation, pp. 574-575 in Bejan, A., *Heat Transfer*, Wiley, New York.

Bejan, A., 1995, *Convection Heat Transfer*, second edition, Wiley, New York, Problems 3.25 and 4.29.

Bejan, A., 1994, Solid-fluid contact, in Humphrey, J. A. C. et al., eds., Unanswered questions in heat transfer research: technological limitations in the characterization of heat transfer at interfaces, ASME Paper No. 94-WA/HT-3.

Bejan, A., 1995, The optimal spacing for cylinders in cross flow forced convection, *J. Heat Transfer*, Vol. 117, to appear.

Stanescu, G., Fowler, A. J. and Bejan, A., 1995, The optimal spacing in free-stream cross-flow forced convection, submitted to *Int. J. Heat Mass Transfer*.